DSPACE

https://dspace.org/

Numerical investigation of selective withdrawal of brine from salt cavern with entrainment of the light phase oil

Moropane, Isaac Sekontshe

2024

https://hdl.handle.net/10539/37368

Downloaded from a DSpace repository. https://dspace.org/

ABSTRACT

This paper presents a numerical simulation of selective withdrawal of brine from salt cavern with entrainment of crude oil. Selective withdrawal is the siphoning of one layer of fluid from two immiscible fluids and avoiding the entrainment of other fluid. A trial of three incline siphons (60^o, 75^o and 90^o) were utilized and each passing through 2.54 cm silicon oil layer and face down below the liquid-liquid interface drawing water upwards. The siphons had a submergence depth of 2.54 cm below the liquid-liquid interface. The simulation was done using the software Ansys Academic, Student 2021 R1. The flow was simulated using two dimensions CFD. The volume of Fluid model and Pressure-based solver were adopted for this simulation. The turbulence model used in the CFD was standard k-epsilon. Semi-Implicit Method for Pressure Linked Equations (SIMPLE) algorithm was adopted for pressure velocity coupling. The results showed that, for avoiding oil entrainment, 90^o siphon is better followed by 60^o inclined, whereas the 75^o inclined was the worse. The results obtained from CFD simulation were validated using experimental data and found to agree. The paper's findings can be useful for Petroleum Engineers to reduce oil entrainment in selective withdrawal from salt caverns in the Strategic Petroleum Reserve (SPR). By predicting the transition from selective withdrawal to oil entrainment, an improved design can optimize the withdrawal process. The design can be enhanced by adjusting the withdrawal rate, pressure, and siphon orientation to minimize the transition from selective withdrawal to oil entrainment. The consequences of oil in the brine system necessitate the separation of oil from the brine, the transfer of oil entrainment back into the salt caverns, and clean-up to avoid environmental contamination. This process of separating and cleaning oil from brine in a brine pond is more time-consuming and expensive.

KEYWORDS

Computational Fluid Dynamics; Volume of Fluid; selective withdrawal; oil entrainment; liquid-liquid interface

DECLARATION

I, Isaac Sekontshe Moropane declares that the content of this research report is my unaided original work. The research report is submitted for the Master of Science in Engineering to the School of Chemical and Metallurgical Engineering, Faculty of Engineering and the Built Engineering, University of Witwatersrand, Johannesburg, South Africa. I declare that I have not previously submitted the work for any other degree or qualification in any university or college.

Signature:  Date: 25/04/2023

Isaac Sekontshe Moropane

1897106

PUBLICATIONS AND PRESENTATIONS EMANATING FROM THIS RESEARCH

Journal Publication – Submitted for publication

- Moropane Isaac Sekontshe, Kitungwa Kabezya, 2022. Numerical investigation of selective withdrawal of brine from salt cavern with entrainment of the light phase oil.
  Upstream Oil and Gas Technology.

ACKNOWLEDGEMENTS

My undoubted note of thanks to my supervisors, Mr Kitungwa Kabezya & Dr Diakanua Nkazi for allowing me to do this project and Mr Kitungwa Kabezya's continuous guidance and knowledge transferred. I would also like to thank the Ansys software company for allowing me to download, install and use the Ansys academic student software.

My humble gratitude goes to the University of Witwatersrand for the great opportunity to study and finance my MSc Chemical Engineering in their institution, this study would have not been possible without the University, my supervisors and Ansys Academic Student.

"I really appreciate people who correct me, because without them, I might have been repeating mistakes for a long time." – Mufti Menk

TABLE OF CONTENTS

ABSTRACT i
KEYWORDS i
DECLARATION ii
PUBLICATIONS AND PRESENTATIONS EMANATING FROM THIS RESEARCH iii
ACKNOWLEDGEMENTS iii
TABLE OF CONTENTS iv
TABLE OF FIGURES vii
LIST OF TABLES x
ABBREVIATIONS xi
RESEARCH REPORT STRUCTURE xii
CHAPTER 1: INTRODUCTION 1
1.1 Research Problem 3
1.2 Main Aim 4
1.3 Research Question 4
CHAPTER 2: LITERATURE REVIEW 5
2.1 Properties of the Crude Oil 5
2.2.1 Density and Specific Gravity 6
2.2.2 API Gravity 7
2.2.3 Viscosity 7
2.2.4 Surface Tension 8
2.2.5 Interfacial Tension 8
2.3 Petroleum Products Storage Methods 9
2.3.1 Floating Roof Tanks 12
2.3.2 Fixed Roof Tanks 14
2.3.3 Abandoned Deep Cast Mines 14
2.3.4 Underground Concrete Storage 14
2.3.5 Unlined Underground Rock Caverns 15
2.3.6 Lined Underground Rock Caverns 16
2.3.7 Depleted oil and gas reservoirs 16
2.3.8 Salt caverns 16
Design or Construct Dome Cavern Shapes 19

Bottom Injection (Direct Leaching Mode) 19
Top Injection (Reverse Leaching Mode) 20
Operation of Salt Cavern 20
2.4 Fluid flow 22
Flow Visualization 25
Particle Image Velocimetry (PIV) 26
Laser Doppler Velocimetry (LDV) 27
Hot Wire Anemometry (HWA) 27
2.5 Selective Withdrawal 28
Previous Studies 28
2.6 Computational Fluid Dynamics (CFD) 32
2.6.1 Governing Equations 33
2.6.2 Models in Multiphase Flow Regime 36
Mixture Model 36
Eulerian Model 37
Volume of Fluid (VOF) Model 37
2.6.3 Solver Settings 39
Pressure-Based Solver 39
Segregated algorithm 39
Coupled algorithm 40
Density-Based Solver 40
Pressure-velocity coupling 41
SIMPLE 41
PISO 41
Coupled Algorithm 41
CHAPTER 3: RESEARCH METHOD **43**
3.1 Experimental Setup 43
3.2 Experimental Procedure 45
3.3 Numerical method 47
3.3.1 Geometry 47
3.3.2 Meshing 51
3.3.3 Setup and Solution 55
CHAPTER 4: RESULTS AND DISCUSSION **61**
4.1 Simulated Water-Silicon Oil Model 61

4.2 Vortex Formation and Velocity Vector in the Simulation 64
4.2.1 Vortex Formation 64
4.2.2 Velocity Vector 65
4.3 The effect of Pressure and Velocity 68
4.4 Calculated Dimensionless Numbers 72
4.4.1 Reynolds Number 74
4.4.2 Froude Number 74
4.4.3 Weber Number 75
CHAPTER 5: CONCLUSION AND RECOMMENDATION **77**
5.1 Conclusion 77
5.2 Recommendation 77
APPENDIX A: SYMMETRICAL LINES ALONG THE SIPHON AND HORIZONTAL LINES BELOW THE SIPHON'S INLET **78**
APPENDIX B: SUMMARY STEPS OF FLOW SOLVER IN FLUENT **81**
APPENDIX B: CALCULATIONS OF THE DIMENSIONLESS NUMBERS **83**
REFERENCES **86**

TABLE OF FIGURES

Figure 1: Salt cavern oil storage (Shi et al., 2017). **2**
Figure 2: Internal floating roof tank (Barker, 2018). **13**
Figure 3: External floating roof tank (Ledzung, 2012). **13**
Figure 4: (a)-Cone and (b)-Dome roof tank (Ledzung, 2012). **14**
Figure 5: (a)-Bedded salt formation and (b)-Dome salt formation respectively (Geocaching, 2008). **17**
Figure 6: Deformation of Thin Bedded formation (Bruno & Dusseault, 2003). **18**
Figure 7: (A)–Bottom injection or Direct leaching mode and (B)–Top injection or Reverse leaching mode (Nanda, Rath & Usmani, 2015). **20**
Figure 8: Salt cavern operation (Lane, 2019). **21**
Figure 9: (a)-Laminar and (b)-Turbulent flow (Shivam, 2020). **24**
Figure 10: (a)-Primary siphon orientation and (b)-Secondary siphon orientation below liquid-liquid interface (Hartenberg & O'Hern, 2011). **29**
Figure 11: Interface withdrawal (Zhou & Feng, 2010b). **30**
Figure 12: Element control volume with inlet and outlet mass flow (Anderson & Wendt 2009). **33**
Figure 13: Mass flow terms with three inlets and three outlets (Anderson & Wendt 2009). **34**
Figure 14: Element control volume with inlet and outlet momentum flux (Anderson & Wendt 2009). **35**
Figure 15: Momentum flux terms with three inlets and three outlets (Anderson & Wendt 2009). **35**
Figure 16: Experimental setup of the hexagonal testing tank (Hartenberg & O'Hern, 2011). **44**
Figure 17: Testing tank as viewed through a windowpane (Hartenberg & O'Hern, 2011). **46**
Figure 18: Successful completion of geometry, Meshing, Setup & Solution and postprocessing which was indicated by the green tick. **48**
Figure 19: Geometry and dimensions of salt cavern with 60^{o} inclined siphon from Design-Modeler of Ansys 2021 R1 ..... **49**
Figure 20: Geometry and dimensions of salt cavern with 75^{o} inclined siphon from DesignModeler of Ansys 2021 R1 ..... **50**

Figure 21: Geometry and dimensions of salt cavern with 90^{o} inclined siphon from DesignModeler of Ansys 2021 R1. **51**
Figure 22: Mashed geometry of salt cavern with 60^{o} inclined siphon from Meshing-Modeler of Ansys 2021 R1. **52**
Figure 23: Mashed geometry of salt cavern with 75^{o} inclined siphon from Meshing-Modeler of Ansys 2021 R1. **53**
Figure 24: Mashed geometry of salt cavern with 90^{o} inclined siphon from Meshing-Modeler of Ansys 2021 R1. **54**
Figure 25: ANSYS Launcher. **55**
Figure 26: General Settings on ANSYS FLUENT. **56**
Figure 27: Setting of Multiphase Model in ANSYS FLUENT. **57**
Figure 28: Input Coordinates on ANSYS FLUENT. **58**
Figure 29: Simulated steps of the occurrence of oil entrainment at the 60^{o} inclined siphon obtained from Ansys. **61**
Figure 30: Simulated steps of the occurrence of oil entrainment at the 75^{o} inclined siphon obtained from Ansys. **63**
Figure 31: Simulated steps of the occurrence of oil entrainment at the 90^{o} siphon obtained from Ansys **63**
Figure 32: Stages of vortex formation at 60^{o} siphon obtained from Ansys. **64**
Figure 33: Velocity vector on primary orientation siphon obtained from experimental data (Hartenberg & O'Hern, 2011). **65**
Figure 34: Velocity vector at the 60^{o} inclined siphon obtained from the simulation. **66**
Figure 35: Velocity vector at the 75^{o} inclined siphon obtained from the simulation. **67**
Figure 36: Velocity vector at the 90^{o} siphon obtained from the simulation. **68**
Figure 37: Variation of pressure along a horizontal line below the inlet. **69**
Figure 38: Variation of pressure along the symmetrical line to the siphon. **70**
Figure 39: Variation of velocity along a horizontal line below the inlet. **71**
Figure 40: Variation of velocity along the symmetrical line to the siphon. **72**
Figure 41: Dimensionless Numbers on the siphon angle **73**
Figure 42: Froude & Weber number as a function of normalised submergence. **76**

Figure 43: At a 60^{o} inclined siphon, Symmetrical line along the siphon and horizontal line below the inlet..... **78**
Figure 44: At a 75^{o} inclined siphon, Symmetrical line along the siphon and horizontal line below the inlet..... **79**
Figure 45: At a 90^{o} inclined siphon, Symmetrical line along the siphon and horizontal line below the inlet..... **80**
Figure 46: Summary steps of Pressure-Based Solution Methods (Ansys Inc, 2009). **81**
Figure 47: Summary steps of Density-Based Solution Method (Ansys Inc, 2009). **82**

LIST OF TABLES

Table 1: General physical-chemical characteristics of crude oil in the South region of Pakistan (Yasin et al., 2013). **6**

Table 2: Dimensionless Numbers **73**

Table 3: Flow velocity at the siphon's inlet of the simulations **83**

Table 4: Properties of fluids used in the simulation..... **83**

Table 5: Testing tank geometry values. **83**

ABBREVIATIONS

API	American Petroleum Institute
ASTM	American Society for Testing and Materials
CAD	Computer-Aided Design
CFD	Computational Fluid Dynamics
FLT	Fuel-Oil Leak Test
FSM	Fractional Step Method
HWA	Hot Wire Anemometry
LDV	Laser Doppler Velocimetry
LPM	Litres per minute
LVDT	Linear Variable Displacement Transducer
MALR	Maximum Admissible Leak Rate
MDLR	Minimum Detectable Leak Rate
MIT	Mechanical Integrity Test
NLT	Nitrogen Leak Test
PDMS	Polydimethyl siloxane
PISO	Pressure-Implicit with Splitting of Operators
PIV	Particle Image Velocimetry
RANS	Reynolds-Average Navier-Stokes
SG	Specific gravity
SIMPLE	Semi-Implicit Method for Pressure Linked Equations
SIMPLEC	SIMPLE-Consistent
SPR	Strategic Petroleum Reserve
VOF	Volume of Fluid

RESEARCH REPORT STRUCTURE

This research report is divided into five chapters as described below and some other relevant information is provided in appendices.

Chapter 1: *Introduction.* The current chapter provides background and motivation information on the problem. A comprehensive purpose of the study is presented, in which the research problem, main objectives or aim of the current investigation are given.

Chapter 2: Literature Review. This chapter aims at highlighting the most relevant aspects related to entrainment of crude oil during the selective withdrawal of brine. The detailed background of crude oil storage methods and operations is provided in this chapter. Computational Fluid Dynamics methods and the properties of crude oil is also provided in this chapter.

Chapter 3: Research Method. This chapter highlights specific methods used in the research project. The chapter answers two main questions: How was the data generated? How was generated data analysed? The numerical investigation was carried out using CFD. The simulation was done using Ansys Academic Student R2021 and workbench-fluent was used as an analysis system. The numerical method is divided into: 1-Geometry, 2-Meshing, 3-Boundary conditions, 4-Solver and 5-Result analysis.

Chapter 4: Results and Discussion. The simulation data generated is presented and thoroughly discussed in this chapter. The simulation data is compared with the experimental data to validate the Hartenberg and O'Hern (2011) investigation.

Chapter 5: Conclusion and recommendation. This final chapter summarizes the findings of the simulation and compared the findings with the experimental investigation. The chapter also includes the recommendations for future study.

CHAPTER 1: INTRODUCTION

Strategic petroleum reserve (SPR) is a stockpile of crude oil, managed by governments and the private sector, that is specifically designed to ensure emergency fuel supplies and strengthen national security during an energy crisis (Naithani, 2012). The stockpile can only sustain countries for a limited period during oil and gas supply disruptions. This depends solely on the capacity of the reserves and the consumption per country (Lane, 2019). Crude oil interruption supply does not only soar the price of crude oil but threatens the food security, transportation system and energy supply. Remedies for crude oil interruption supply among other things are: diversify energy sources and supply, domestic oil and gas production, crude oil stockpiling or oil and gas strategic reserves. Diversify energy sources and supply, crude oil importers should diversify their supply, not rely only on a specific region or country due to the political and economic risks associated with crude oil. Domestic oil and gas production, oil and gas production for domestic consumption and export is seen as a way to attract international investment, enhance economic growth and create an income stream to assist other sectors of the economy to thrive.

Oil and gas storage facilities or Strategic petroleum reserves are categorised in underground and above ground storage (Ledzung, 2012). The underground storage facilities are bigger in size and large in storage capacity. The storage capacity of oil and gas strategic reserves is crucial. These types of oil and gas storage facilities include salt caverns, depleted wells, abandoned deep mines, unlined rock caverns, lined rock caverns, barge storage, and in-ground concrete tanks (Guo et al., 2020; Han et al., 2007; Naithani, 2012; Nanda *et al*., 2015). Stockpiling of oil and gas in caverns is a well-recognised technique around the globe, mainly for security supply (Lane, 2019). These methods are essential for ensuring that the reserves are available when needed. The development and operation of salt caverns in the strategic reserve for oil and gas are pertinent to the current investigation.

Salt cavern facilities are developed by drilling into rich salt formations and adding fresh water to dissolve the salt, and then removing the dissolved salt or saturated solution (brine) and then send to ponds and tanks for storage purposes for later operation. This process is called solution mining (Hartenberg & O'Hern, 2011). Salt caverns are used to store the crude oil above the brine. Salt caverns are the cheapest for crude oil storage facilities and are followed by unlined rock caverns (Han et al., 2007; Naithani, 2012). When the crude oil is transferred into the salt caverns, a certain

amount of brine is pumped out through a suspended siphon passing in the crude oil layer into the brine layer using selective withdrawal method (Park & Chung, 2014; Rath et al., 2008). A typical example of a salt cavern is shown in **Figure 1**.

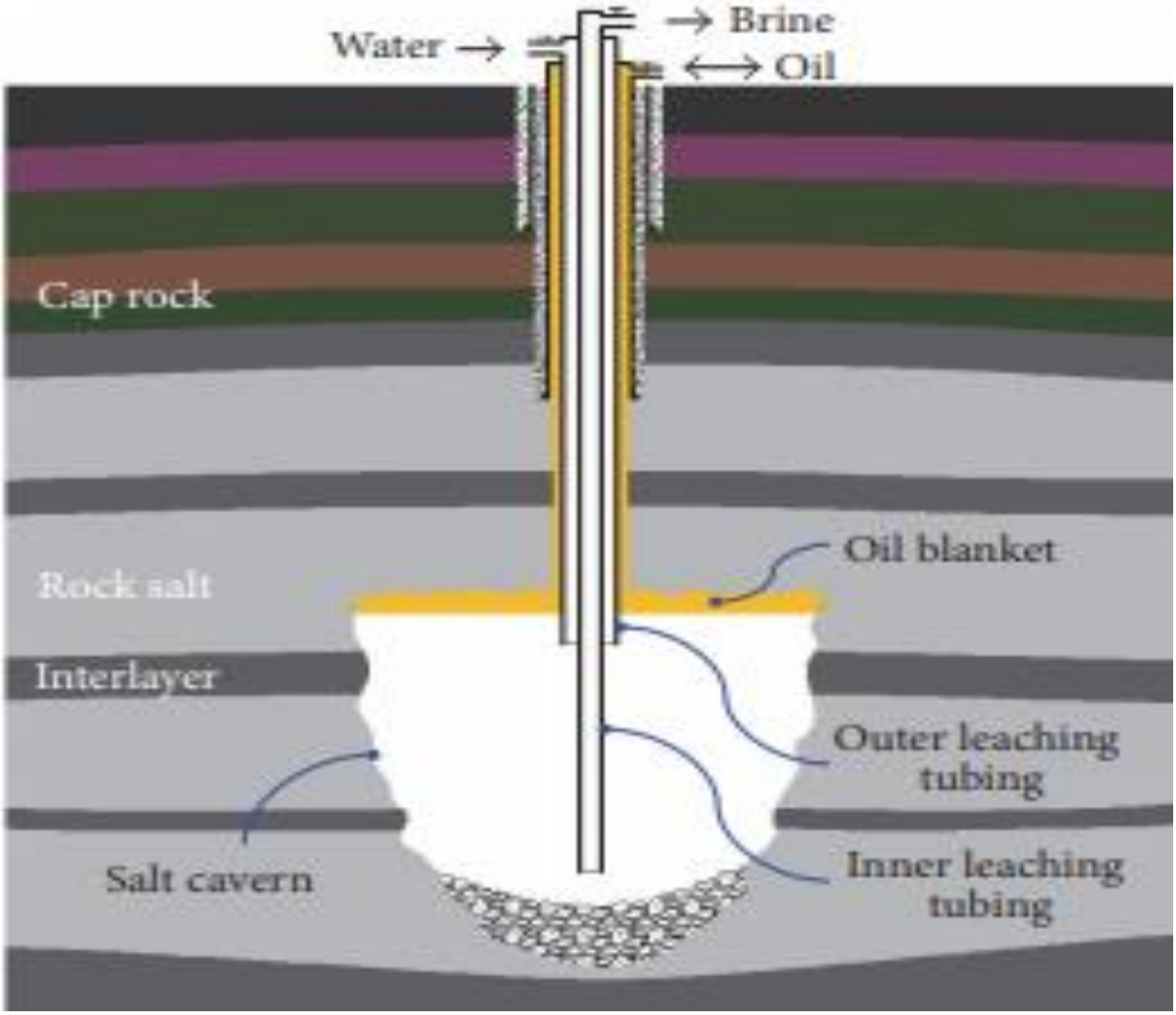


Figure 1: Salt cavern oil storage (Shi *et al.*, 2017).

This process is called selective withdrawal. During the selective withdrawal process, the entrainment of petroleum products needs to be avoided to ensure high productivity (Kabezya *et al.*, 2019). Selective withdrawal is the withdrawal of one layer of fluid from the immiscible fluid system at a given flow rate, siphon orientation, depth of suspended withdrawal siphon and siphon inside diameter (Hartenberg & O'Hern, 2011; Lu *et al*., 2018). In a daily operation of salt caverns, the withdrawal of brine at the maximum flow rate is critical and desirable. The challenge during brine withdrawal among other things is the entrainment of crude oil. The unintended withdrawal

of crude oil entrainment from the salt caverns and transfer it back into the caverns consume more time and is expensive. Numerous studies in selective withdrawal method have been reviewed (Berkenbusch *et al.*, 2008; Blanchette & Zhang, 2009; Cohen, 2004; Cohen & Nagel, 2002; Farrow & Hocking, 2006; Hartenberg & O'Hern, 2011; Kabezya *et al.*, 2019; Zhou and Feng ,2010a; Zhou & Feng, 2010b), however, the majority of these studies focused on the selective withdrawal of two miscible liquids and studies about the selective withdrawal of two immiscible liquids are limited (Blanchette and Zhang, 2009; Kabezya *et al.*, 2019; Hartenberg & O'Hern, 2011; Zhou & Feng, 2010b).

Deep knowledge of the two immiscible fluids behaviour, interface tension deformation and any challenges associated with the selective withdrawal of brine in salt caverns is crucial for effective operations of the salt caverns and reduction of operational costs (Li & Renardy, 2000). Crude oil storage methods, Computational Fluid Dynamics (CFD) and physical-chemical properties of crude oil play important role in the investigation of the current study. Previous work by Blanchette & Zhang (2009), Hartenberg & O'Hern (2011) and Zhou & Feng (2010b) provided some direction for further research into the challenge of selective withdrawal and transition to entrainment of the undesired fluid. This study will focus only on the numerical simulation of selective withdrawal of two immiscible fluids to understand the behaviour of crude oil and brine in salt cavern conditions. Simulation fluids in the current investigation are silicone oil and water to represent crude oil and brine respectively. The simulated outcomes will be compared to the physical observations and measurements of the previous laboratory investigation by Hartenberg and O'Hern (2011).

1.1 Research Problem

The physical problem under investigation is the interface tension deformation or to put it more clearly, the challenge is to explain the interface deformation of two immiscible liquids. Narrowing it down, even more, the actual issue is the withdrawal of the undesired fluid or entrainment of crude oil during selective withdrawal of brine in the salt caverns.

In our model problem, an axisymmetric withdrawal flow driven by a point of sink 2.54 cm below the interface in the water layer deforms an interface between two immiscible liquids (oil and water) of different viscosity and density or other properties. When pumping begins in the selective withdrawal in the Strategic Petroleum Reserve, the interface between oil and brine is drawn down, allowing undesirable liquid (oil) to enter the siphon's inlet. The potential consequences of oil in the brine system necessitate the separation of oil from the brine, the transfer of oil entrainment

back into the salt caverns, and cleanup to avoid environmental contamination. This process of cleaning and separating oil from brine in a brine pond takes longer and is more expensive.

1.2 Main Aim

The main objective of this research project is to investigate numerically the entrainment of crude oil during the selective withdrawal of brine. Silicone oil and water will be used as simulated fluids to represent crude oil and brine respectively.

1.3 Research Question

- What encourages the unintended withdrawal of crude oil during selective withdrawal of brine in the salt cavern?
- What is the effect of siphon leaning angle on the liquid-liquid interface deformation?
- How does the flow rate of brine influence the deformation of the liquid-liquid interface?

CHAPTER 2: LITERATURE REVIEW

This chapter offers a review of existing literature that provided the foundation for this investigation. This Chapter is made up of five main sections. *Section 2.2: Properties of crude oil*, all physical-chemical properties of crude used in the study are described in this section. *Section 2.3: Petroleum products storage methods*, different types of petroleum storage facilities and operational procedures thereof are described in this section. *Section 2.4: Fluid flow*, the definition of flow, types of flow, geometries of pipe and how the suction is formed are described in this section. *Section 2.5: Selective withdrawal*, challenges and factors influencing selective withdrawal are described in this section. Previous investigations relating to selective withdrawal are also outlined in this section. Lastly, *Section 2.6: Computational Fluid Dynamics (CFD)*, principle, different applications and methods in CFD are described in this section. Governing Equations are outlined in this section.

2.1 Properties of the Crude Oil

Crude oil is a complex, naturally occurring liquid mixture primarily composed of hydrocarbons, primarily aliphatic, alicyclic, and aromatic hydrocarbons. Impurities may also be present in trace amounts. Crude oil contains impurities such as sulphur, oxygen, carbon dioxide, nitrogen, traces of metals (Iron, Vanadium, Aluminium, Chromium, Cobalt, Sodium, Potassium, Mercury, Manganese and Nickle), salts and water. Crude oil is frequently referred to as "black gold." Refining crude oil into usable petroleum products necessitates, among other things, characterizing the crude oil's physical and chemical properties. Crude oil has a carbon range of C_1 to C_{120} and is classified on the basis of its physical-chemical characteristics. The characteristics that are referred to commonly as commercial parameters include density, API gravity, sulfur content, acid gases and water content (Abdulsalam, 2019). These common parameters determine the value of the crude oil and also assist with the handling and processing of crude oil. Some typical properties of crude oil are shown in **Table 1** (Yasin *et al*., 2013). Density and Specific gravity, API gravity, Viscosity, Surface and interfacial tension are physical properties applicable to the current investigation and they are discussed in this section. Crude oil is classified based on API gravity (discussed in subsection 2.2.2) and sulfur content. Crude oil with sulfur content less than 0.500 wt% is considered sweet; greater than 0.500 wt% is sour. Crude oil **H**, **I**, **J**, **K** and **M** in **Table 1** are classified as Light sweet crude oil while **L** is classified as Light sour crude oil.

Table 1: General physical-chemical characteristics of crude oil in the South region of Pakistan (Yasin et al., 2013).

Characteristics	Test method (ASTM)	Crude Oil H	I	J	K	L	M
SP. Gravity@60/60°F	D-1298	0.8310	0.8360	0.8350	0.8088	0.8135	0.8130
API Gravity@60/60°F	D-1298	38.77	37.75	37.96	43.45	42.43	42.54
Sulfur (wt %)	D-4294	0.018	0.276	0.2360	0.2793	0.8267	0.2630
Water (Vol %)	D-95	0.05	0.05	0.05	7.0	7.0	6.0
Kin. Viscosity @ 40°C (cSt)	D-445	1.99	2.00	1.95	1.29	1.28	1.27
Kin. Viscosity@ 50°C (cSt)	D-445	1.46	1.47	1.42	1.14	1.15	1.14
Pour Point. (°C)	D-97	+18	+18	+21	+6	+12	+12

2.2.1 Density and Specific Gravity

The density of crude oil is defined as the mass of oil per unit volume (*kg/l or kg/m^3 or g/cm^3*) at a specific temperature as shown in **Equation (1)** and it is usually represented by the Greek letter "ρ". Density is a fundamental physical characteristic that can be used with other properties to characterize both light and heavy fractions of petroleum products. It is also used to convert the measured mass to volume. The density decreases with increasing temperature and increases with increasing pressure. Crude oil will float in water due to its low density (ASTM Standard D4052, 2011). The pressure in the salt cavern must be high enough to keep crude oil in a liquid phase as per the phase diagram principle. The correct temperature is required to prevent crude oil evaporation or crystallization or brine crystallization.

$$\rho_o = \frac{mass}{volume} \quad (1)$$

Specific gravity (SG) is the ratio of the density of the fluid at a stated temperature to the density of water at a stated temperature as shown in **Equation (2)**. Specific gravity is also known as

relative density and it is dimensionless (ASTM Standard D4052, 2011). The specific gravity is used in the calculation of API gravity.

$$SG = \frac{\rho_{crude\ oil}}{\rho_{water}} \quad (2)$$

Crude oil and silicone oil are nonpolar liquids and water and brine are polar liquids. This means that crude oil/silicone oil and water/brine are immiscible and separated by interfacial tension. Silicone oil is a mixture of polydimethylsiloxanes with dimethicone and simethicone and has a specific gravity of less than 0.97, meaning it can float in water (Barca, Caporossi & Rizzo, 2014). Water has a specific gravity of 1.0. Brine has a specific gravity of more than 1.0 (Tatar, Halali & Mohammad, 2016).

2.2.2 API Gravity

API gravity is the measure of how heavy or light a petroleum liquid is compared to water as indicated in **Equation (3).**

$$API = \frac{141.5}{SG} - 131.5 \quad (3)$$

If the API gravity of crude oil is more than 10^o, it is lighter and can float on water. If API gravity is less than 10^o, it is heavier and sinks in water. High API gravity means the crude oil is less dense (low density) and low API gravity means the crude oil is denser (high density). Crude oil is classified as light, medium or heavy, based on its API gravity. Light crude oil – API gravity >35.1^o, medium crude oil – API gravity >22.3^o and <35.1^o, Heavy crude oil – API gravity <22.3^o, Extra heavy crude oil – API gravity <10^o (Abdulsalam, 2019).

2.2.3 Viscosity

In general, a fluid's viscosity is a measurement of its resistance to flow, and there are two forms of viscosity: dynamic and kinematic viscosities. Dynamic viscosity is a measure of fluid resistance to flow or deformation that represents a material's capacity to transmit momentum in response to steady or time-dependent external shear forces, as illustrated in **Equation (4a)**. Sometimes is referred to as absolute viscosity and it is measured in N.s/m^2 or Pa.s or kg/ms.

$$\text{Absolute viscosity } = \frac{Fy}{AV} \quad (4a)$$

F is an applied force in N, y is a separation distance in m, V is a speed in m/s and A is an area in m^2.

Kinematic viscosity is the resistance of the fluid to flow under gravity or it can be defined as the ratio of dynamic viscosity to the density of the fluid at the same temperature and pressure as shown in **Equation (4b)**. It is measured in mm^2/s or m^2/s or cm^2/s. Viscosity measurement helps in the pump design. In addition, it is important for fuel handling, optimum storage and operational condition. Viscosity for gases increases with temperature. The viscosity for liquids (crude oil) decreases as increasing temperature is due to weakening cohesive forces. Some typical viscosities are shown in **Table 1.**

$$\text{Kinematic viscosity} = \frac{\text{absolute viscosity}}{\text{density}} \quad (4b)$$

1 cm^2/s is called a stoke (St). the centistoke (1 cSt = 10^{-2} St) is 1 mm^2/s (ASTM Standard D445, 2017a).

2.2.4 Surface Tension

The interface is the boundary between two phases, so it is with noting the difference between surface and interfacial tension because both exist when two phases are present (Gazem *et al*.,2018). Surface tension is typically known as the air-liquid phase boundary. The force per unit length parallel to the surface is the surface tension to counterbalance the net downward pull. The surface tension results from the greater cohesive force of liquid molecular attraction than the adhesive force of air molecular attraction. The net force on the molecule at the surface is into the bulk of the liquid causing the liquid to behave as if its surface was covered with a stretched elastic membrane (Lautrup, 2011; Sophocleous, 2010).

2.2.5 Interfacial Tension

Interfacial tension is classified as the force per unit length, the one that is more applicable to the current investigation. Interfacial tension is one of the most significant features of the interface between two inhomogeneous or immiscible liquids. Interfacial tension is a boundary between two molecules as a result of attractive forces. The liquid-liquid interface is significantly important for numerous process applications such as industrial separation involving extraction enhanced oil recovery (Wang & Anderkon, 2013; Vanysek & Ramirez, 2008). Hartenberg & O'Hern (2011) stated that the interface distortion is the result of multiple forces, whereas the interface tension restores the interface. Buoyancy is the main contributor of resilience that prevents the transition to light entrainment, whereas the cause of the transition to light entrainment is driven by inertia

forces. Hartenberg & O'Hern (2011) measured interfacial tension of six liquid pairings using a ring tensiometer and obtained results of 0.03 – 0.04 N/m. These results showed that liquid pairing has little effect on the interfacial tension. In this study, only one liquid pairing of polydimethylsiloxane (PDMS) known as silicone oil and water will be investigated. PDMS with density and viscosity of 918 kg/m^3 and 0.005 kg/ms respectively and water with density and viscosity of 998 kg/m^3 and 0.001 kg/ms respectively.

2.3 Petroleum Products Storage Methods

Oil storage facilities are tanks or containers or reservoirs that hold oil during different stages of oil processing before it can be refined into various final products for the consumers. Oil storage facilities can be designed in different sizes, shapes, materials based on their application, legal requirement, environment as well as safety. Either of the following two storage conditions is taken into account, depending on the type of petroleum product: ambient temperature and atmospheric pressure, or ambient temperature and high pressure. Depending on specific physical properties (e.g., density, flash point, viscosity, pour point, Reid vapor pressure) of the crude oil and other petroleum products, the storage temperature will be defined. Crude oil and other petroleum products can be stored under atmospheric pressure at a temperature of approximately 15°C. The temperature of 15°C is used as a standard reference condition to express the volumes of gases and liquids and related quantities such as the rate of volumetric flow. Petroleum products that have a low flash point can pose a high fire risk if they are stored at higher temperatures. When compared to high temperatures, petroleum products at low temperatures move slowly (viscosity) or have difficulties being poured out (pour point) which will affect pumping system. The interfacial tension between crude oil and brine also depends on the temperature, the interfacial tension showed an increase with an increase in temperature under anaerobic conditions, whereas at aerobic conditions, interfacial interface decreased with temperature (Hjelmeland & Larrondo, 1986). The biodegradability of crude oil was found to be highly dependent on its composition and on incubation temperature. Crude oils that are lighter at 20°C tend to experience more evaporation and are more prone to biodegradation compared to heavier crude oils. However, these lighter crude oils contain volatile components that evaporate slowly at 10°C, which can hinder microbial degradation. On the other hand, heavier oils do not have a volatile fraction and have lower rates of oil evaporation at 20°C than lighter crude oils. (Atlas, 1975). The change in vapour pressure

should, however, be controlled in the case of large-scale storage and discharge of crude oil. Park & Chung (2014) suggested that in order to hold the LPG in a liquid form, LPG needs to be kept under high pressure. Due to high operating pressure for LPG storage, the cavern geometry is designed to be less capacious and egg-shaped compared to crude oil, to maintain the high pressure. There are two main types of oil storage facilities, namely: aboveground and underground storage facilities, each has pros and cons (Gsctanks, 2020). This study will focus mainly on the underground storage facilities, particularly the salt caverns for the storage of crude oil.

Aboveground storages are basically constructed above the ground and they are cost-effective to install, easy to maintain or easy to check leaks and access to repair. However, they have low storage capacity. A single tank has nominal volume ranging from 47500 to 190000 cubic meters. Corresponding tank sizes range from 60 to 120 m in diameter and 12 to 19.2 m height (API, 2020), while salt cavern can hold 1.5 million cubic meters oil (Hartenberg & O'Hern,2011). According to joined study conducted by oil and gas companies around the globe, there are 16 ~ 20 large aboveground oil tank fire accidents per year (Li and Dai, 2021). According to Bérest & Brouard (2003) study, fires or explosions are less likely to occur because of impermeability of the salt caverns, however, a small number of accidents have occurred in the past.

Underground storage facilities are built deep beneath the ground in Oil and Gas Industry for storage of oil and gas (Sigl *et al*., 2014). During periods of low demand, underground storage facilities can store surplus products (LPG, natural gas and crude oil) and supply products during a time of high demand (Lane, 2019). Underground storage consists of strategic and commercial volumes, which uses the same principles and technologies in the storage method. The only difference is its aim of long-term storage of crude oil and rotates them a few times a year.

Tightness in underground storage is a fundamental prerequisite and minimum product leakage is required. According to Berest & Brouard (2003), there are three key factors contributing to the problem of leakage in underground storage, namely: pressure distribution of different fluids, geological environment and cementing workmanship, and well architecture. The leakage can be tested by either the liquid leak test or the nitrogen leak test. The salt cavern leakage can be tested using Mechanical Integrity Test (MIT) to prove the integrity of the tubing, formation, and casing on the new designs and repairs. A typical working injection pressure must be used for MIT. There are two different types of MIT: the Fuel-Oil Leak Test (FLT) and the Nitrogen Leak Test (NLT).

The NLT is utilized for full-size cavern tests, while the FLT is typically utilized prior to the cavern being leached out (Bérest *et al*., 2001).

During FLT, a fuel-oil column is lowered into the annular gap to conduct the test, and the evolution of the brine and fuel-oil pressures as determined by the well head is monitored. A leak is evidently indicated by a significant pressure-drop rate. Additionally, the fuel oil is removed after the test and weighed in order to compare it to the weight of the volume of fuel oil that was injected. During NLT, the location of the brine/nitrogen interface is tracked using a central string filled with brine and a logging instrument. The interface will shift upward whenever there is a nitrogen leak. The measurements to track the location of the interface are performed every 24 hours for two or three days (Bérest *et al*., 2001; Crotogino, 1995) The most widely used MIT is the Nitrogen Leak Test (NLT). Since nitrogen has a significantly lower viscosity than liquid, it is possible to detect very minor leaks.

The quantity of leaking that a cavern should be permitted is a significant concern. Crotogino (1995) distinguishes between the Minimum Detectable Leak Rate and the Maximum Admissible Leak Rate. The MDLR is a term used in leak testing to identify the smallest detectable leak rate while the maximum admissible leak rate is the highest rate of leakage that is considered acceptable. Crotogino (1995) advises that the MDLR be set at one-third of the MALR in the test's design and the maximum Admissible Leak Rate to be 150 kg/day at the temperature and pressure of 27oC and 17MPa respectively. It is necessary to divide the mass flow rate by 2 (for LPG), 3 (for gas oil), or 10 (for crude oil) when comparing the flow rates of viscous fluids to nitrogen under equivalent temperature and pressure (Bérest *et al*., 2001; Crotogino, 1995).

Underground storage facilities enjoy more advantages over aboveground storage in terms of safety, security, low operational costs and land space. However, underground storage is very expensive to install, not easy to inspect which increase the chances of leaks and pollution (Gsctanks, 2020). underground storages include salt caverns, underground concrete tanks, unlined underground rock caverns, lined underground rock caverns and depleted oil and gas reservoirs (Naithani, 2012; Park & Chung, 2014; Shi *et al*., 2017). According to Berest & Brouard (2003); Mohanty *et al*. (2013); Naithani (2012); Park & Chung (2014); Sigl *et al*. (2014) & Shi *et al*. (2017) studies, advantages of underground storage facilities are as follows;

- ❖ Hazards are very low due to sabotage by terrorist activity, war, bombing, storms, earthquakes, floods, typhoons, tsunamis, external fires, explosions, plane crushes.
- ❖ Surface land requirement is low and the land aboveground can be used for other things.
- ❖ Hydrocarbons are isolated from oxygen (which is necessary for combustion) in the air by several hundred meters of rock.
- ❖ The lifetime of the underground storage is longer than aboveground storage. Lifetime of underground caverns or storages depend on several factors; such as rock or salt formation, product and quantity, temperature and pressure. Salt cavern can last for decades or even centuries. Estimated lifespan for rock cavern is 30 to 100 years, for underground tank is 30 to 40 years while aboveground tank is 10 to 15 years.
- ❖ The control and firefighting systems are much easier and cheaper to install and run.
- ❖ The huge remnants of the rock formation that are excavated can be used as a building material or in an infrastructure development.
- ❖ Underground storage generates fewer losses from evaporation.
- ❖ The operation costs of the underground are less due to the large storage capacity and become lesser in the long term.

2.3.1 Floating Roof Tanks

Floating roof storage tanks consist of a cylindrical steel shell, pipes, dispensing system, spill containment devices, overfill protection devices and secondary containment systems (Wami *et al*., 2017). The floating roof tank is when the roof of the tank floats on the liquid surface due to filling, emptying, contraction and expansion as the liquid level changes. The roof is designed to move around in the storage tank with the liquid. In crude oil storage, floating roof tanks can have external and internal floating roofs.

Internal Floating Roof Tank

As shown in **Figure 2**, the internal floating roof tank has both a permanently fixed roof (Dome/cone/flat) and a floating roof inside. In reducing the free space above the stored liquid, the floating roof system is very important to minimize the loss of the stored liquid product due to evaporation. Minimizing the fire risk by reducing the volatile gases inside the storage tank is another important factor in using the floating roof (API, 2020; EL-Samanody, Ghorab & Noaman, 2017).

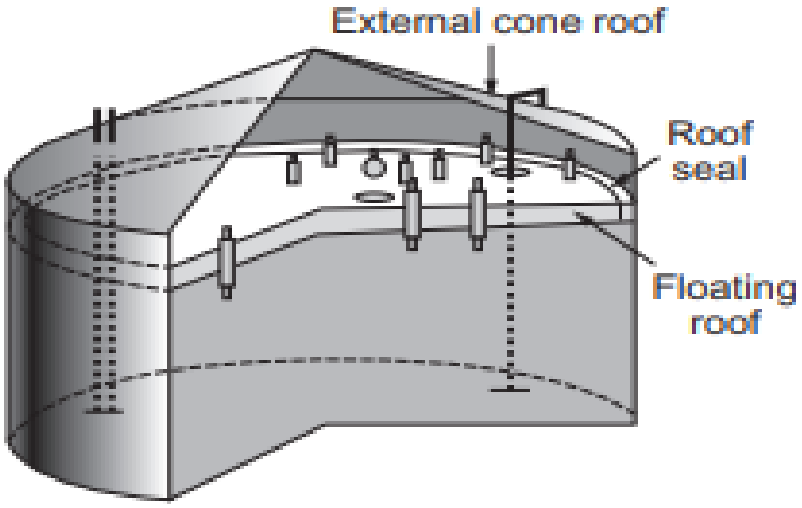


Figure 2: Internal floating roof tank (Barker, 2018).

External Floating Roof Tank

The external floating roof tank does not have a permanently fixed roof, only a floating roof is installed, as shown in **Figure 3** (Gsctanks, 2020). In reducing the free space above the stored liquid, the floating roof system is very important to minimize the loss of the stored liquid product due to evaporation. Minimizing the fire risk by reducing the volatile gases inside the storage tank is another important factor in using the floating roof (API, 2020; EL-Samanody, Ghorab & Noaman, 2017).

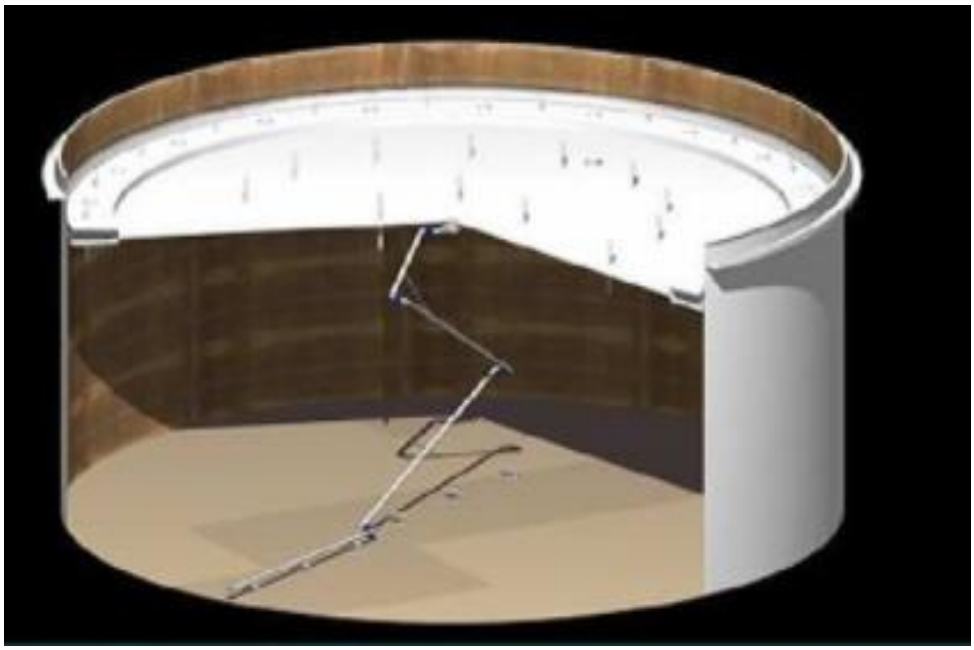


Figure 3: External floating roof tank (Ledzung, 2012).

2.3.2 Fixed Roof Tanks

Usually, fixed roof storage tanks are cylindrical in shape and can be oriented either horizontally or vertically. Fixed roof tanks consist of pipes, dispensing systems, spill containment devices, overfill protection devices and secondary containment systems (Wami *et al*., 2017). As shown in **Figure 4**, fixed roof tanks have a steel shell with a permanently affixed roof that can be flat or cone/dome-shaped. Fixed roof tanks are either freely ventilated or have a pressure/vacuum vent fitted. Fixed roof tanks are the least expensive to construct.

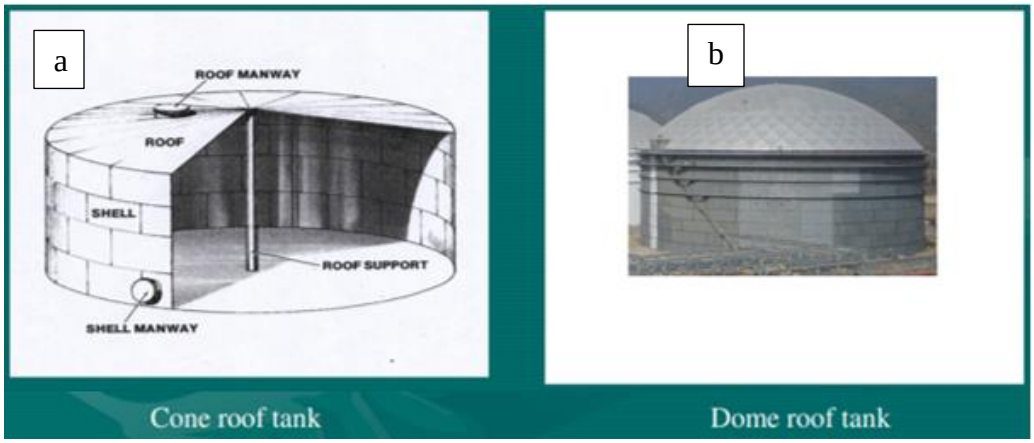


Figure 4: (a)-Cone and (b)-Dome roof tank (Ledzung, 2012).

2.3.3 Abandoned Deep Cast Mines

Abandoned mines that were previously used to extract mineral resources such as gold, ore, coal and salt can be used as a hydrocarbon storage facility, depending on the rock formation. Abandoned mines are available in abundance across the globe with a great capacity and sufficient depths. They have, however, been used very infrequently for gas storage. Just one abandoned salt mine in Europe is currently used as a storage facility for natural gas. The storage facility converted from abandoned mines depends largely on the impermeability of the surrounding rock mass and the cost of seal manufacturing. Sweden was the first country to convert abandoned mines into liquid hydrocarbon storage (Schneider & Donadei, 2016).

2.3.4 Underground Concrete Storage

According to Nanda, Rath & Usmani (2015), the Republic of South Africa was the only country with underground concrete tanks. The building of underground concrete the tank depends upon the geological settings, pipeline network, seaports and location of existing refineries. The tank

mainly consists of a floor, roof slab and sidewalls. The roof slab is directly resting on the column heads inside the tank. The tank is built with strong reinforced concrete and internally coated with acrylonitrile to ensure tank is impermeable. The secondary containment by external high-density polyethylene membrane is used to collect leaked crude oil without polluting the environment. The leaked crude oil into secondary containment is pumped back into the tank. The borehole is used to monitor the possible contamination of groundwater or the environment.

2.3.5 Unlined Underground Rock Caverns

An unlined underground rock cavern is created by excavating through the rock formation and groundwater which are suitable for the creation of rock caverns and storage of hydrocarbons. Storage of fuels in unlined rock caverns is a mature and well-proven technique that was originally developed in Sweden. In an unlined rock cavern, there is no concrete lining to create a barrier between the stored petroleum product and the rock formation. The lining of the caverns with concrete would be expensive due to the high capacity of the caverns (Naithani, 2012). Shotcrete and rock bolting support systems are widely used to ensure the caverns' stability (Rath *et al*., 2008). Hydraulic confinement is the fundamental concept of storage in an unlined rock cavern. The caverns are sufficiently deep for adequate hydrostatic pressure to counter the vapour pressure or liquid pressure of the substance deposited within the cavern (Naithani, 2012; Rath *et al*., 2008). According to Sigl *et al*. (2014), the principle for storage of crude oil in unlined underground rock caverns are groundwater pressure, the density of water and crude oil and insolubility of crude oil in water. The caverns are excavated where the level of groundwater is high and the rock formation must remain saturated with water even while excavation is being carried out. The natural pores of the rock and water percolate continuously into the cavern, preventing oil from leaking out (Mohanty *et al*., 2013). The water curtain system is installed to further ensure the flow of water from the rock formation to the cavern (Rath *et al*., 2008).

The water curtain system consists of an array of horizontal boreholes evenly spaced across the cavern region and is used to increase the hydrostatic pressure of the rock formation. Once there is a drop of hydrostatic pressure, the water curtains are put into operation to increase formation pressure. To intersect all of the joints of the rock formation, boreholes are drilled from the water curtain tunnel. The proper sealing of the stored product ensures saturated rock formation and groundwater flowing into caverns. The water is regularly pumped out of the caverns for treatment

and disposal to create sufficient storage of petroleum products (Park & Chung, 2014). According to Naithani (2012), unlined underground rock caverns, after salt caverns, are the second cheapest caverns used to store hydrocarbons.

2.3.6 Lined Underground Rock Caverns

A lined underground rock cavern is created by excavating through the rock formation which is suitable for the creation of rock caverns and storage of hydrocarbons. The steel alloy and reinforced concrete are used for lining the caverns. The lined underground formation is suitable for any hydrocarbons because the hydrocarbons are not in contact with the rock formation and it is safe and environmentally friendly. These caverns are extremely expensive (Guo, Hao & Niu, 2020; Han *et al.,* 2007; Nanda, Rath & Usmani, 2015).

2.3.7 Depleted oil and gas reservoirs

The most widely used underground storage sites for natural gas are the depleted oil and gas fields, especially the gas fields used for natural gas storage. These storage facilities are widely available with no need to excavate or drill through the formation. However, not all depleted oil and gas fields are suitable for conversion into a natural gas storage facility. The suitability requirements include the reservoir rock's depth, sufficient permeability and porosity. Depleted oil and gas fields tend to have low flexibility for injection and withdrawal of gas to be stored (Letcher, 2016; Nanda, Rath & Usmani, 2015). According to Azin, Nasiri & Entezari (2008), abandonment pressure is one of the significant factors for natural gas storage in depleted reservoirs. If the gas reservoir is depleted down to its ultimate recovery, the pressure might not be enough storage operations which will affect the withdrawal rate.

2.3.8 Salt caverns

Canada was reportedly the first country to utilise salt caverns in the 1940s. in the 1950s Europeans, countries started to utilise salt caverns as hydrocarbon's storage. Rock salt is formed under dry and arid climatic conditions in an oceanic basin (Lane, 2019). Salt caverns are constructed by drilling on the salt formations to create a well and pumping fresh water to dissolve the rock salt. The dissolved salt or saturated solution or brine is pumped out leaving a cavity or void in the rock salt. This process is called solution mining. The salt caverns do not have internal lining however hydrostatic pressure and rock salt formation make it impossible to lose hydrocarbons into the

formation. It's cheaper to store crude oil in salt caverns for longer periods: 10 times less than aboveground tanks and 20 times less than hard rock mines. Salt caverns are environmentally friendly because the salt is insoluble in hydrocarbons or cannot react with the hydrocarbons. The availability of adequate freshwater supply is a prime requirement (Naithani, 2012; Nanda, Rath & Usmani, 2015; Strauch, Zimmer & Tjallingii, 2019).

According to Lane (2019) and Shi *et al*. (2017), the permeability of the rock salt is very low because of the extremely small hydraulic conductivity of its matrix. The rock salt is stronger than concrete material and it is called 'self-healing' material because any fracture occurred when maximum pressure is exceeded, the rock salt will heal or seal itself when the pressure returns to normal. The salt can withstand large deformation by creeping without failing. Bérest & Brouard (2003) reported permeability of salt rock as low as $K = 10^{-22} – 10^{-20}$ m^2. Construction cost is very low. According to Shi *et al*. (2017), the cost to build aboveground storage was $15 – 18 per barrel, while digging underground rock storage was more than $30 per barrel. However, the construction cost of salt caverns in the Gulf of Mexico was low as $1.5. salt rocks are highly abundant.

Types of Salt Formation

There are two different types of salt formation namely: salt domes formation and bedded salt formation as shown in **Figure 5**.

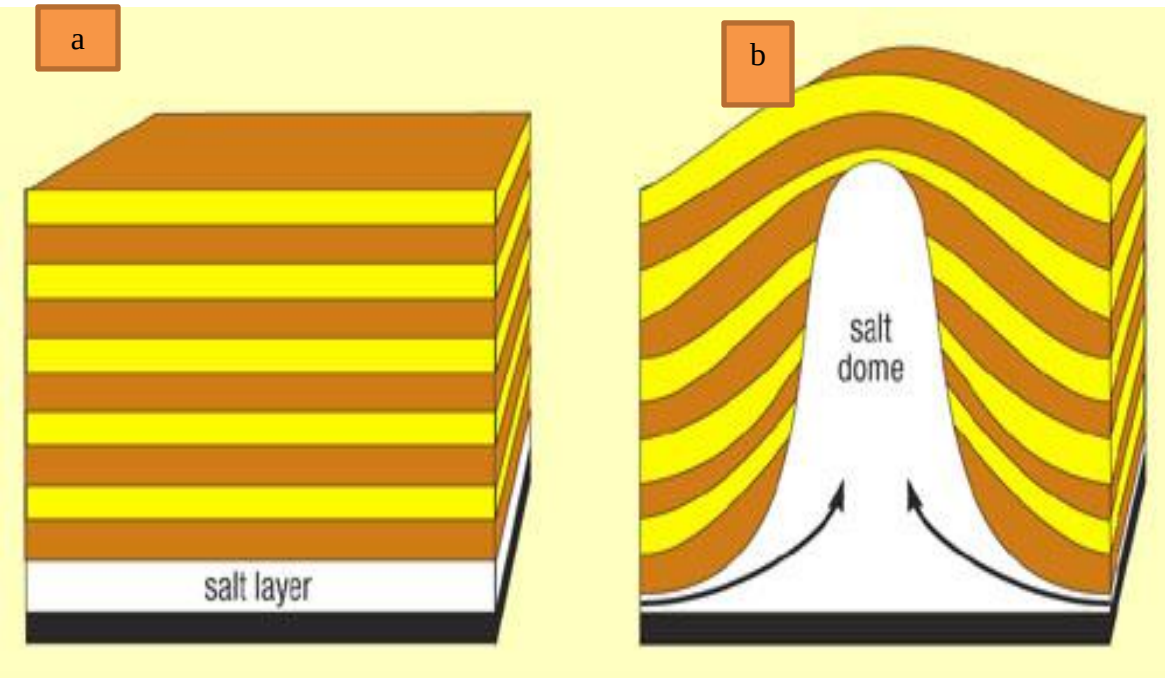


Figure 5: (a)-Bedded salt formation and (b)-Dome salt formation respectively (Geocaching, 2008).

Salt Domes Formation

Salt domes formations are thick, deep-rooted, peak/umbrella-shaped structures that have pierced overburden sequences to ascend to a relatively shallow depth and it is shown in **Figure 5(b)** (Bruno *et al*., 2005; Lane, 2019; Nanda, Rath & Usmani, 2015).

Bedded Salt Formations

Bedded salt formations are thin, horizontal and parallel salt layers with a large surface area and interspersed with interbedded non-salt material such as anhydrite, shale, dolomite, and limestone **Figure 5(a)** (Bruno *et al*., 2005; Lane, 2019; Nanda, Rath & Usmani, 2015).

According to Bruno & Dusseault (2003), the development and operations of the thin-bedded salt cavern have additional engineering challenges related to:

- ❖ The layered, heterogeneous lithology,
- ❖ Differential deformation, creep and bedding plane slip between individual layers and larger lateral to vertical cavern dimensions.

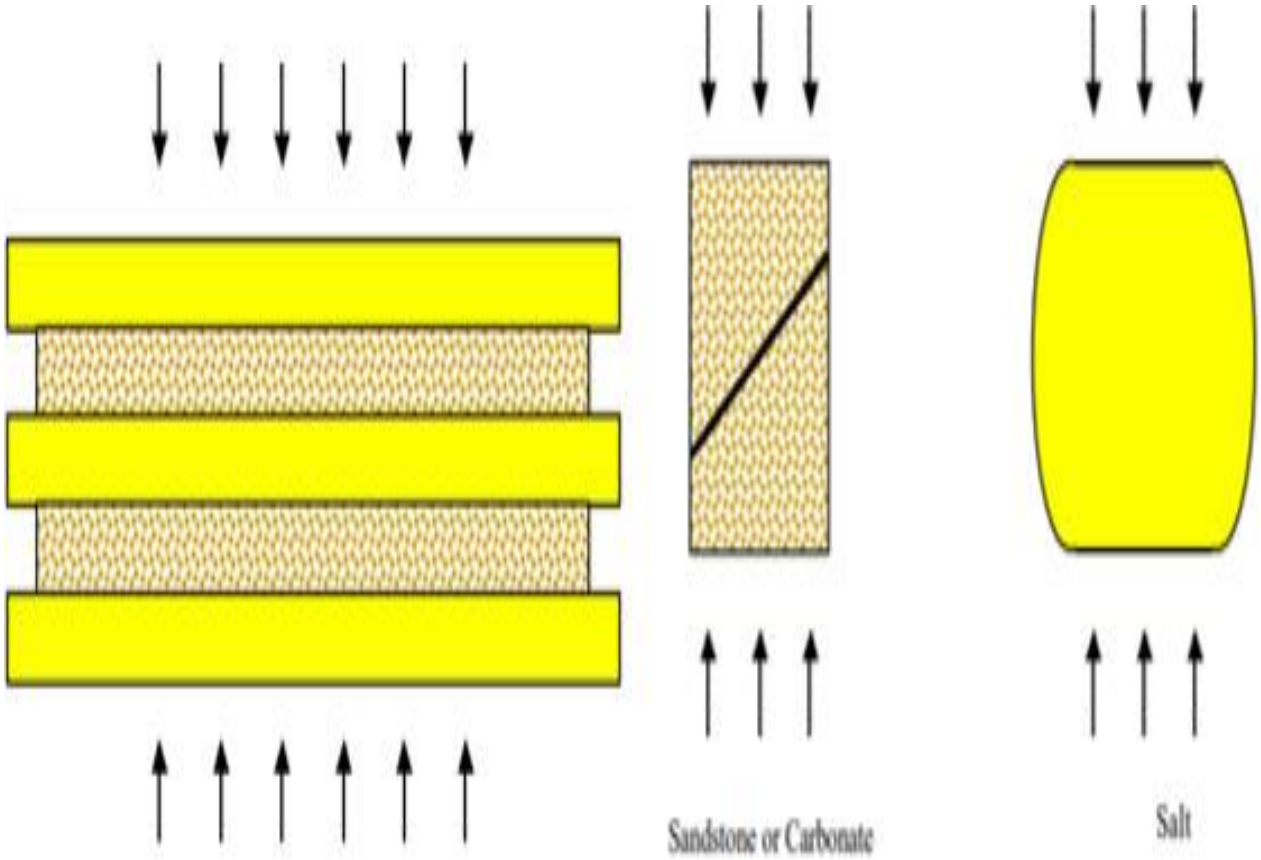


Figure 6: Deformation of Thin Bedded formation (Bruno & Dusseault, 2003).

According to Bruno & Dusseault (2003), there are three basic geomechanical processes that limit maximum and minimum pressures in a bedded salt cavern as shown in **Figure 6**.

- ❖ The tensile fracturing pressure for the salt material and interbedded non-salt material,
- ❖ The minimum and maximum pressure that might induce roof stability or excessive closure and
- ❖ The formation stresses induced by cavern pressure decrease or increase at which bedding plane slip might be induced between heterogeneous material layers.

The typical construction of salt caverns is shown in **Figure 1**. The borehole is drilled through the aquifer (fresh and unstable water zone) which is a few hundred feet, then cemented and cased. The first casing is called surface casing. The borehole is then drilled through interbedded layers of shore and sand into a salt formation. The second casing is installed at least a few hundred feet below the top o of the salt formation. The last casing is installed a few feet below the second casing. The borehole is drilled through the salt formation until the desired length and this borehole is not cased. A suspended pipe is run into the borehole from the surface wellhead, like a straw in a bottle. This pipe is called tubing string or washing string or brine string. Freshwater is injected through the tubing string to dissolve salt formation to create a cavern. The brine is withdrawn to the surface through the annular space between the tubing string and cemented casing. The cavern development is monitored by the amount of brine produced and sonar survey which provide 3-D images periodically during solution mining. Inert gas or diesel fuel is injected at the roof of the caverns to prevent the roof from dissolving during the introduction of freshwater (Bérest & Brouard, 2003; Lane, 2019; Nanda, Rath & Usmani, 2015; Strauch, Zimmer & Tjallingii, 2019). Injection of freshwater and brine withdrawal depends on the required caverns design.

Design or Construct Dome Cavern Shapes

There are two different ways to design or construct dome cavern shapes namely: Bottom injection (direct leaching mode) and Top injection (reverse leaching mode) as shown in **Figure 7** (Strauch, Zimmer & Tjallingii, 2019; Zhang *et al.*, 2018).

Bottom Injection (Direct Leaching Mode)

In bottom injection (Direct leaching mode), water is injected from the bottom through a leaching tube installed into one another with different path independent path flows for water and brine and more salt is dissolved on the lower region. A typical bottom injection is shown in **Figure 7(A)** (Strauch, Zimmer & Tjallingii, 2019; Zhang *et al.*, 2018).

Top Injection (Reverse Leaching Mode)

In top injection (Reverse leaching mode), water is injected from the top through a leaching tube installed into one another with different path independent path flows for water and brine and more salt is dissolved on the upper region. A typical bottom injection is shown in **Figure 7(B).** The saturated brine produced during solution mining can be evaporated in the evaporation ponds or disposed into the ocean or disposal well (Strauch, Zimmer & Tjallingii, 2019; Zhang *et al.,* 2018).

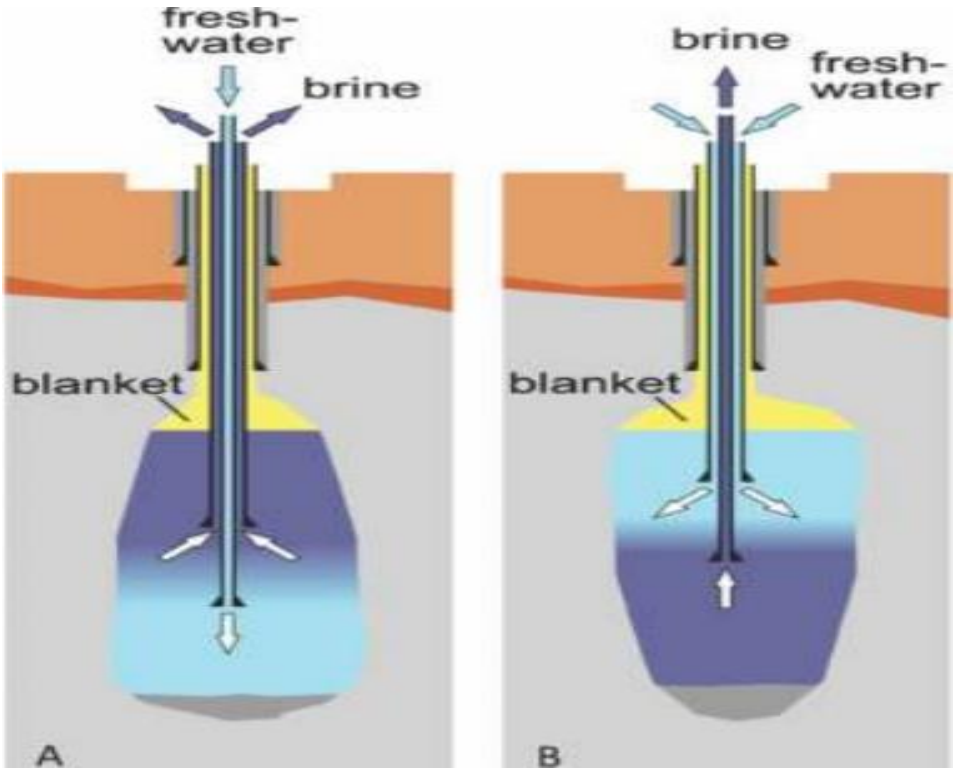


Figure 7: (A)–Bottom injection or Direct leaching mode and (B)–Top injection or Reverse leaching mode (Nanda, Rath & Usmani, 2015).

Operation of Salt Cavern

A salt cavern must always be full of either saturated brine or crude oil or both crude oil/brines. The empty salt cavern is at high risk of collapse if it is exposed to atmospheric pressure (Lane, 2019). When the salt cavern is full of brine only, the cavern must be at atmospheric pressure (Bérest & Brouard, 2003). The correct temperature is required to prevent crude oil evaporation or crystallization and brine crystallization. However maximum operating pressure should be restricted because excess pressure may fracture the rock salt which can increase permeability subsequent to the risk of leakage or results in huge crude oil loss (Zhang *et al.,* 2018).

Salt caverns for liquids (Oil, Naphtha, Kerosene, Gasoline) and liquified hydrocarbons (LPG, ethylene, propylene) are operated by the "brine compensation" method. The brine compensation method is when brine is injected into the caverns and the equivalent volume of product is pumped out (Bérest & Brouard, 2003; Lane, 2019). In the operation of salt caverns, as the crude oil is transferred into the salt cavern by pumping it through the annular space, equivalent saturated brine is withdrawn through the brine string into the separator. The separator removes or separates any crude oil entrainment from the saturated brine before entering the brine bonds to prevent any volatile entrainment in the brine bonds because volatile entrainment in the brine bonds will evaporate into the atmosphere and pollute the air. The brine at the bottom of the separator is then transferred into brine bonds. The crude oil from the separator is transferred back into the salt cavern and gas from the separator if any, is sent to flare to burn it. The brine bonds are constructed and lined in a way that brine cannot leak and contaminate the environment. Any excess brine from the bonds will be transferred into storage tanks or disposed of (ocean or disposal well or evaporation ponds) as shown in **Figure 8** (Lane, 2019).

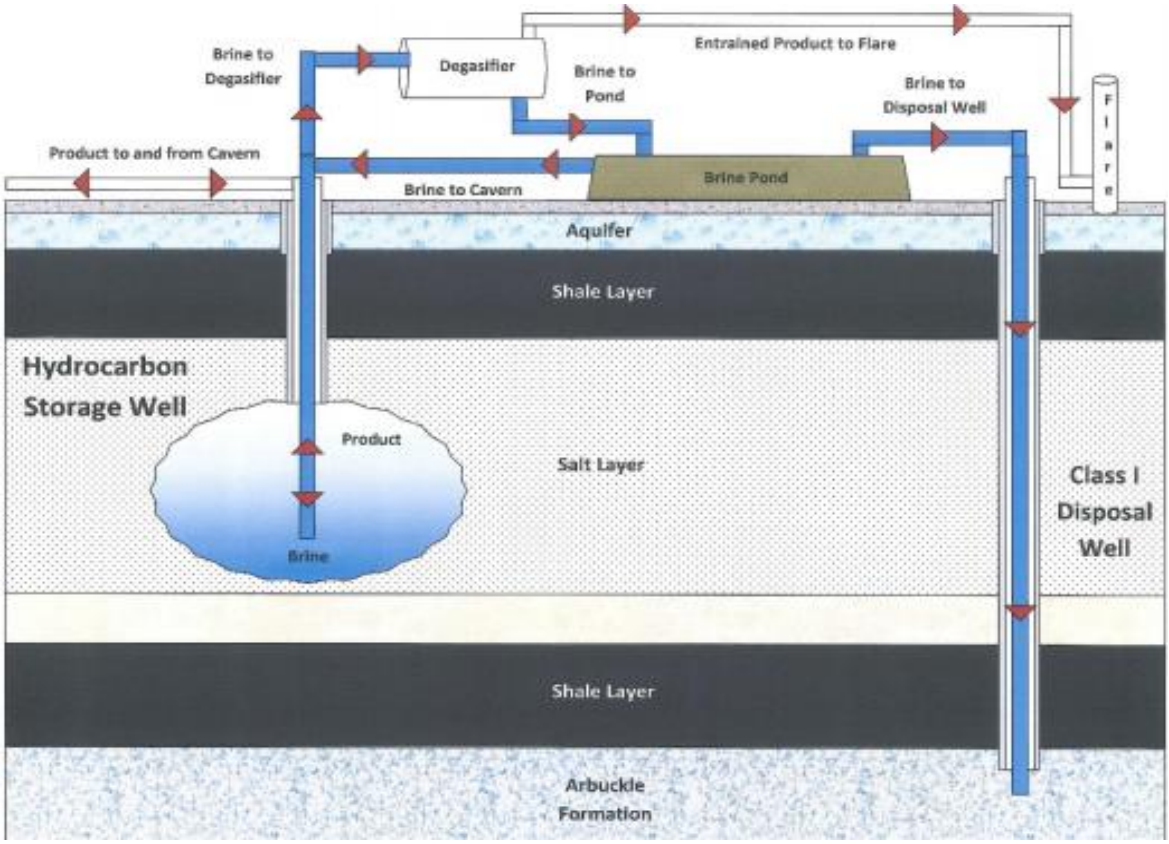


Figure 8: Salt cavern operation (Lane, 2019).

2.4 Fluid flow

A pipe can be in a circular or noncircular geometry. Noncircular geometry is divided into rectangular, ellipse and isosceles triangle shapes. In the current study, the focus was on the pipe with circular geometry. In a circular pipe, most of the fluids, particularly liquids, are transported. Without undergoing major distortion, the circular pipe can withstand great pressure differences. In buildings where the pressure difference is relatively small, non-circular pipes are typically used in heating and cooling systems. (Çengel & Cimbala, 2014; Darby & Chhabra, 2001; Munson *et al*., 2013).

The suction of a fluid is defined as the flow rate at which a fluid is removed through the system, and the flow rate depends on three factors: the fluid viscosity, withdrawal pipe diameter and the amount of negative pressure created by the pump (Darby & Chhabra, 2001). The theory of Bernoulli helps one to evaluate the relationship at any point in the fluid between pressure, density and velocity or flow rate. Flow rate (Q) is the volume (V) of fluid that, passes through an area (A) at a specific time (t) as shown in **Equation (5)**.

$$Q = \frac{V}{t} = \frac{Ad}{t} = A\bar{\upsilon} \quad (5)$$

$$\bar{\upsilon} = \frac{d}{t} \quad (6)$$

where d is a distance or height or length. The flow rate (Q) is directly proportional to both average velocity ($\bar{\upsilon}$) and cross-sectional area (A). If the pipe radius is reduced for an incompressible fluid, the same volume of fluid must flow past each point in the pipe within a given time to ensure continuity of flow as shown in **Equation 7** (Munson *et al*., 2013).

$$Q_1 = Q_2 \text{ or } (A_1\bar{\upsilon}_1 = A_2\bar{\upsilon}_2) \quad (7)$$

When a fluid enters a narrower channel, its velocity increases, which leads to an increase in its kinetic energy. This increase in kinetic energy is due to the net work done on the fluid to push it into the channel and the work done on the fluid by gravity if the fluid changes its vertical position. The narrowing of the channel creates a pressure difference, which results in a net force on the fluid. The net work done on the fluid increases its kinetic energy, causing a drop in pressure in a rapidly-moving fluid, regardless of whether it is confined to a tube or not. This relationship between pressure and velocity in incompressible, frictionless fluid was described by Bernoulli's equation as shown in **Equation (7a).**

$P + 1/2\rho v^2 + \rho gh = \text{constant}$ (7a)

where P is the absolute pressure, ρ is the fluid density, v is the velocity of the fluid, h is the height above some reference point, and g is the acceleration due to gravity. **Equation (7b)** applied to any two points that lie along the path of the fluid.

$P_1 + 1/2\rho v_1^2 + \rho g h_1 = P_2 + 1/2\rho v_2^2 + \rho g h_2$ (7b)

When a fluid moves but its depth remains constant, which means that $h_1=h_2$ this is another important situation. In this case, Bernoulli's equation takes the form as shown in **Equation (7c)**.

$P_1 + 1/2\rho v_1^2 = P_2 + 1/2\rho v_2^2$ (7c)

Here, P_1 and P_2 are the pressures at two different points along the fluid's path, v_1 and v_2 are the velocities at those points, and ρ is the density of the fluid. This equation is important because it shows that when the velocity of a fluid increases, the pressure decreases, and vice versa. This is known as Bernoulli's principle, which is a consequence of Bernoulli's equation (Çengel & Cimbala, 2014; Darby & Chhabra, 2001; Munson *et al.*, 2013).

There are three classes of flow regimes through a pipe and these regimes can be determined using Reynold number (Re_d). A significant non-dimensional parameter used in fluid mechanics is the Reynolds number. It is defined as the proportion of a fluid's inertial force to the viscous force and is shown in **Equation (8)**. The Reynolds number enables fluid flow simulation such that it is possible to index complex operating characteristics to a common value (Emerson, 2015).

$$Re_D = \frac{\rho D \bar{\upsilon}}{\mu} \quad (8)$$

Where: ρ = Fluid density, D = Pipe diameter, $\bar{\upsilon}$ = Average fluid velocity, μ = Absolute (dynamic) viscosity of the fluid. The description of these regimes is the result of extensive studies by scientists and engineers exploring the hypothesis that a transition between low and high velocities passes through fluids flowing in pipes. This transformation triggers a shift in a pipe's velocity profile, which dramatically affects the fluid's dynamics and the ability to accurately calculate the flow rate (Çengel & Cimbala, 2014; Emerson, 2015).

These three classes of flow regimes through a pipe are Laminar, Transitional and Turbulent flow. Laminar flow has a Reynold number (Red) < 2000 and can be defined as a series of liquid cylinders within a closed pipe where the innermost parts flow very slowly or do not move at all, and the outermost parts that touch the pipe flow faster. This flow is regarded as smooth flow because there

is no vibration as shown in **Figure 9(a)** (Abdulsalam, 2019; Çengel & Cimbala, 2014; Munson *et al*., 2013).

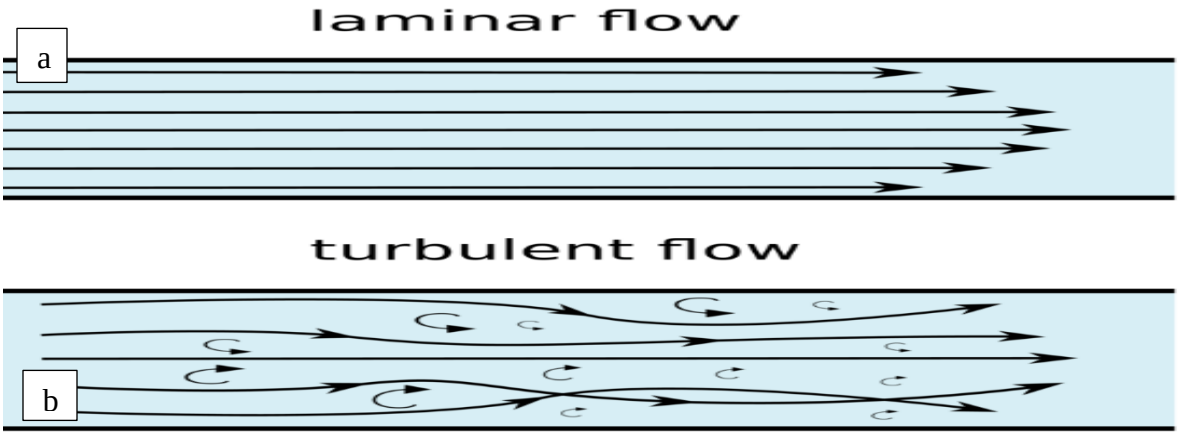


Figure 9: (a)-Laminar and (b)-Turbulent flow (Shivam, 2020).

Turbulent flow has a Reynold number (Red) > 4000 and can be defined as the fluid layers that move very rapidly, mixing the fluid layers, as a result of which intense mixing occurs, the flow pattern changes constantly over time. The velocity of the fluid keeps on changing continuously. The flows are chaotic and cannot be predictable. The fluid flow causes vibration and can cause premature wear in the system and consequently break the pipe as shown in **Figure 9(b)** (Abdulsalam, 2019; Çengel & Cimbala, 2014).

In this study, flows found in crude oil storage are turbulent, so it is important to understand how turbulence affects the stress of wall shear. Turbulent flow is described in flow by chaotic and rapid variations of swirling regions of fluid, called eddies. An additional mechanism for momentum and energy transfer is given by these fluctuations. The swirling eddies transport mass, momentum, and energy to other flow regions much more rapidly than molecular diffusion in turbulent flow, significantly improving mass, momentum, and heat transfer. As a consequence, turbulent flow is related to much higher coefficients of friction, heat transfer, and mass transfer values (Çengel & Cimbala, 2014).

A turbulent fluid flow is when the motion of the fluid is three-dimensional, unpredictable, and random. It is characterized by eddies, or lumps of fluid, which fluctuate both in the direction of the main flow and at right angles to it. These eddies are of different sizes, but typically fluctuate only a few percentages of the mean value. These eddies form and disintegrate in a matter of a few oscillation times, giving turbulent fluid flows a limited time scale (Majumdar, 2011).

The transitional flow has Reynold number (Re_d) >2000 but <4000 and it is the combination of both laminar flow and turbulent flow. It is the transformation of laminar flow to turbulent flow (Abdulsalam, 2019; Çengel & Cimbala, 2014; Li & Renardy, 2000; Moreno, 2014).

The relevant dimensionless parameter used to describe the flow is the Froude number and this number is very important for free surface flows such as in the case of open-channel flow. Froude number is expressed as the ratio of inertia force to force of gravity and is shown in **Equation (9)**. (Hartenberg & O'Hern, 2011; Sequeiros, 2012). Froud number is the flow parameter for flow around a tapping tube and when modelling the flow. Froude number is taken into account due to the aspect of dynamic similarity (Kabezya, Hara & Paton, 2019).

$$Fr_D = \frac{\bar{\upsilon}}{\sqrt{gD}} \quad (9)$$

Where $\bar{\upsilon}$ is the average flow velocity, D is the pipe diameter, and g is the acceleration due to gravity. Abulnaga and Rushdi (2013) mentioned that:

Fr_D < 1 the flow is subcritical; the depth is greater and the velocity is lower.

Fr_D = 1 the flow is critical.

Fr_D > 1 the flow is supercritical; the velocity is higher and the depth is smaller.

Froude number thus provides immediate analysis on the type of flow and how near the flow conditions are to those at critical depth. The closest the Froude number is to 1.0, the more unstable the surface of the fluid becomes, leading to waves or surface disturbances or deformation of the interface (Oetjen, Schüttrumpf & Engel, 2020).

Flow Visualization

In the current investigation, flow visualization was used to analyse the fluid flow. Moving fluids frequently form patterns that are so complex that our intuition fails when we try to imagine them, and the governing equations are incapable of analysing all of their details. Visual images of the actual flow can provide us with information about the true flow pattern (Hagen, Müller & Nielson, 1993). In comparison to the theatrical concept of any object, a human can understand it physically well (Kline, 1969). A famous bon mot asserts that a real picture of the phenomenon is considered to be equivalent to a thousand words.

Measurements are much more difficult in unsteady but not truly periodic flows, such as turbulent shear flows. In such cases, motion pictures of the flow can be extremely helpful in perceiving the overall flow structure, determining instantaneous velocity profiles, and determining the time sequence of events as a step toward establishing causality. It is frequently more convenient to use

flow visualization to determine the actual flow pattern for a given set of conditions. Flow visualization is used to provide important information on a wide range of flow phenomena, including waves in stratified fluids, cells in rotating systems with thermal effects, flow in a tee channel, vortices starting and stopping, supersonic and hypersonic wakes, compressible flow over sharp objects, and flow models in turbulent boundary layers (Hagen, Müller & Nielson, 1993; Kline, 1969). The main aim of flow visualization is to make certain flow structures or floe regions visible (Westerweel, 1997).

There are two types of flow visualization: experimental flow visualization and numerical flow visualization. Experimental flow visualization is critical for gaining insights into flow physics and comprehending practical videos of fluid dynamics. The results of numerical flow visualization are calculated numerically using scalar, vector, and tensor quantities that are difficult to obtain everywhere in the flow domain. By comparing numerical solutions to corresponding experimental results, numerical solutions are validated (Kline, 1969).

Flow visualization techniques utilized in the experimental methodology for turbulent flow analysis include Laser Doppler Velocimetry (LDV), Particle Image Velocimetry (PIV), and Hot Wire Anemometry (HWA). Flow visualisation techniques in the numerical method include; contour, streamlines, velocity vector, vortex structure and particle tracking (Shirayama & Kuwahara, 1990).

Particle Image Velocimetry (PIV)

Particle Image Velocimetry (PIV) is a flow visualization technique that is used to evaluate the instantaneous velocity vector of a flow cross-section. This is a non-intrusive optical flow visualization technique. The PIV is extremely important in the study of high-speed flows and fluid boundary layers. Two or three velocity components are obtained concurrently in PIV however the flow cannot be resolved on both large and small scales at the same time. First, particles that act as fluid tracers must be introduced into the flow facility. These particles are introduced into the flow so that their size, distribution, and concentration can be controlled. A thin sheet illuminates a cross-section of the flow. A camera positioned perpendicular to the light sheet captures sequential photos of the lit flow field. The laser pulsing is generated and synchronized with the camera's frame rate timing sequence using electronics, resulting in single-exposure photos. Finally, a data collection system is employed to record successive pictures from the camera. (Westerweel, 1997). PIV was used in Hartenberg & O'Hern (2011) investigation and it is important to the current study.

Laser Doppler Velocimetry (LDV)

Laser Doppler Velocimetry (LDV) is a non-intrusive technique that is commonly used for reliable measurements of fluid velocity in liquid or gaseous flows. LDV can be used in environments where conventional techniques would be ineffective however collecting data near the walls is difficult. A single high-coherence continuous-wave laser beam is divided in two and then refocused in this approach. The focus zone, also known as the waist, is found within a fluid flow containing naturally or artificially seeded reflecting particles. The inherent coherence of the laser beam produces a sequence of linear interference fringes in the area where it is recombined. Particles traveling through the waist of the beam reflect light, which is refocused and monitored in a photodetector. The intensity of the reflected light fluctuates as a result of the Doppler shift generated by the difference between incident and reflected light, and is consequently proportional to the velocity of the fluid moving through the beam (Eder, Durst & Jordan, 2001; Moghtaderi, 2003).

Hot Wire Anemometry (HWA)

Hot Wire Anemometry (HWA) is a technique for monitoring instantaneous velocities and temperatures at a flow point that is invasive. HWA is a measuring technique that relies on heat transfer from a sensing element and is thus extremely sensitive to temperature variations in the surrounding environment. As a result, using HWA to measure mean flow properties is not usually recommended. Hot wire anemometry is an excellent tool for measuring velocity fluctuations in turbulent flows in the time domain. The primary tool for studying the physics of turbulent flows. To conduct fundamental turbulence studies, realistic turbulence models, HWA, must be developed (Comte-Bellot, 1976).

As previously stated, vortices structures can be examined visually, which is relevant to this study. A vortex is a whirlpool of fluid that revolves around an axis line that might be straight or curved. Typically, vortex formation is induced by a considerable local shift in flow velocity near the siphon entrance. The flow streamlines are extremely near and may interact, causing the flow to become rotational, appear as a swirl, and perhaps evolve into a vortex. Vortices can appear on the free surface or in the subsurface. Light fluid is drawn into the siphon inlet by severe vortices (Hasan & Hayder, 2021).

2.5 Selective Withdrawal

We should start by explaining selective withdrawal, Selective withdrawal is the removal of one layer of fluid from a fluid consisting of multiple layers of varying densities. This withdrawal of fluid can be either above or underneath the interface. The withdrawal all takes place until some critical flow rate is reached from inside the layer adjacent to the withdrawal point, after which fluid is drawn out directly through the sink from both layers. As was originally assumed, the crucial event is not as clear. There is a variety of possibilities for the interface deformation, including flow rate and siphon submergence distance, orientation and diameter (Farrow & Hocking, 2006; Hartenberg & O'Hern, 2011; Shammaa & Zhu, 2010).

Previous Studies

Hartenberg & O'Hern (2011) investigated the effect of two withdrawal siphon opening directions, face-up and face-down opening on the light entrainment transition. Face-down withdrawal siphon passes through the lighter fluid and liquid-liquid interface into the heavy fluid as shown in **Figure 10(a)**, while face-up withdrawal siphon withdrew heavy fluid directly without going through the lighter fluid and liquid-liquid interface **Figure 10(b)**. Due to the relative importance of the impedance to flow induced by the withdrawal siphon walls, the transfer of light entrainment on the face-down withdrawal at a low flow rate occurs at less submergence depth than face-up withdrawal as flow rate increases. The effect of withdrawal siphon opening directions at higher flow rates were not explored in their investigation however, they have suggested that the withdrawal siphon walls at a higher flow rate might not affect the light entrainment transition. They also investigated the relationship between the flow rate and the depth of submergence. An increase in flow rate and withdrawal siphon diameter was found to motivate the transition of light entrainment at deeper submergence depths. Hartenberg & O'Hern (2011) investigation found that a disturbance could be detected as the liquid-liquid interface was approaching the siphon opening. The disruption appeared as a sunken annulus surrounding the withdrawal siphon for the facedown withdrawal siphon orientation that eventually became more peaked before light layer entrainment began. The disruption resembled a conical hump above the withdrawal siphon for the faceup withdrawal siphon orientation before the light entrainment layer began. **Figure 10** displays the withdrawal siphon orientations, including the interface disruption.

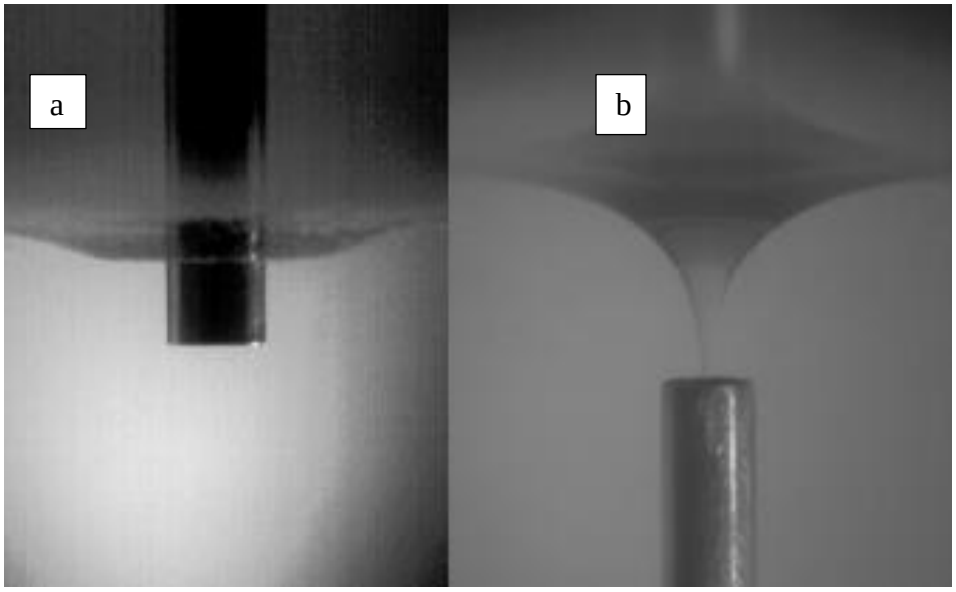


Figure 10: (a)-Primary siphon orientation and (b)-Secondary siphon orientation below liquid-liquid interface (Hartenberg & O'Hern, 2011).

Farrow and Hocking (2006) investigated computer simulations of selective water withdrawal through a slit in the base of a finite rectangular cavity filled with a two-layer fluid with a finite-thickness interface. The involvement of lengthy interfacial waves (basin-scale) in the processes leading to the interface being dragged into the slot received special attention. These waves have been demonstrated to have a key influence in delaying or hastening the drawdown. This means that the drawdown will occur over a wide range of Fr values. The current study will be conducted in such a way that the model takes into consideration the suction tube rather than a drain-hole.

Lubin & Springer (1967) conducted an experimental investigation on selective withdrawal of two-layer stratified liquids. As a function of the sink flow rate, the critical height between the floor of a two-liquid tank and the liquid-liquid interface above was estimated. The Froude number centred on the sink tube diameter was found to be the characteristic non-dimensional parameter describing the flow, assuming surface tension to be negligible and using the Bernoulli theory. The non-dimensional flow rate and the scaled critical depth have been found to have a linear relationship. The flow phenomena reported by Hartenberg & O'Hern (2011), Farrow & Hocking (2006) and Lubin & Springer (1967) are similar. In their investigations, a dip occurs over the point sink on the surface of the lower fluid at a certain entrainment depth and a certain flow rate. Until it reaches a critical entrainment depth and a critical flow rate, the flow is constant, at which point the dip increases rapidly and almost instantaneously extends into the point sink.

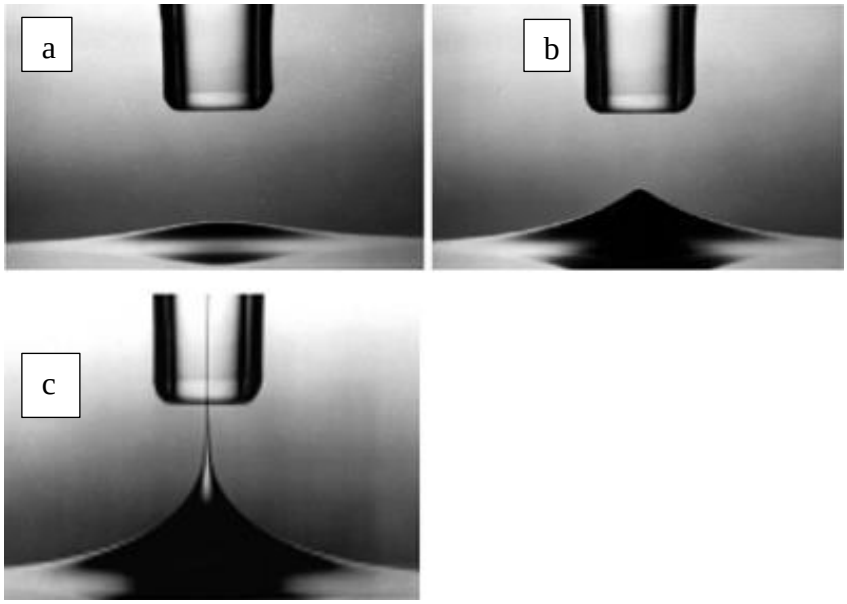


Figure 11: Interface withdrawal (Zhou & Feng, 2010b).

According to Blanchette & Zhang (2009) and Zhou & Feng (2010b) investigation, in the upper layer, a siphon is inserted and suspended above the interface. The liquid was removed at a particular flow rate through the siphon and replenished far from the surface. In the upper layer, this withdrawal produced an axisymmetric flow that radially converges inwards and axially extends. The viscous stress of the withdrawal flow forces the interface upwards and a hump immediately below the siphon is formed by the interface. The hump was replaced with a spout pulled from the bottom layer into the siphon. As seen in **Figure 10**, the selective withdrawal regime, in which only liquid was withdrawn from the top layer, was followed by the viscous entrainment regime, in which liquid was drained from both levels.

Ajoko & Ebughni (2015) used CFX-Pre and ANSYS Fluent to analyse the multiphase flow simulation of oil and gas in a vertical pipe. Solidworks was used to model the pipe. The multiphase equation was used to solve the model with a fluent energy flow equation. A velocity flow for the mixture was the boundary condition at the inlet and the outlet was set to normal atmospheric pressure. The pressure drop through the vertical pipes was verified to be high in their study to test the concepts from the open literature. The pressure drop is a function of the pipe length, and the pressure drop often increases as the length of the pipe increases. The pressure drop can then be regulated by subsequent reductions in the length of the pipe.

Zhou and Feng (2010a) investigated numerical simulations of polymer solution selective withdrawal. They employed finite elements to solve the Navier-Stokes and constitutive equations

in the liquid on an adaptively revised unstructured grid using an arbitrary Lagrangian-Eulerian approach to track its free surface. The rheology of viscoelastic fluids was modelled using the Oldroyd-B and Giesekus equations, and the physical and geometric characteristics were compared to those measured in tests. The estimated interfacial deformation matched the experimental results. Cohen and Nagel (2002) used two fluids of equal viscosities to calculate the hump, and the mean curvature at the hump tip, as a function of the withdrawal flux in their three-dimensional axisymmetric selective withdrawal study. Cohen (2004) studied the transition to other liquid-liquid pairings in the subsequent research. When the transition from selective withdrawal to viscous entrainment was approached from below, the steady-state hump curvature increased considerably. Cohen and Nagel (2002) explained how to apply this rate of increase to a power-law divergence. However, they discovered that the hump never creates a cusp shape. Instead of the transition, the final step of the hump growth gets eliminated. This behavior led to the realization that the almost continuous transformation between the steady-state hump and spout shapes is structured by a single steady-state shape solution. The transition from a hump to a spout was noticed when the radius of curvature at the hump tip was 50 m or larger. Furthermore, the magnitude of the cut-off length implies that the two layers are not dependent on the viscosity contrast.

Berkenbusch, Cohen, and Zhang (2008) performed a computer investigation of the viscous entrainment selective withdrawal transition. In the model problem, an axisymmetric withdrawal flow distorted an interface between two immiscible layers of equal viscosity, which was prompted by a point sink positioned in the upper layer some distance above the interface. It was discovered that steady-state hump solutions cease to exist above the withdrawal flux threshold, resulting in selective liquid withdrawal from the top layer, and that this transition corresponds to a saddle-node bifurcation for hump solutions. Numerical observations on the shape evolution of the steady-state interface were compared to recent experimental data (Berkenbusch, Cohen, & Zhang, 2008). There is a clear awareness of where information overlaps. The considerable rise in curvature at the hump tip reflects a strong tendency in the steady-state interface's development. For high deflections, the hump height is proportional to the logarithm of the curvature at the hump tip; hence, tiny changes in the hump height correspond to significant changes in the hump curvature value. The interface in the current examination dips towards the sink or pipe inlet positioned underneath the interface.

2.6 Computational Fluid Dynamics (CFD)

Computational Fluid Dynamics (CFD) is a computer technique that evaluates or solves fluid flow and heat transfer equations within a well-defined flow geometry (Albaali & Farid, 2006). CFD, or computational fluid dynamics, is the study of processes involving fluid flow, heat transfer, and associated phenomena such as chemical reactions using computer-based simulation. The technique is quite successful, and it may be applied in a wide range of industrial and non-industrial environments. (Versteeg & Malalasekera, 2007). Some examples of this are:

- ❖ Airplane and car aerodynamics: lift and drag.
- ❖ Ship Hydrodynamics.
- ❖ Power plant: combustion of gas turbine and internal combustion engines.
- ❖ Turbomachinery: flows, diffusers, within revolving passages.
- ❖ Electrical and electronic engineering: cooling, including micro-circuit equipment.
- ❖ Chemical process engineering: blending and isolation, moulding of polymers.
- ❖ Buildings' external and internal environment: loading of wind and heating/ventilation.
- ❖ Marine engineering: off-shore structural loads.
- ❖ Ecological engineering: distribution of toxins and waste.
- ❖ Flows in rivers, estuaries, oceans: hydrology and oceanography.
- ❖ Meteorology: the weather forecast.
- ❖ Biomedical engineering: blood flows through veins and arteries.

CFD is a useful and practical analysis tool that can give significant benefits in oil and gas, in areas such as equipment design, petroleum refinery process and optimisation, offshore oil rigs, or platform design, and fire risk and safety cases. For example, the design of efficient drill bits for oil drilling, exploration, petroleum separator design, solid separation design and fire dispersion and mitigation strategy (Hendriana, 2020). CFD is also useful in the enhancement of oil recovery and hydrocarbon storage. Enhanced oil recovery is a method used to extract oil by unconventional methods.

Field and laboratory studies to investigate enhanced oil recovery can be costly, dangerous, slow and difficult to perform. CFD numerical simulation could use results obtained from a laboratory test, whose scales are smaller than field tests to scale up to real conditions and minimize operational risks. Numerical simulations are cheap, faster and safer compared to expensive and dangerous laboratory investigations (Jafar *et al.*, 2019; Lu *et al.*, 2018; Shammaa & Zhu, 2010).

Other advantages of CFD, are its ability to research processes at and above their normal performance limits under hazardous conditions and practically limitless degree of outcome information. All conditions of simulation methods such as temperature, pressure and different forces could be modelled. Complete information and very precise details can be obtained for solving the problem when using CFD. In the experimental investigation, only a few points can be obtained (Versteeg & Malalasekera, 2007).

2.6.1 Governing Equations

The primary governing equations that regulate the physics of fluid mechanics and thermal sciences and are instrumental in the study of computational fluid dynamics (CFD), are conservation of mass (continuity equations), conservation of momentum (Navier-Stokes equations) and energy equations (Wah-Yen *et al.*, 2017). Conservation of energy equation is not considered in this investigation because the current investigation deals with the incompressible fluid flow. General mathematical expression for the conservation of mass is illustrated below;

$$\rho A_1 V_1 = \rho A_2 V_2 \quad (10)$$

Where $\boldsymbol{\rho}$ is the density, $\mathbf{A_1}$ and $\boldsymbol{V_1}$ is the area and volume at the initial state respectively. $\boldsymbol{A_2}$ and $\boldsymbol{V_2}$ is the area and volume at the final state respectively. General mathematical expression for the conservation of momentum is illustrated below;

$$m_1 u_1 + m_2 u_2 = m_1 v_1 + m_2 v_2 \quad (11)$$

Where velocities are $\boldsymbol{u_1}$ and $\boldsymbol{u_2}$ before and $\boldsymbol{v_1}$ and $\boldsymbol{v_2}$ after.

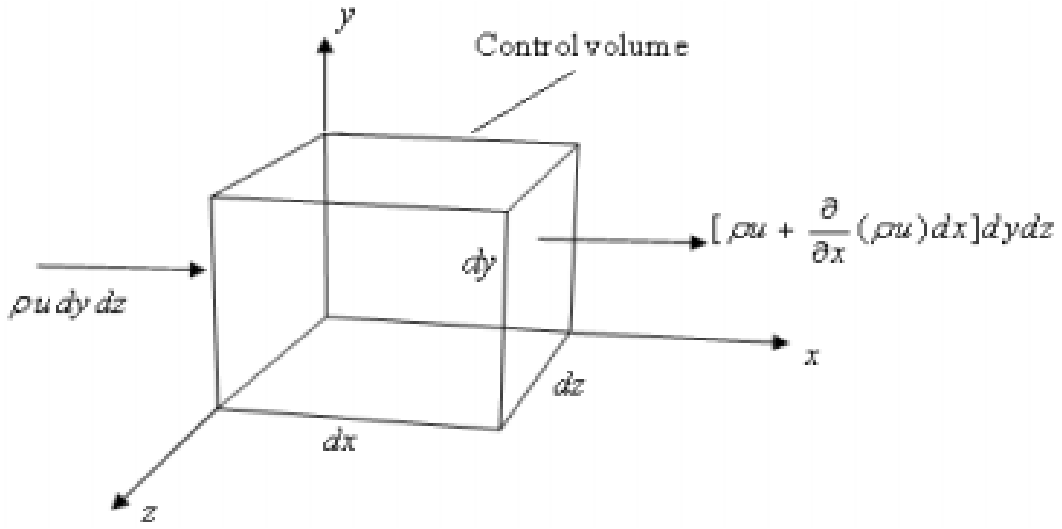


Figure 12: Element control volume with inlet and outlet mass flow (Anderson & Wendt 2009).

Face	Inlet mass flow	Outlet mass flow
x	$\rho u\, dy\, dz$	$\left[\rho u + \frac{\partial}{\partial x}(\rho u)\, dx\right] dy\, dz$
y	$\rho v\, dx\, dz$	$\left[\rho v + \frac{\partial}{\partial y}(\rho v)\, dy\right] dx\, dz$
z	$\rho w\, dx\, dy$	$\left[\rho w + \frac{\partial}{\partial x}(\rho w)\, dz\right] dx\, dy$

Figure 13: Mass flow terms with three inlets and three outlets (Anderson & Wendt 2009).

According to Anderson & Wendt (2009) and Wah-Yen *et al.* (2017), conservation of mass says the net rate of mass (mass outflow – mass inflow) = decrease of mass in fluid element. Inertial mass and gravitational mass are two ways of defining mass. The first one uses the second law of Newton for definition, while the second one uses the gravitation law of Newton. The numerical value for mass is similar in both cases. If this numerical value does not change when there is a change in the method, then it is regarded as mass conservation of mass. Take into account the following fluid element that is fixed in space and from which fluid flows:

- Net rate of mass in x-direction: $[\rho u + \partial(\rho u)/\partial x\, dx]\, dydz - (\rho u)\, dydz = \partial(\rho u)/\partial x\, dxdydz$.
- Net rate of mass in y-direction: $[\rho v + \partial(\rho v)/\partial y\, dy]\, dxdz - (\rho v)\, dxdz = \partial(\rho v)/\partial y\, dxdydz$.
- Net rate of mass in z-direction: $[\rho w + \partial(\rho w)/\partial z\, dz]\, dxdy - (\rho w)\, dxdy = \partial(\rho w)/\partial z\, dxdydz$.

Therefore, the sum of the terms for the 3 directions will be expressed as follows:

- Net mass flow = $[\partial(\rho u)/\partial x + \partial(\rho v)/\partial y + \partial(\rho w)/\partial z]\, dxdydz$

$[\partial(\rho u)/\partial x + \partial(\rho v)/\partial y + \partial(\rho w)/\partial z]\, dxdydz = -\partial\rho/\partial t\, (dxdydz)$

$\partial\rho/\partial t + [\partial(\rho u)/\partial x + \partial(\rho v)/\partial y + \partial(\rho w)/\partial z] = 0$

$\partial\rho/\partial t + \nabla.\, (\rho\bar{v}) = 0$ is the conservation of mass for a stationary fluid element. $(\partial/\partial t)$ and (d/dt) describe partial and total derivatives respectively. $\bar{v}$ **(*u, v, w*)** describes the fluid velocity. In fluid mechanics, the Navier-Stokes equation also referred to as conservation of momentum, is a partial differential equation that describes the flow of incompressible fluids (Anderson & Wendt 2009) and (Wah-Yen *et al.*, 2017).

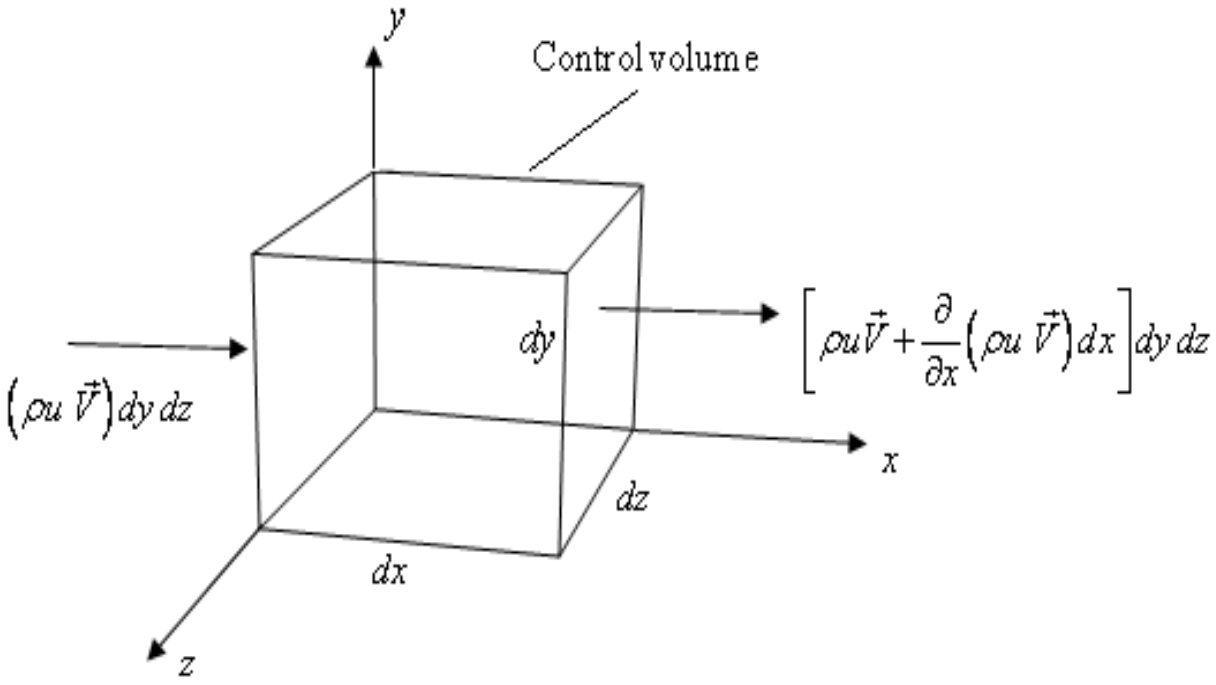


Figure 14: Element control volume with inlet and outlet momentum flux (Anderson & Wendt 2009).

Face	Inlet mass flow	Outlet mass flow
x	$\left(\rho u\ \vec{V}\right)dy\,dz$	$\left[\rho u\vec{V}+\frac{\partial}{\partial x}\left(\rho u\ \vec{V}\right)dx\right]dy\,dz$
y	$\left(\rho v\ \vec{V}\right)dx\,dz$	$\left[\rho v\vec{V}+\frac{\partial}{\partial y}\left(\rho v\ \vec{V}\right)dy\right]dx\,dz$
z	$\left(\rho w\ \vec{V}\right)dx\,dy$	$\left[\rho w\vec{V}+\frac{\partial}{\partial z}\left(\rho w\ \vec{V}\right)dx\right]dx\,dy$

Figure 15: Momentum flux terms with three inlets and three outlets (Anderson & Wendt 2009).

The differential momentum equation for Newtonian fluid if the flow is incompressible with constant density and viscosity are given by, x-momentum: $\rho g_x - \partial p/\partial x + \mu \left[\partial^2 u/\partial x^2 + \partial^2 u/\partial y^2 + \partial^2 u/\partial z^2\right] = \rho\, du/dt$, y-momentum: $\rho g_y - \partial p/\partial y + \mu \left[\partial^2 v/\partial x^2 + \partial^2 v/\partial y^2 + \partial^2 v/\partial z^2\right] = \rho\, dv/dt$ and z-momentum: $\rho g_z - \partial p/\partial z + \mu \left[\partial^2 w/\partial x^2 + \partial^2 w/\partial y^2 + \partial^2 w/\partial z^2\right] = \rho\, dw/dt$. It is a second-order, non-linear partial differential equation and is known as the Navier-Stokes equation. In vector form, it may be represented as, $\rho\bar{g} - \nabla p + \mu\nabla^2 \bar{v} = \rho\, d\bar{v}/dt$. In previous studies, several different realisations of flow-driven topological transitions have been investigated. Here, we analyse those studies that specifically evaluate the ingredients needed for a topological transition to take place and the appropriate ways to describe the interface's evolution near such a transition. In CFD, there are different models to assess the multiphase flow regime.

2.6.2 Models in Multiphase Flow Regime

There are different models to assess the multiphase flow regime namely: mixture, Eulerian and Volume of Fluid (VOF) models (Bonto, Eftekhari & Nick, 2019; Jafar *et al.*, 2019). In this research, VOF model was used to simulate oil and water.

Mixture Model

In the Mixture model, phases are interlocked and can be solved with a single set of momentum equations are solved with a single set of momentum equations. Both control volume and volume fractions can have any value between zero and one depending on the amount filled by primary and secondary phases in the cell. The mixture model can use slip velocities, meaning that fluids can travel at different speeds. On the other hand, the Mixture model can utilise a homogeneous multiphase model, meaning that the phases can travel at the same velocity. The Mixture model can simulate sedimentation, cyclone separators, tiny gas bubbles in a liquid substance and particle-laden flows.

This model answers the secondary phases' continuity, momentum, energy, and volume fraction equations. The mixture model is a good replacement for the complete Eulerian multiphase model in various circumstances. When the particulate phase is widely spread, or when the interphase rules are unknown or their trustworthiness is called into doubt, a comprehensive multiphase model may not be possible. A simpler model, such as the mixture model, can outperform a complete multiphase model while dealing with fewer variables. The mixture model lets you select granular stages and determines their attributes. This is true for liquid-solid fluxes.

$$\frac{\partial}{\partial t}(\rho_m) + \nabla.(\rho_m \bar{\upsilon}_m) = m \quad (12)$$

ρ_m is a mixture density, $\bar{\upsilon}_m$ is a mass average velocity and m is a mass transfer.

Eulerian Model

The Eulerian model allows for phase separation and mixing. It may be used to imitate droplets or bubbles of secondary phases, as well as to determine the diameter of granular particles. For each phase, this model solves the continuity, momentum, enthalpy, and turbulence equations.

Volume of Fluid (VOF) Model

In the VOF model, two or more immiscible (not interlocked) fluids are solved with a single set of momentum equations. The model can track every liquid in the domain during the simulation. The VOF model can simulate water released from the dam, jet breakup, large moving bubbles in a liquid substance and tracking of liquid-liquid or liquid-gas interface for steady or transient flow. In the current study, we investigate oil entrainment into water siphon or deformation of the oil-water interface by tracking both phases in the domain. For this reason, the VOF model is more suitable to solve the problem of the current investigation than its counterpart (Mixture Model).

The VOF approach offers a convenient way to deal with topological changes to the interface, such as merging and folding, which can be difficult to manage by other methods correctly and explicitly (Muzaferija & Peric, 2017). It is robust, minimum storage requirements because interface positions are not stored for each time-step. However, it is restricted to standardized meshes and for practical applications in engineering, its precision is still not adequate. Lastly, it is resolution-dependent (Tang & Wrobel, 2005).

Requirements required for the multi-phase flow prediction of interfaces include (Tang & Wrobel, 2005):

- ❖ the movement of the interface with time,
- ❖ the treatment of partially filled cells,
- ❖ the representation of the interface on a discrete grid,
- ❖ the coupling of the interface conditions with the equations of motion.

The phases share all variables and attributes and reflect volume-averaged values as long as the volume fraction of each phase is known at each location. One of the most difficult aspects of analysing flow consisting of two immiscible liquids of various densities and viscosities is that the region of interest has an unclear free border. To correctly model-free surfaces, three crucial traits are required (Tang & Wrobel, 2005):

❖ To describe the shape and place of a surface, a scheme is necessary,

❖ To develop the shape and location with time, an algorithm is required,

❖ Free–surface boundary conditions must be applied at the surface.

VOF model analyses all phases using a mathematical equation for each transportation phenomenon. Mathematical **Equations (13a)** and **(13b)** show the conservation of mass and momentum respectively. If the flow is incompressible. $\nabla . \bar{\upsilon} = 0$, the flow is governed by the Navier-Stokes equations:

$$\frac{\partial \rho}{\partial t} + \nabla . (\rho \bar{\upsilon}) = 0 \quad (13a)$$

$$\rho \frac{D\bar{\upsilon}}{Dt} = \rho \left(\frac{\partial u}{\partial t} + \bar{\upsilon} . \nabla \bar{\upsilon} \right) = -\nabla p + \nabla \cdot (\mu \nabla \bar{\upsilon}) + \rho \boldsymbol{g} + F \quad (13b)$$

Where $\boldsymbol{p}$ is the pressure, $\boldsymbol{g}$ is the gravitational force, $\boldsymbol{t}$ is the time, $\boldsymbol{\rho}$ is the density and F is the body force (Hirt & Nichols, 1979; Guerrero *et al*., 2017; Lu *et al.*, 2018).

Variables and properties in any given cell are either purely representative of the phases or representatives of a mixture of the phases depending upon the volume fraction values. If α is fluid volume fraction and track the interface, then when α_o=0: the cell is only filled with oil, α_w=1: the cell is only filled with water and 0<α<1: the cell contains interface between the fluids. The VOF model provides a simple and economical way of tracking the interface between the phases using a continuity equation as a function of the volume fraction in two- or three-dimensional meshes (Guerrero, Munoz & Ratkovich, 2017). The two immiscible fluids, the density ρ and the viscosity μ are constant in each fluid.

Average density and viscosity are calculated as a function of the volume fraction are shown in **Equations (14)** and **(15)** respectively (Abdulkadir *et al.*, 2013; Jafari *et al*., 2019; Li & Renardy, 2000; Muzaferija & Peric, 2017).

$$\rho = \rho_w \alpha_w + (1 - \alpha_o) \rho_o \quad (14)$$

$$\mu = \mu_w \alpha_w + (1 - \alpha_o) \mu_o \quad (15)$$

Where density, viscosity and volume fraction, respectively, are expressed by ρ, μ and α. The w and o subscriptions also refer to water and oil respectively. The flow at the inlet must be known and constant at all times. If the density of the fluid is constant, the volume of a fluid particle cannot change as it moves and this means the fluid flow is incompressible.

2.6.3 Solver Settings

A pressure-based or density-based solution can be used to examine the flow numerically. Historically, the pressure-based methodology was intended for low-speed incompressible fluids, whereas the density-based method was created for high-speed compressible fluids. Both systems, however, have recently been expanded and reformed to handle and work in a broader range of flow situations than their primary or traditional objective. Both strategies used momentum equations to calculate the velocity field. In both procedures, the velocity field gets calculated using momentum equations. The density field gets calculated using the continuity equation, while the pressure field is calculated using the equation of state. In contrast, the pressure field gets extracted using the pressure-based approach by solving a pressure or pressure correction equation generated by manipulating continuity and momentum equations (Ansys Inc, 2009).

Pressure-Based Solver

In the current investigation, the pressure-based solver is more appropriate. The pressure-based solver employs an algorithm from the projection approach, which encompasses a wide range of techniques. The mass conservation condition of the velocity fields gets achieved in the projection approach by solving a pressure equation. The pressure equation gets derived from the continuity and momentum equations in such a way that the corrected velocity field fulfils the continuity. Because the governing equations are nonlinear and coupled, the solution process entails iterations in which the entire set of governing equations gets solved repeatedly until the solution converges. Pressure-based solver algorithms are generally classified into two types: segregated algorithms and coupled algorithms. These two techniques are addressed in depth in the sections that follow. (Ansys Inc, 2009).

Segregated algorithm

In the current investigation, the pressure-based solver is more appropriate. The pressure-based solver employs an algorithm from the projection approach, which encompasses a wide range of techniques. The mass conservation condition of the velocity fields gets achieved in the projection approach by solving the pressure-based solver utilizing a solution algorithm to solve the governing equations sequentially (segregated from one another). Because the governing equations are nonlinear and coupled, the solution loop must be repeated to yield a convergent numerical solution. The segregated algorithm gives the separate governing equations of the solution variables one at a time. As a result, while being solved, each governing equation is "decoupled" or "segregated" from

the others, hence the term. Because discretized equations only need to be held in memory one at a time, the segregated technique saves memory. However, because these equations get calculated separately, the convergence of the solution is extremely slow, the phases of the separated algorithm as depicted in **Figure 45**. (Ansys Inc, 2009).

Coupled algorithm

The coupled method, as opposed to the segregated algorithm mentioned above, solves a coupled system of equations that includes the momentum and the pressure-based continuity equations.

Because the momentum and continuity equations get solved in a tightly coupled manner, the rate of solution convergence improves considerably over the segregated technique. However, the memory consumption is higher than that of the segregated technique because when solving for velocity and pressure fields, the discrete system of all momentum and pressure-based continuity equations must be kept in memory. The steps of the coupled algorithm as depicted in **Figure 45**. (Ansys Inc, 2009).

Density-Based Solver

The density-based solver simultaneously solves the governing equations of continuity, momentum, energy, and species transport (coupled together). Following that, the governing equations for more scalars will be solved sequentially (segregated from one another and the coupled set). Because the governing equations are nonlinear, the solution loop must be iterated several times before a convergent solution is found. Figure 46 displays the steps involved in each repetition (Ansys Inc, 2009).

The discrete, non-linear governing equations are linearized in density-based solution techniques to give a system of equations for the dependent variables in each computing cell. The linear system results are then solved to get an updated flow-field solution. Regarding the dependent variable of interest, linearization can be implicit or explicit. The unidentified value in each cell of an implicit for a particular variable gets calculated using a relation that incorporates both existing and unknown values from surrounding cells. As a consequence, each unknown in the system will appear in a series of equations that must be solved concurrently to provide the unknown integers. The unidentified value in each explicit cell gets generated using a correlation that only contains existing values for a specific variable. As a consequence, each unknown in the system will be represented by a single equation, and the equations for the unknown values in each cell may be solved one by one to obtain the unknown numbers (Ansys Inc, 2009).

Pressure-velocity coupling

There are five pressure-velocity coupling algorithms in ANSYS FLUENT: SIMPLE, PISO, Coupled, SIMPLEC, and Fractional Step Method (FSM), although only the first three will be described in this section. The pressure-based segregated approach is used by SIMPLE, SIMPLEC, PISO, and the Fractional Step Method, whereas the pressure-based coupled solution is used by coupled. All of the previous systems, except the "coupled" scheme, use the predictor-corrector approach. (Ansys Inc, 2009).

SIMPLE

SIMPLE is the ANSYS FLUENT default scheme. Pressure fields in the SIMPLE algorithm are obtained by a linear correlation between the velocity and pressure adjustments to enforce mass conservation. After the pressure-adjustment equation is solved, the new velocities will not satisfy the momentum balance. so, a repetitive calculation will be needed until the balance is satisfied (Ansys Inc, 2009).

PISO

PISO is an extension of the SIMPLE method, which is used to solve the Navier-Stokes equations in computational fluid dynamics, and is based on a greater degree of approximation between the pressure and velocity adjustments. The PISO algorithm's fundamental principle is to replace the SIMPLE's repetitive computations as aforementioned. To improve the efficiency of PISO algorithm, two additional adjustments are performed: skewness adjustment and neighbour adjustment. Skewness adjustment considerably decreases the challenges associated with extremely distorted meshes in terms of convergence. Skewness adjustment enables ANSYS FLUENT to solve a heavily skewed mesh in roughly the same number of iterations as a more orthogonal mesh. Although neighbour adjustment takes a bit longer each solver iteration, it can drastically reduce the number of iterations necessary for convergence, particularly for transient problems (Ansys Inc, 2009).

Coupled Algorithm

The coupled technique outperforms the separate approach in various ways. The coupled scheme outperforms segregated solution techniques in terms of resilient and efficient single-phase implementation for steady-state flows. This pressure-based coupled algorithm is a solution to the pressure-based segregated algorithms with SIMPLE-type pressure-velocity coupling. When

dealing with transient flows, the coupled approach is necessary when the mesh quality is inadequate or when using long time steps (Ansys Inc, 2009).

CHAPTER 3: RESEARCH METHOD

This investigation's methodology is primarily based on the use of numerical methods (CFD) to simulate crude oil entrainment. This methodology is not purely numerical because, to validate the numerical method, the number obtained and the experimental test result must be compared. The physical model of Hartenberg and O'Hern (2011) was used for numerical method validation. The assumption was that if the outcomes were adequate and consistent with the observations, the remaining simulations would be equally valid. This chapter highlights specific methods used in the current investigation. This Chapter is made up of three main sections. *Section 3.2: Experimental Setup,* an experimental setup by Hartenberg & O'Hern (2011) is outlined in this section. *Section 3.3: Experimental Procedure*, the experimental procedure by Hartenberg & O'Hern (2011) is outlined in this section. Lastly, *Section 3.4: Simulation*, simulation method used in the current investigation is described in this section. Geometry, meshing, physics of the model and boundary conditions of the simulation are also outlined in this section.

3.1 Experimental Setup

A typical Strategic Petroleum Reserve (SPR) salt cavern is 609.6 meters deep, 60.96 meters in diameter, and can carry one and half million cubic meters of crude oil. The experiment was reduced to laboratory size. The diameter of the siphon in the SPR caves was compared to the diameters of the three laboratory-sized siphons for geometric scaling.

The experimental setup by Hartenberg and O'Hern (2011) in the laboratory is depicted in **Figure 16**. A hexagonal testing tank made of glass that was 60.96 cm deep and has sides that were 25.4 cm wide. A cylindrical separation tank 70 cm deep and 20 cm in diameter was used to separate any silicon oil that has become entrained in the water. On a returning pipe between the testing and separation tanks, a Zoeller High-Capacity Pump and a GPI electronic digital flow meter were installed. To trace the movement of the liquid-liquid interface, a Linear Variable Displacement Transducer (LVDT) was installed on the siphon between the separation and testing tanks and was zeroed at the undisturbed interface. Two Redlake MotionPro cameras were installed on the side of the testing tank, 120° apart, to capture digital videos from the start of the test until silicon oil entrainment began. Two different withdrawal tube orientations were used. In the primary orientation, a siphon is passed through the 2.54 cm layer of silicon oil and faces downward below the liquid-liquid interface, drawing water upwards, as shown in **Figure 17**. The siphon withdraws

directly from the water without passing through the liquid-liquid interface in the secondary orientation, and the water is drawn downwards.

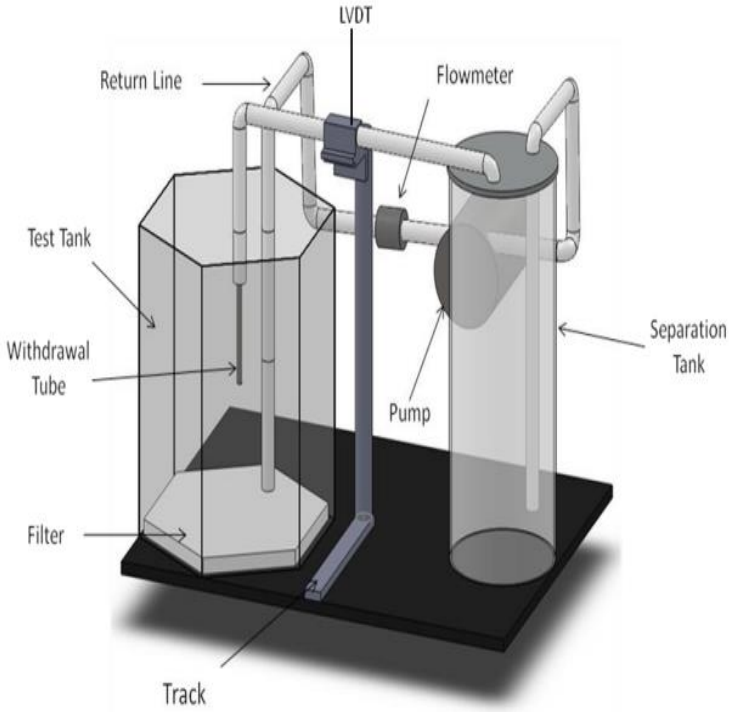


Figure 16: Experimental setup of the hexagonal testing tank (Hartenberg & O'Hern, 2011).

Each siphon orientation had a submergence depth of 2.54 cm below the liquid-liquid interface. Three different diameter siphons were used, as well as six different liquid pairings. A ring tensiometer was used to determine the interfacial tension between each liquid pairing. All experiments began with the siphon being centred in the tank and the inlet being perpendicular to the undisturbed liquid-liquid interface. Before carrying out the entire set of experimental experiments, several preliminary tests were carried out to ensure the quality of the flows. The "quality of the flows" refers to the fluid's characteristics, including magnitude, frequency, timing, and duration, which can determine the quantity and quality of the fluid being measured. To develop high-quality flows in the test section, it is essential to ensure the reliability and functioning of the flow conditioning unit. Various factors, including the reliability and functioning of the flow conditioning unit, can affect the quality of the flows. The quantity and quality of the flows can be determined using various means, including dye testing. Dye testing is a method used to visualize the flow and check the accuracy of a flow meter, correcting for repeatable, systematic biases in a flow measurement. The quantity and quality of the flows can be determined using various means, including dye testing (Baker, 1990; Bert *et al.,* 2022; CPA, 2019; Engel & Baade, 2015). In

Hartenberg & O'Hern, (2011) investigation, the quality of flow was done in two steps: dye injection and layer thickness. Firstly, dye injection tests revealed that the filter distributor produced a uniform, gently increasing flow inside the test tank that had no discernible effect on the flow at the liquid-liquid interface or near the siphon. Second, the thickness of the silicon oil layer was gradually reduced to assess its impact on the conditions that caused the system to switch to light layer entrainment. Layer thicknesses ranging from 5.08 cm to 0.3175 cm had no effect. in **Figure 17**, $\boldsymbol{S}$ is the submergence depth, $\boldsymbol{d}$ is the diameter of the siphon, $\boldsymbol{Q}$ is the fluid flow rate and $\boldsymbol{\gamma}$ is the liquid-liquid interface.

3.2 Experimental Procedure

Before each experimental trial, certain systematic actions were carried out. To begin, an LVDT was utilized to zero out the siphon end at the liquid-liquid contact to provide a consistent point of reference. The siphon was then lowered by at least 2.54 cm using a micrometre to ensure that the system began each trial in a state of selective withdrawal. Second, using the two cameras, the alignment of the siphon was checked to ensure that each trial had a level siphon orientation (siphon opening orientated normal to gravity).

Each trial started with a constant rate of flow through the system. The flow rate was adjusted using a variable controller on the pump. Upon the measurement of the flow rate, the MotionPro cameras were activated and video began, while the siphon was gradually raised by 250 μm increments using a micrometre. The step size was reduced to 25 μm as the circumstances approached transition. A disturbance could be observed when the tube aperture approached the liquid-liquid contact.

The liquid-liquid interface disruption presented itself as a sunken annulus encircling the siphon in the primary siphon direction, which gradually got more peaked until silicon oil entrainment commenced. Until silicon oil entrainment occurred, the liquid-liquid interface disturbance for the secondary siphon orientation resembled a conic hump.

When the system transitioned to silicon oil entrainment, the flow rate and submergence depth of the siphon were recorded, and the video recordings were stopped. The pump was turned off and a valve between the test tank and the separation tank was closed to minimize the amount of silicon oil drawn into the separation tank. The silicon oil that had been entangled in the connecting line was emptied back into the testing tank, where it quickly coagulated. When the separation tank was cleaned, the air was fed into both the withdrawal pipe and the separation tank.

Because the system relied on a pump after the separation tank, water had to be delivered to both the separation tank and the withdrawal line. After the oil withdrawal line was cleansed, water was suctioned into the separation tank and partially into the vacuum line through the withdrawal line. Water from the vacuum line was returned to the testing tank and settled back into the system. The withdrawal siphon location and direction were re-zeroed and, if necessary, modified in preparation for the next test after analysing and recording the images on the camera.

According to Hartenberg and O'Hern (2011), about 350 experimental trials were conducted due to a large number of experimental variables. The test tank was first filled with a liquid pairing. After that, one of the siphons was added to the system. Second, several flow rates were investigated, often beginning with the lowest achievable stable flow rate and gradually increasing the flow rate in 3.79 LPM increments until the maximum achievable flow rate was achieved. After completing one set of trials, the withdrawal tube would be replaced until all potential trials for the liquid pairing were completed. After that, the test tank was thoroughly cleaned, and the next liquid pairing was added until all of the experimental tests were completed.

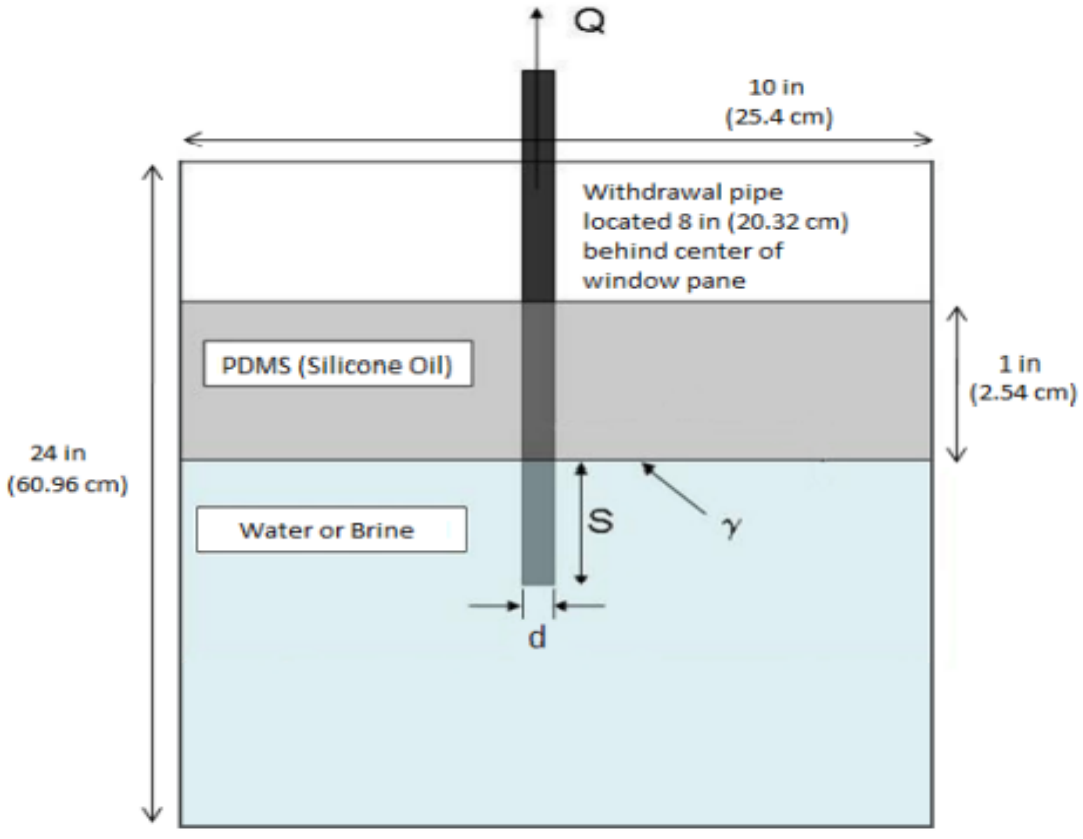


Figure 17: Testing tank as viewed through a windowpane (Hartenberg & O'Hern, 2011).

3.3 Numerical method

A numerical investigation of selective withdrawal of brine from salt cavern with entrainment of the light phase oil was carried out using the CFD programme. The simulation was done using Ansys Academic Student 2021 R1. Ansys Academic Student 2021 R1 was downloaded and installed on a 64-bit computer system for the simulation. To begin the simulation, workbench-fluent was used. Workbench-Fluent is divided into Geometry, Meshing, Setup, Solution and Results.

3.3.1 Geometry

The initial phase in the simulation process is to produce design models, which are required for product development. These models can be geometric forms that reflect genuine design details, or they can be design approximations that employ simpler components like beams and plates. Geometry is not only a vital component of engineering simulation; it also combines engineering simulation with design and production, and so plays a key role in simulation. The geometry may be built or imported in Ansys Workbench. Since appropriate geometry was not obtainable in the current investigation, the geometries were constructed from scratch.

There are two models to create geometry in the Workbench, namely: Design-Modeler and Space-Claim. Space-Claim is fast and simple but comprehensive 3D modeling software.

Design-Modeler was used in the current investigation (Ansys Inc, 2012; Ansys Inc, 2013). The decision to use DesignModeler was based purely on comprehensive training platforms available online to familiarise ourself with tools related to analysis in Ansys Workbench. Ansys DesignModeler offers unique simulation modelling functions such as parametric geometry creation, concept model creation, Computed-Aided Design (CAD) geometry modification, automated cleanup and repair, and several custom tools designed for fluid flow, structural, and other types of analyses. Before beginning a new model in the DesignModeler application, you are presented with three mutually perpendicular planes, which correspond to the three mutually perpendicular planes in the Cartesian coordinate system (the XY plane, the YZ plane and the ZX plane). You must define a feature on a plane before using a sketch to create it. Every sketch is attached to a distinct plane. At any given time, only one sketch may be worked on (Ansys Inc, 2012; Ansys Inc, 2013).

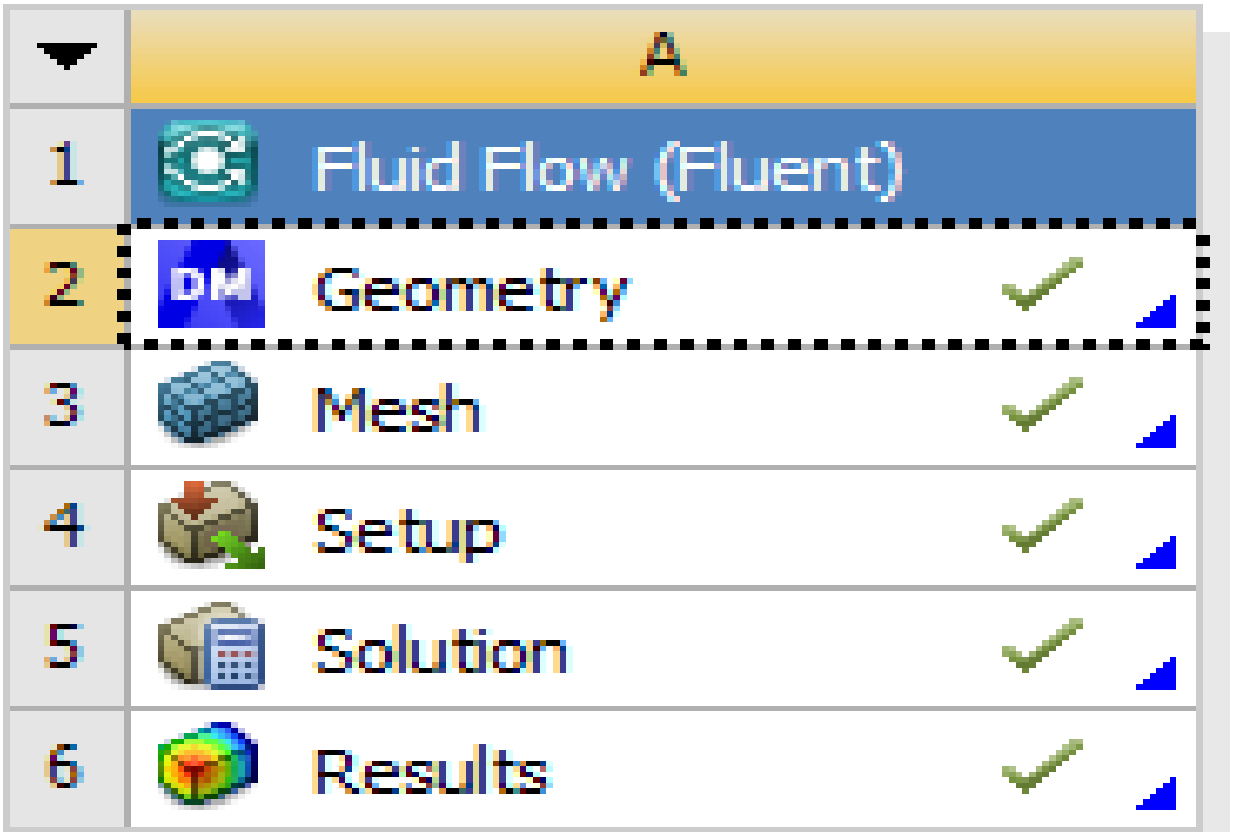
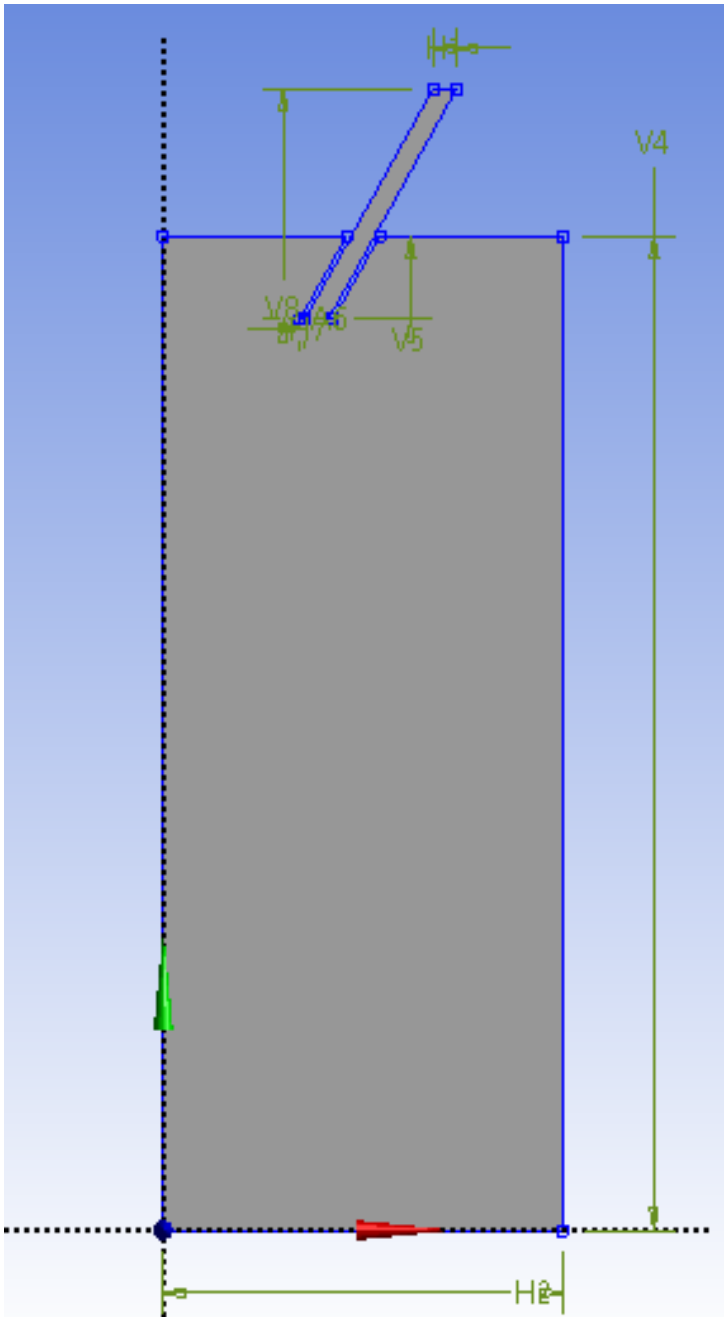


Figure 18: Successful completion of geometry, Meshing, Setup & Solution and postprocessing which was indicated by the green tick.

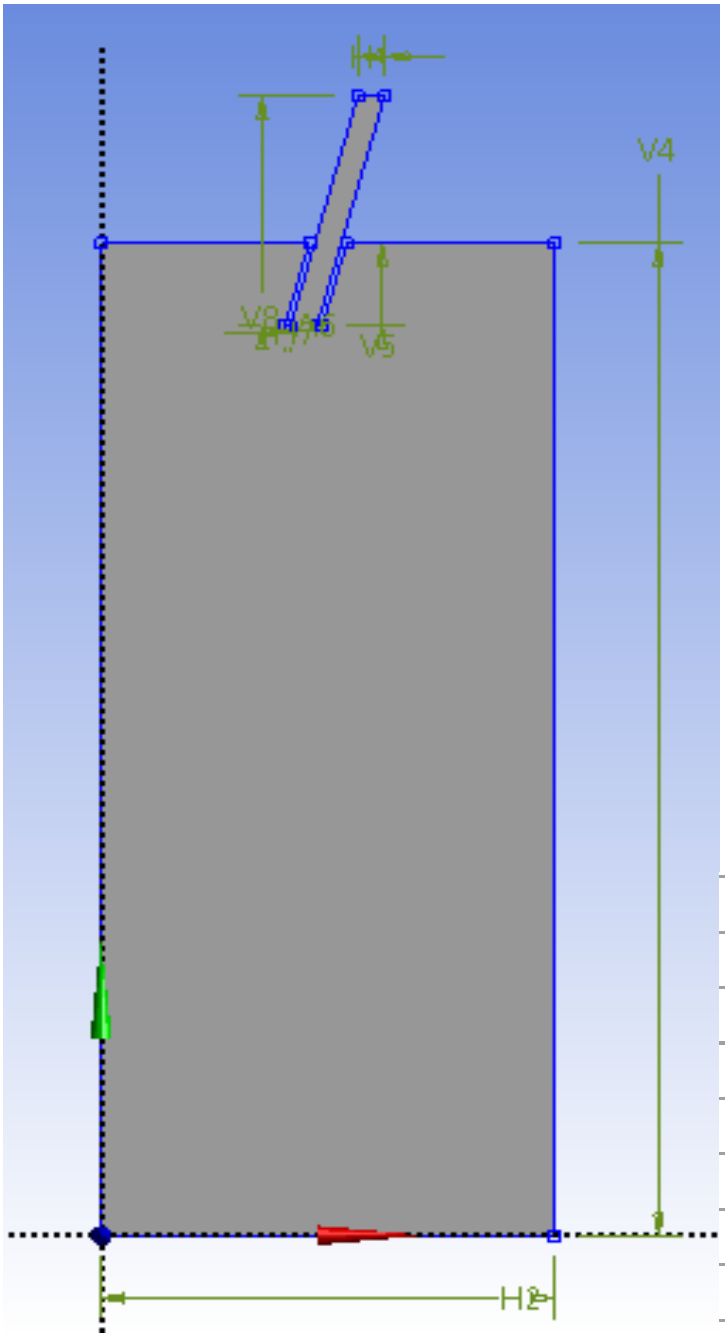
The simulation was a 2-D Geometry as shown in **Figures 19, 20 and 21**. Dimensions used in the simulation are the same as the ones used in the experimental investigation by Hardenberg and O'Hern (2011) which is shown in **Figure 17**. The geometries were sketched using Design-Modeler of the Ansys 2021 R1 and steps to were as follows: The workbench was opened by clicking on ***the "Workbench"*** icon then double-clicking on ***"Fluid Flow (Fluent)"***. ***"Design Modeler"*** was opened by right-clicking on **"Geometry"** and then clicking ***"New Design Modeler Geometry"***. After ***"Design Modeler"*** has opened, the units of geometry were changed to cm by clicking on ***"Units"***. The axis (X, Y plane) of the geometry was selected. ***"Sketching"*** toolbox and ***"Draw"*** were clicked respectively to sketch the geometry. Modify, Dimensions and Constraints were used to perfect the geometry.



Dimensions: 7	
A6	60 °
H1	1,5 cm
H2	25,4 cm
H7	0,3 cm
V4	60,96 cm
V5	5,08 cm
V8	14,12 cm

Figure 19: Geometry and dimensions of salt cavern with 60º inclined siphon from Design-Modeler of Ansys 2021 R1.

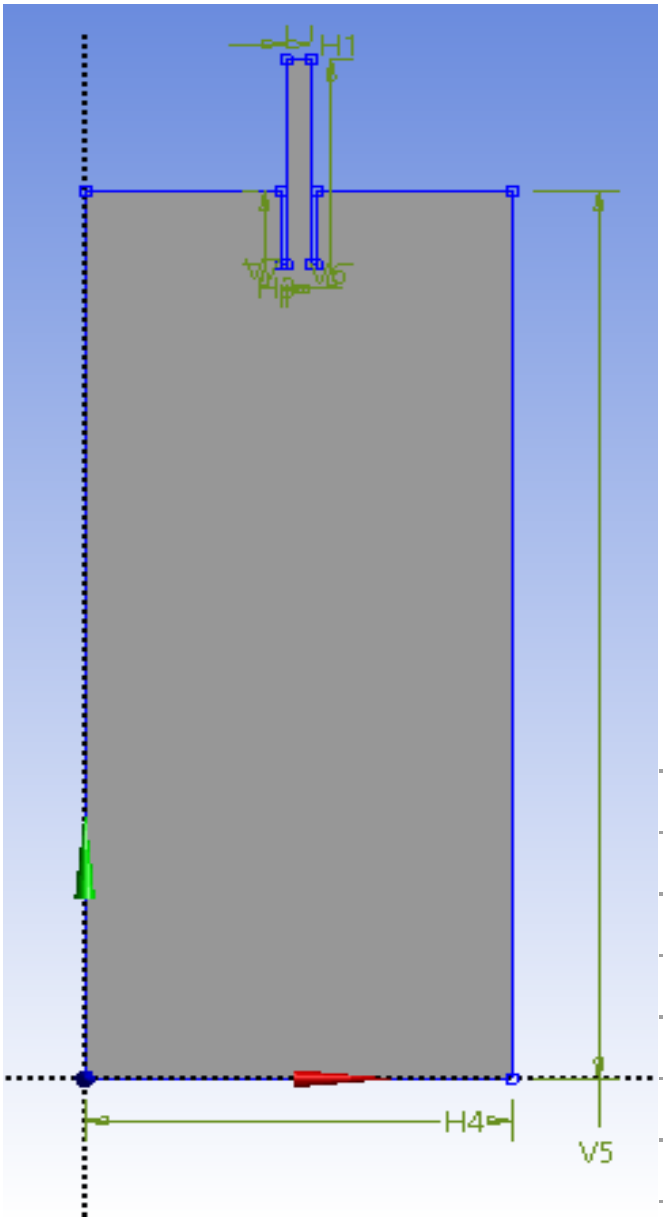
"Modify" was used to trim, extend, drag and corner the geometry. ***"Dimensions"*** was used to specify the dimensions of horizontal, vertical, length/distance and angles of the geometry. ***"Constraints"*** was used to adjust the lines of the geometry to be horizontal, vertical, equal length/distance, parallel, midpoint and perpendicular.



Dimensions: 7	
A6	75 °
H1	1,5 cm
H2	25,4 cm
H7	0,3 cm
V4	60,96 cm
V5	5,08 cm
V8	14,12 cm

Figure 20: Geometry and dimensions of salt cavern with 75º inclined siphon from DesignModeler of Ansys 2021 R1.

To complete the geometry**, *"Concept"*** was clicked then ***"Surface sketches"***, Click on the geometry itself then click on ***"apply"***. Lastly, ***"generate"*** was clicked to complete the geometry. Completed geometries with their dimensions are shown in **Figures 19, 20 and 21**. ***"Geometry"*** on the workbench will tick green to show the geometry was successfully created and ready for meshing as shown in **Figure 18**.



Dimensions: 6	
H1	1,5 cm
H3	0,3 cm
H4	25,4 cm
V5	60,96 cm
V6	14,12 cm
V7	5,08 cm

Figure 21: Geometry and dimensions of salt cavern with 90º inclined siphon from DesignModeler of Ansys 2021 R1.

3.3.2 Meshing

Ansys' meshing solutions range from simple automatic meshing to highly tailored meshing. Methods range from high-order to linear elements, as well as quick tetrahedral and polyhedral meshing to high-quality hexahedral and mosaic meshing (Ansys Inc., 2010). Nodes will be present only at the corners of a linear element or a first-order element. A Second-order element or a Quadratic element, on the other hand, will have nodes in the middle as well as nodes at the corners.

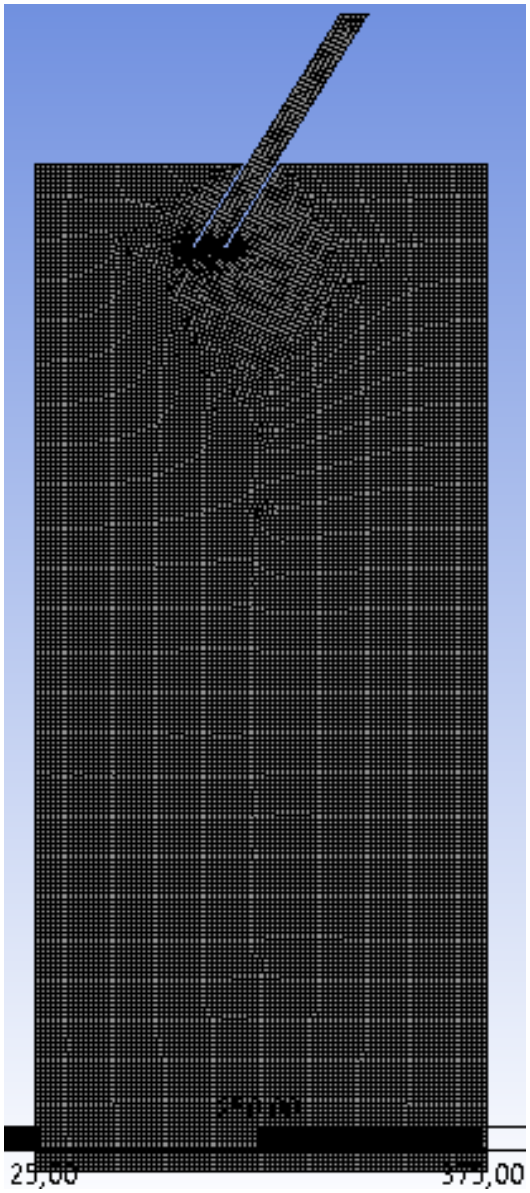


Figure 22: Mashed geometry of salt cavern with 60º inclined siphon from Meshing-Modeler of Ansys 2021 R1.

In the current investigation, the mesh type used was hexahedral elements in conjunction with the first-order element or linear element which is recommended for simple 2D geometry. If linear hexahedral elements are used, the number of nodes will be twice the number of elements. Ansys Academic Student 2021 R1 has a limitation to the maximum of 20000 meshing elements. Mesh elements size and inlet edges size in the current investigation were 3 mm and 0.033mm respectively. In results of the element size and inlet edges size mentioned above, the geometry with 60º inclined siphon had 19843 elements and 40634 nodes, a geometry with 75º inclined

siphon had 19871 elements and 40676 nodes, and geometry with 90^{o} siphon had 17918 elements and 36574 nodes. The inclined angle of the siphon influences the number of elements and nodes with 90^{o} siphon being the lowest among the three. Meshed model is shown in **Figures 22, 23 and 24.**

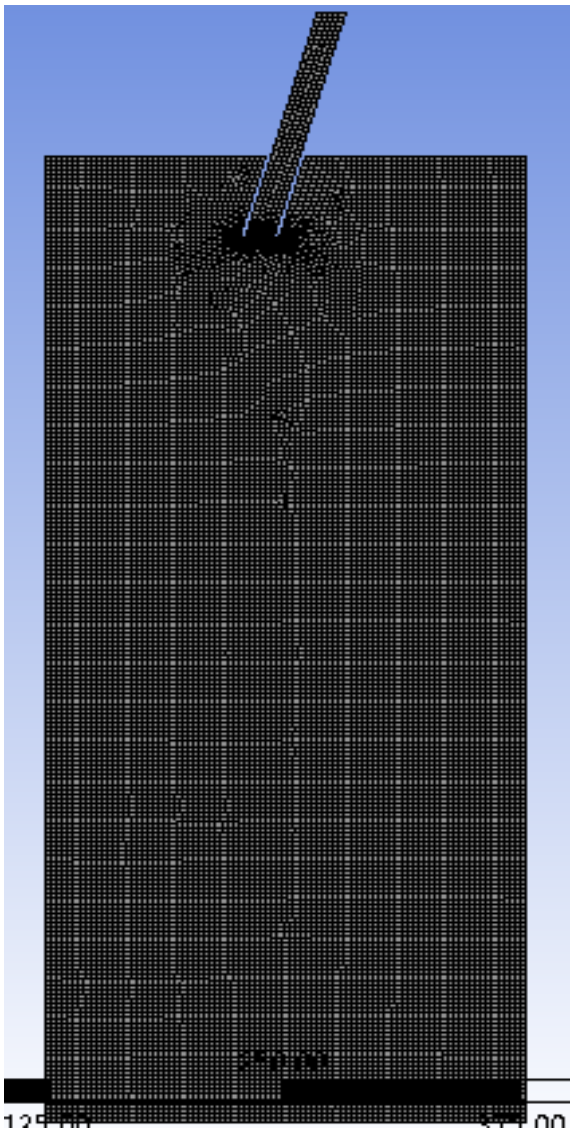


Figure 23: Mashed geometry of salt cavern with 75^{o} inclined siphon from Meshing-Modeler of Ansys 2021 R1.

"Mesh" was double-clicked on the Workbench and waited until the Mesh screen was opened and the geometry was loaded. Right-click on the mesh and generate the mesh. Mesh elements size and inlet edge size were reduced to 3 mm and 0.033 mm respectively. The boundaries (inlet, outlet, free surface and wall) were specified by right-clicking the boundary and choosing ***"selection***

name" to type in boundary name then updating the mesh. Smaller elements in a mesh mean more elements, which means more accuracy. However, as more elements are added, more equations must be solved at each time step, increasing both solution time and memory requirements. High mesh density requires more disk space to store the results. In this simulation as shown in **Figures 22, 23 and 24**. High mesh density was restricted to the area of interest, which is on the inlet edges, to improve accuracy, reduce solution time, and avoid large result files.

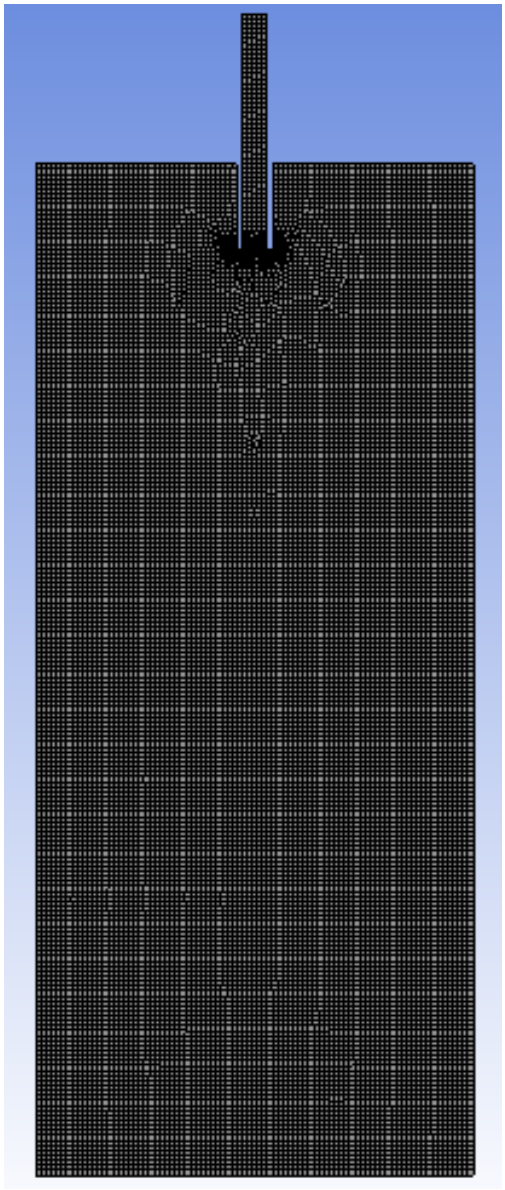


Figure 24: Mashed geometry of salt cavern with 90º inclined siphon from Meshing-Modeler of Ansys 2021 R1.

3.3.3 Setup and Solution

Both the Setup and Solution are the third step of the simulation and CFD analysis was set up using Ansys Fluent. The setup and solution were launched after the geometry and mesh were created as discussed in the previous sections.

FLUENT Launcher

The ***setup*** cell on the workbench was double-clicked and FLUENT Launcher was displayed. ***2D*** from dimension, ***Double Precision*** from options, ***Serial*** from processing options were enabled. Lastly, ***Display Mesh After Reading***, ***Embed Graphics Windows***, and ***Workbench Color Scheme*** from display options were enabled before pressing ***Ok***. The aforementioned is shown in **Figure 25**.

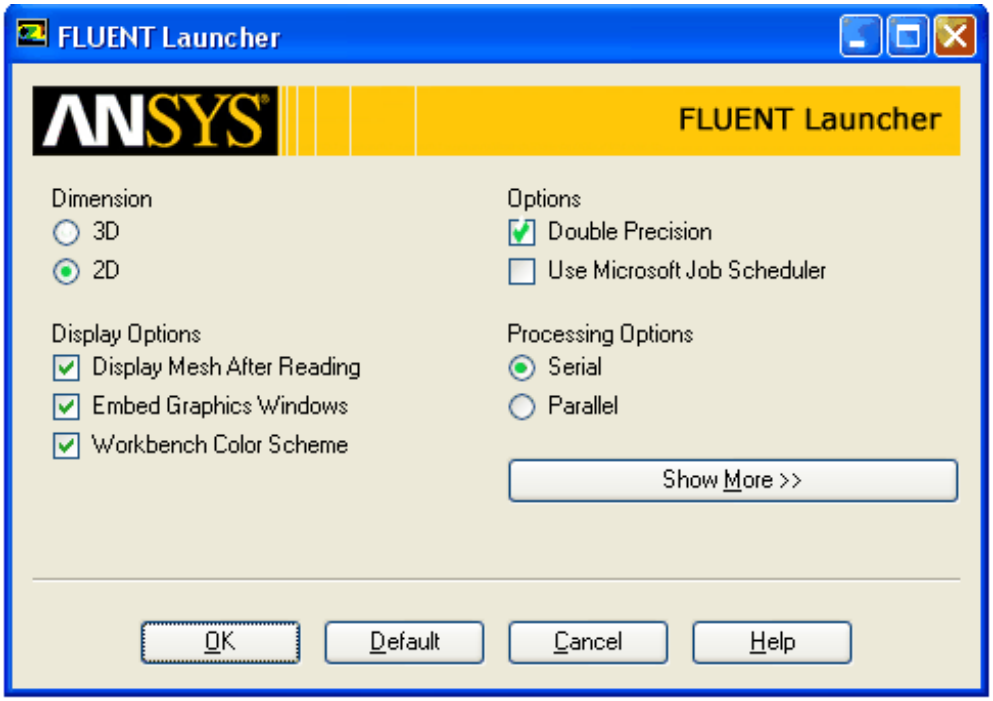


Figure 25: ANSYS Launcher.

They're some of the parameters were changed and some others were left as default. General settings, models setting, materials, boundary conditions and solutions were discussed below.

General Settings on ANSYS FLUENT

Firstly, the meshed geometry automatically uploaded and displayed. In this subsection, general settings were made using the task pages listed under the ***General*** heading. Under the general setting, ***Pressure-Based*** solver type, ***Absolute velocity*** formulation, ***Transient*** time and ***Planar***

were selected as shown in **Figure 26**. Gravitational acceleration of -9.81 m/s^2 was filled in the y-axis cell.

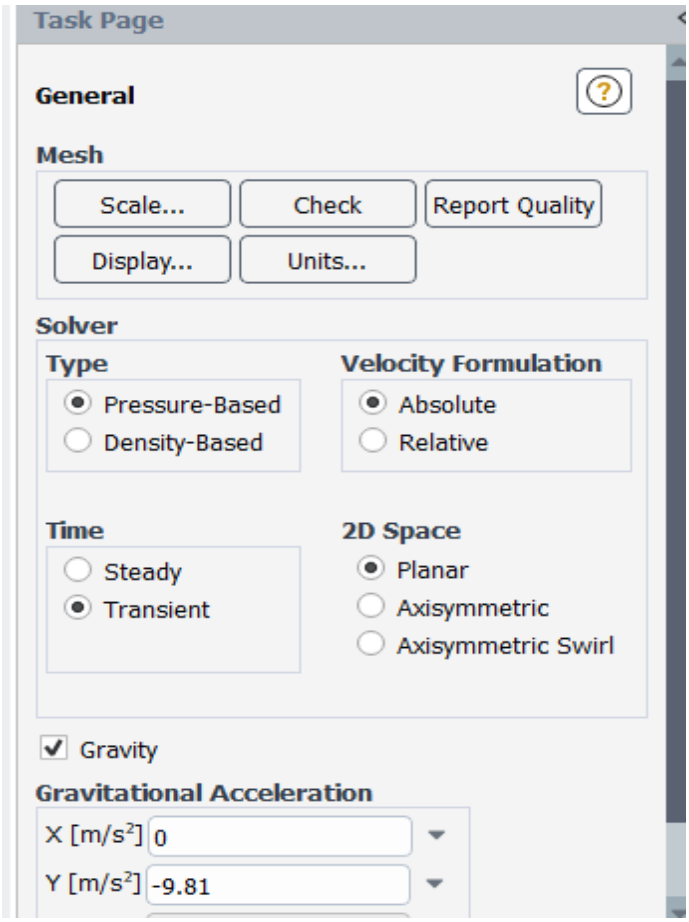


Figure 26: General Settings on ANSYS FLUENT.

Setting Models on ANSYS FLUENT

In this subsection, applicable models were selected using the task pages listed under the ***Models*** heading. The ***Multiphase Model*** was double-clicked and displayed. ***Volume of Fluid*** was selected and then clicked apply. Phases were defined in the following section. ***Surface Tension Force Modeling*** and ***Wall Adhesion*** were selected. Under Surface Tension Coefficient, the surface tension coefficient between water and silicon oil remained unchanged throughout the simulation at 0.04 N/m. Viscous (standard k-epsilon) was used. The settings of Multiphase Model are shown in **Figure 27**.

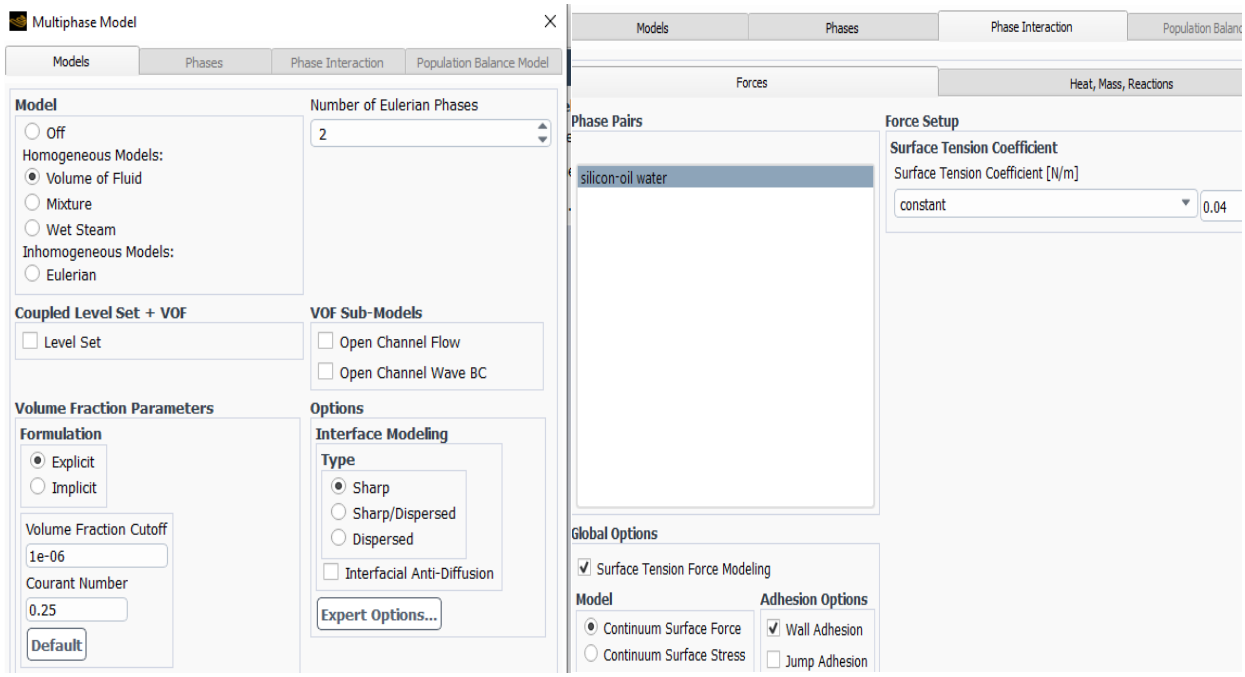


Figure 27: Setting of Multiphase Model in ANSYS FLUENT.

Creating new materials on ANSYS FLUENT

In this subsection, materials were defined using the task pages listed under the ***Materials*** heading. Water and silicon oil were created using the ***Create/Edit Materials*** dialogue box. These two phases were defined. Silicon oil and water were defined as primary and secondary phases respectively. The properties of the two phases were also defined and these properties are mentioned in **Table 4** in **APPENDIX B.**

Input Coordinates on ANSYS FLUENT

In this subsection, coordinates of water in the geometry were defined. Click on ***Adapt***, ***Manual***, ***Cell registers***, ***New*** and lastly ***region***. The coordinates on the X-axis and Y-axis were inserted as shown in **Figure 28.** Only two axes were used because the geometry is two dimensions.

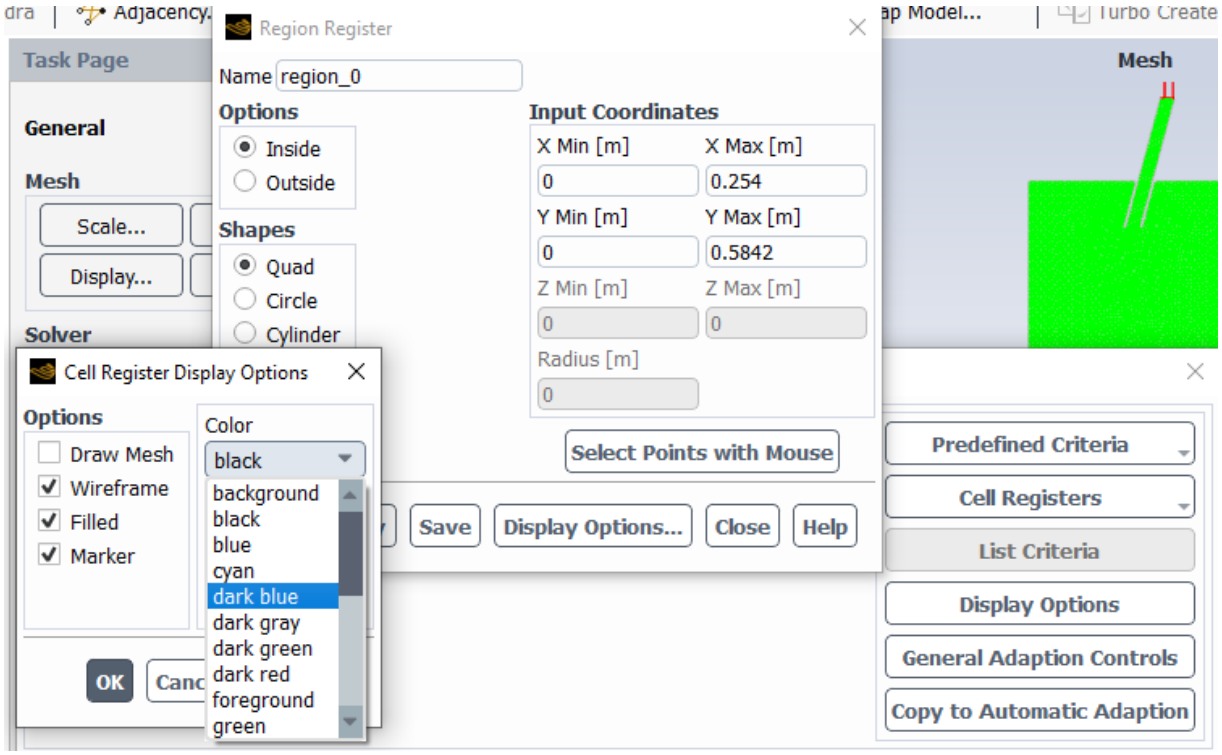


Figure 28: Input Coordinates on ANSYS FLUENT.

Set up of boundary conditions on ANSYS FLUENT

In this subsection, boundaries were defined using the task pages listed under the ***Boundary Conditions*** heading. The simulation model inputs are defined by boundary conditions. Some parameters, such as velocity and volumetric flow rate, govern how a fluid enters and exits the model. The simulation model is linked to its surroundings by boundary conditions. Without them, the simulation lacks definition and, in most cases, cannot continue. The majority of boundary conditions are either steady-state or transient in nature. Throughout the simulation, steady-state boundary conditions exist. Transient boundary conditions change over time and are commonly used to simulate an event or cyclical phenomenon.

Pressure inlet and outlet boundary conditions were adopted for inlet and outlet respectively. The gauge pressure at the siphon outlet was set to -1914 Pa, negative pressure for suction to take place. The free surface was defined as the pressure inlet of the siphon. No-slip and no-penetration wall conditions were used at the solid walls. Two phases were used in the simulation, namely; the primary phase and the secondary phase. Silicon oil was defined as the primary phase and water as the secondary phase. The backflow fraction was set to zero because the secondary phase is not needed initially on the outlet.

Set up of solution for the CFD analysis

In this subsection, setting up and running the calculation using the task pages listed under the Solution heading. ***SIMPLE*** solution method and ***Hybrid initialization*** solution were used for the Solution before running the simulation. After the simulation had converged, both the setup and solution cells will tick green.

A pressure-based solver (pressure-based segregated algorithm) was used in this simulation. An algorithm employed in the pressure-based solver is based on an approach known as the projection method. This method involves solving a pressure equation to satisfy the constraint of mass conservation (continuity) in the velocity field, by integrating the continuity equation and the momentum equation, one obtains the pressure equation which takes into account the pressure for the velocity field to satisfy continuity. Although the governing equations are not linear and coupled, the solution process involves iterations, in which the entire set of equations was solved repeatedly until the solution was obtained (Chorin, 1968). Absolute velocity formulation was chosen precisely because most of the flow in the domain is not rotating. In double-precision, the calculation will be more accurate than single-precision because it will be represented by a 64-bit system. the specified period will require time input in transient time. Lower time steps and a higher number of timesteps improve accuracy. Timestep of 0.00001 and 3000 number of steps will give 0.030s.

Reynolds-average Navier-Stokes equation (RANS) is used to solve/model turbulent flows. RANS models are thought to be more cost-effective and practical for engineering design applications, requiring fewer computational resources. RANS is divided into four models: the zero-equation model, the one equation model, the two-equation model, and the stress equation model. The models chosen are influenced by factors such as the physical flow, the level of accuracy, and the computational resources available (Hasan & Hayder, 2021). The most commonly used turbulence model in CFD is standard *k*-epsilon. This type of turbulence model is based on the eddy viscosity concept and solves two equations: turbulent kinetic energy *k* and turbulent eddy dissipation ε. In some unconfined flows, swirling flows, rotating flows, and anisotropic flows, standard *k*-epsilon performs poorly. Despite known limitations, standard k-epsilon outperforms in some curved channels, predicts well away from the wall, is robust, simple to implement, computationally cheap, and widely used (Alfonsi, 2009; Shaheed *et al*., 2018). Based on the aforementioned factors, standard *k*-epsilon was chosen as the best RANS model for the current investigation. Semi-Implicit

Method for Pressure Linked Equations (SIMPLE) algorithm by Ahmad and Hashid, (2020) was adopted for pressure velocity coupling.

Lastly, after the simulation was successfully converged, the results of the simulation were evaluated using CFD-Post Processing Modeler from the Ansys Workbench. Post-processing computational fluid dynamics (CFD) is critical step for obtaining accurate results and make sensible conclusion from the models. CFD-Post Processing assists in the extraction of graphics and statistical data, the generation of additional tables and charts for various parameters, and the creation of animations related to the project at hand.

CHAPTER 4: RESULTS AND DISCUSSION

In the preceding chapter (chapter 3), the simulation methodology employed in this research report was described. The results and discussions of the aforementioned simulation method used to numerically investigate the selective withdrawal of brine from a salt cavern with entrainment of the light phase oil are presented in this chapter. The simulation results are compared to the results of the experimental study. This chapter comprises four primary sections. Section 4.2: Simulated Water-Silicon Oil Model. Secondly, Section 4.3: Vortex and Velocity in the Simulation. Then, Section: 4.4: The effect of Pressure and Velocity and lastly, Section 4.5: Calculated dimensionless Numbers.

4.1 Simulated Water-Silicon Oil Model

Figures 29, **30** and **31** illustrate a two-dimensional simulation of the water-oil model. The silicon oil represents crude oil and is represented by the red colour layer in the simulation. Water represents brine and is represented by the dark blue colour layer. The inlet opening was horizontal to both the bottom and top of the testing tank to limit early entrainment.

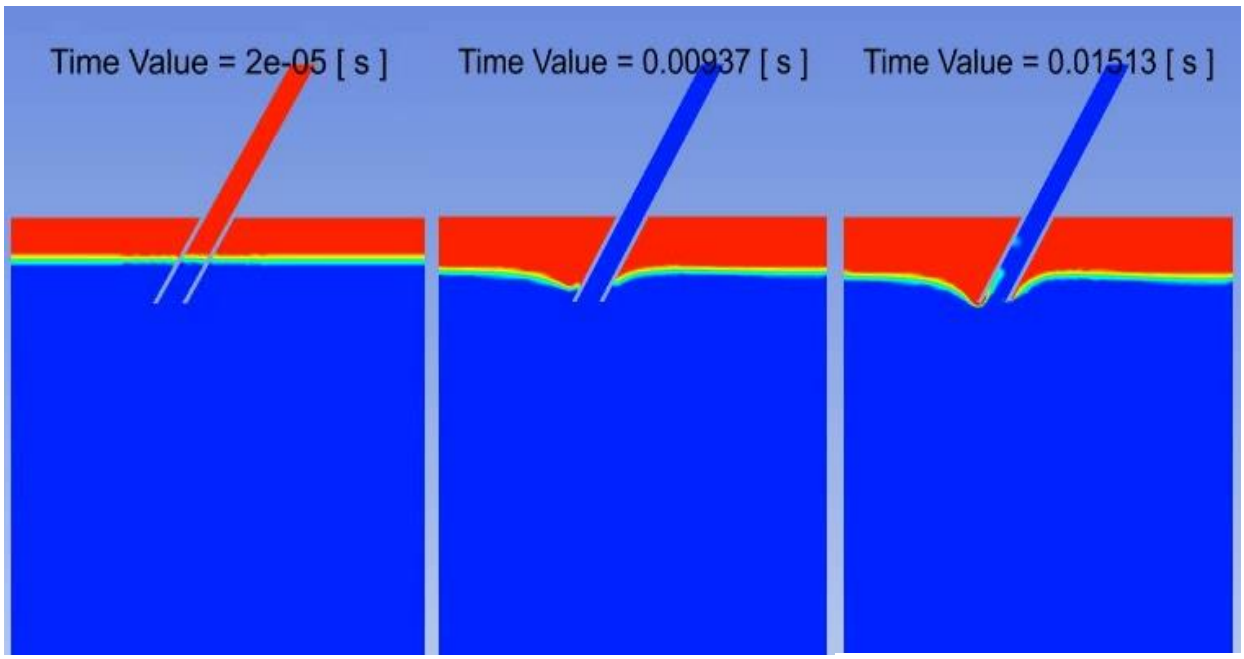


Figure 29: Simulated steps of the occurrence of oil entrainment at the 60º inclined siphon obtained from Ansys.

As time elapses the water is drawn out and the interface drops reaching the inlet of the siphon. As the interface drops, the submergence depth was also reduced. The reduction of submergence depth was not uniform in the testing tank. The reduction of the submergence depth was higher close to the siphon walls compared when submergence depth far away from the siphon walls. The deformation of the interface was not uniform around the 60^o and 75^o siphons and the oil entrainment starts from the left side of the siphons and later oil entrainment starts from the right of the siphon. The deformation of the interface around the 90^o siphon is uniform and starts from all sides of the siphon. The submergence depth of the siphon has been drastically reduced, resulting in interface deformation until critical submergence, this is shown in **Figures 29**, **30** and **31**. Critical submergence refers to the vertical distance between the inlet of a siphon and the interface when the interface starts to be drawn into the siphon from the upper layer elevation. When the critical submergence is low, it prevents early entrainment, which means that selective withdrawal is optimal. The critical submergence of 60^o, 75^o and 90^o are 1.10, 1.62 and 1.02 cm respectively. The decrease in pressure brought on by the velocity pulls the interface downward and reduces submergence depth, causing interface to distort. Buoyancy is most likely the source of the restoring force that prevents oil entrainment, whereas inertia is the driving factor behind oil entrainment. In both the 75^o and 90^o siphons, the interface appeared to drop down the siphon walls before being entrained at the inlet. However, the 60^o did not entrain in this manner, but rather through a vortex on the left side of the siphon.

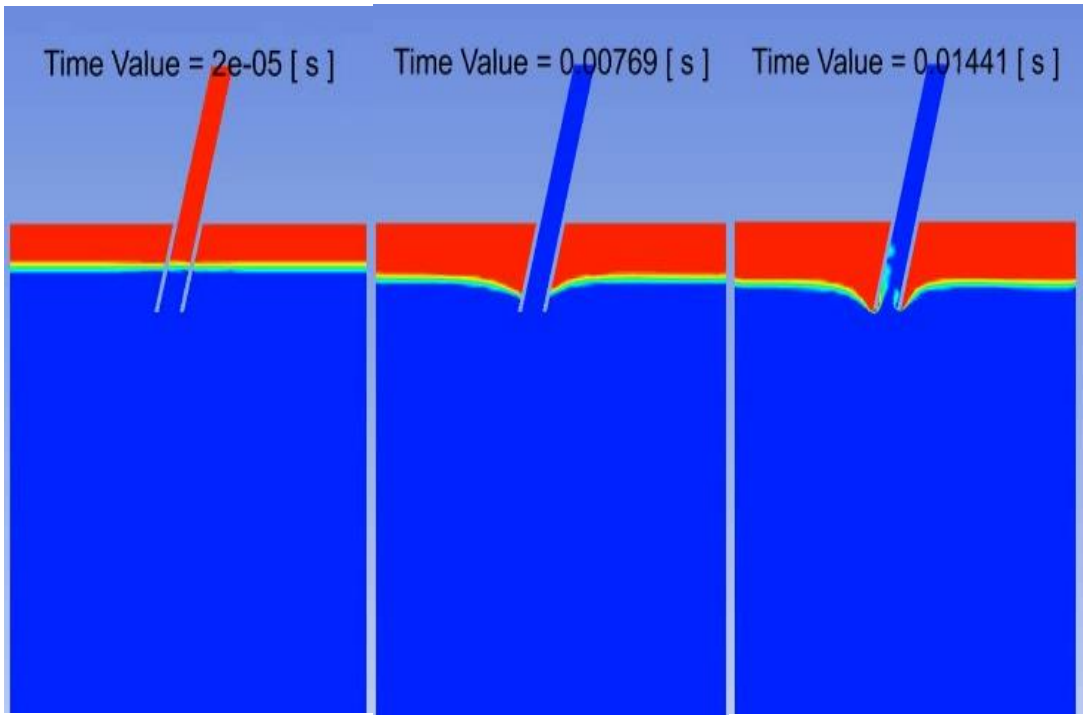


Figure 30: Simulated steps of the occurrence of oil entrainment at the 75º inclined siphon obtained from Ansys.

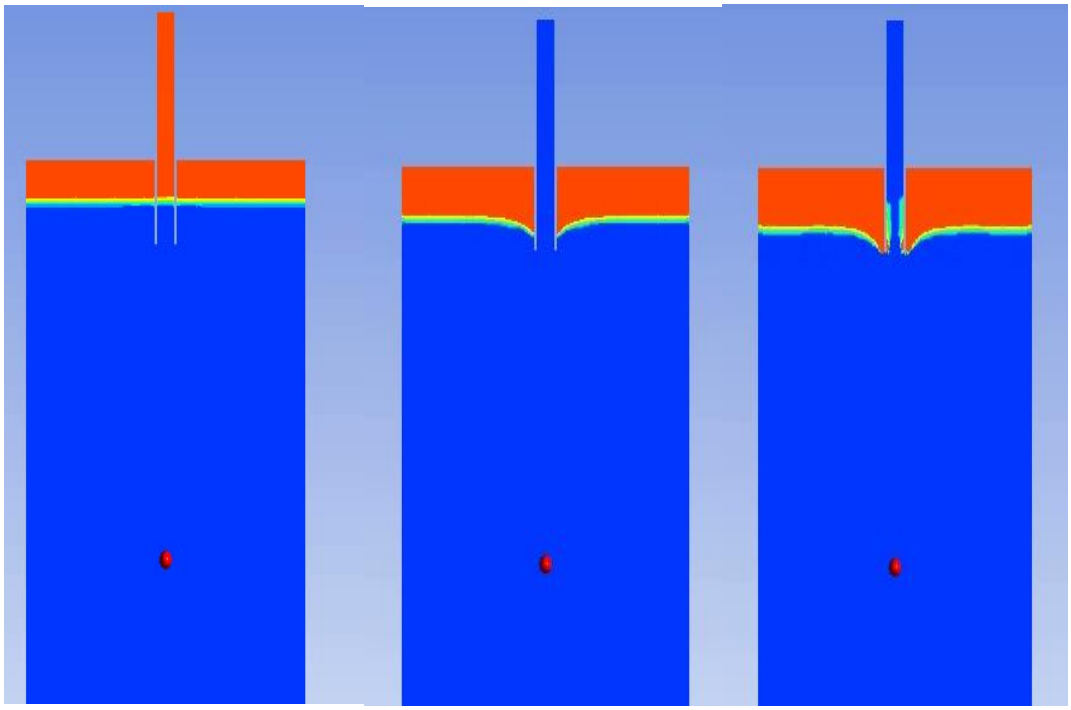


Figure 31: Simulated steps of the occurrence of oil entrainment at the 90º siphon obtained from Ansys.

4.2 Vortex Formation and Velocity Vector in the Simulation

4.2.1 Vortex Formation

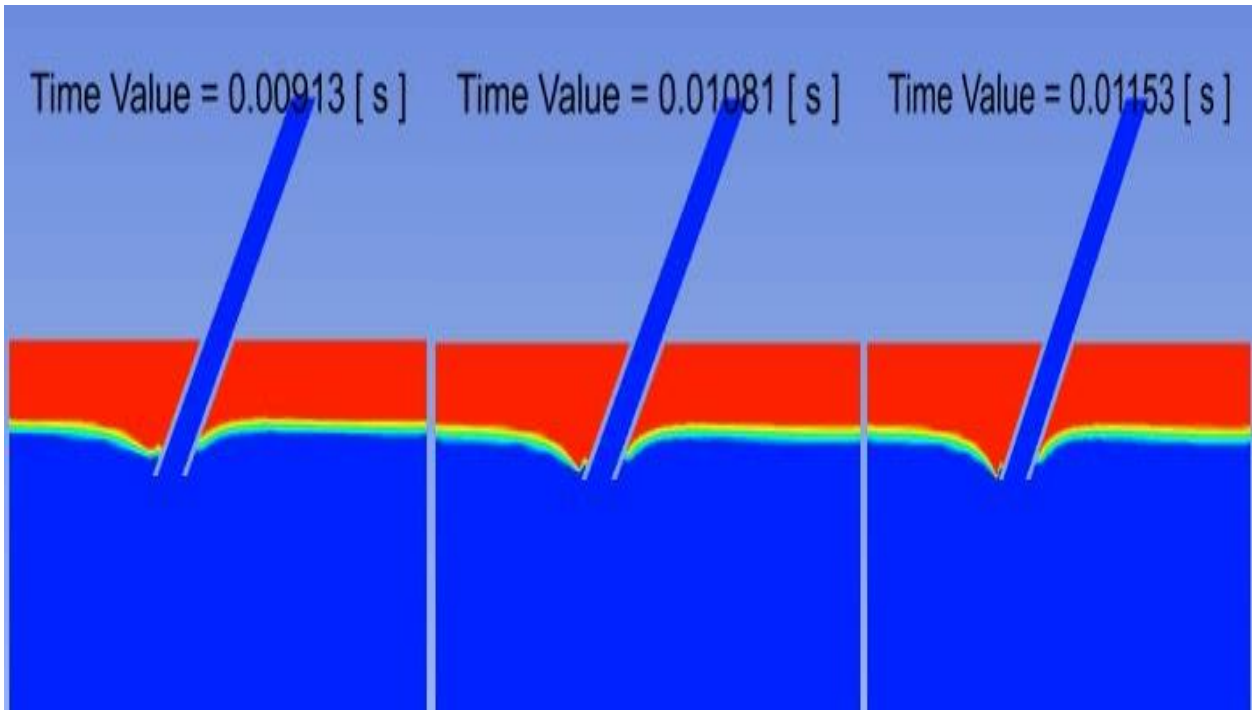


Figure 32: Stages of vortex formation at 60º siphon obtained from Ansys.

In this study, the vortex was only observed on the left side of the 60º inclined siphon but no sign of vortex was observed in 75º inclined and 90º siphon. The vortex formation is shown in **Figure 32**, the formation appears clearly as the submergence depth decrease before the oil is entrained through the vortex as a result of the interaction of water and oil at its interface. These two fluids at the interface have different densities with oil having low density than water. According to Hasan and Hayder (2021), the vertical siphon is the best for avoiding air-entrained vortices, followed by the horizontal siphon and then 22.5º inclined, with 45º being the worst.

4.2.2 Velocity Vector

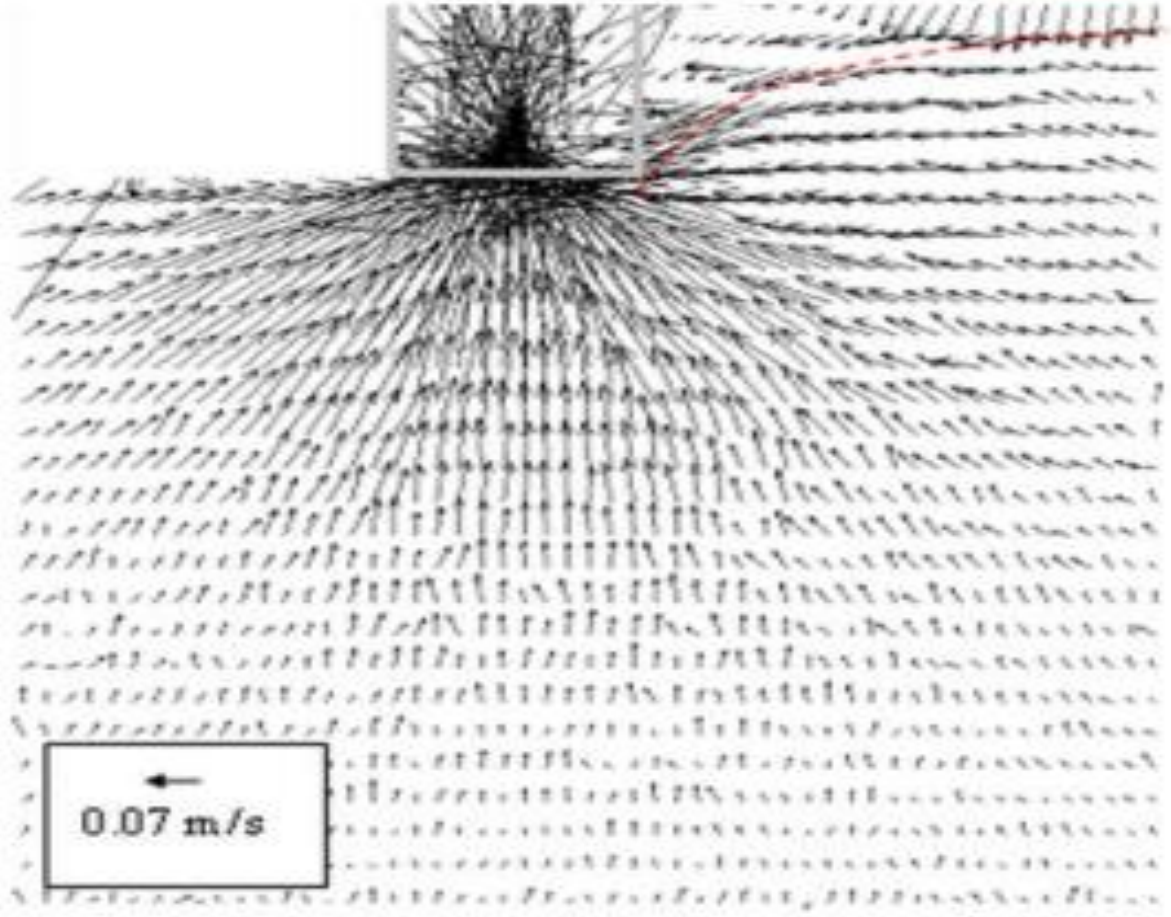


Figure 33: Velocity vector on primary orientation siphon obtained from experimental data (Hartenberg & O'Hern, 2011).

Velocity vectors are made up of two words: velocity + vectors. Let's define these two terms: We define velocity as the rate at which displacement changes. Vectors are physical quantities that have both a direction and a magnitude. Vectors are represented graphically by a line with an arrowhead on it. In this case, the length of the line drawn over the physical quantity represents the magnitude of the vector, and the arrow indicates the vector's direction. The velocity is the magnitude and direction of a speed. As a result, it is a vector quantity. So, a velocity vector represents the rate at which an object's position changes. The magnitude of a velocity vector indicates an object's speed, while the vector direction indicates its direction.

The Red dashed line in **Figure 33** represents the liquid-liquid interface and the liquid-liquid interface has been drawn down and into the siphon inlet.

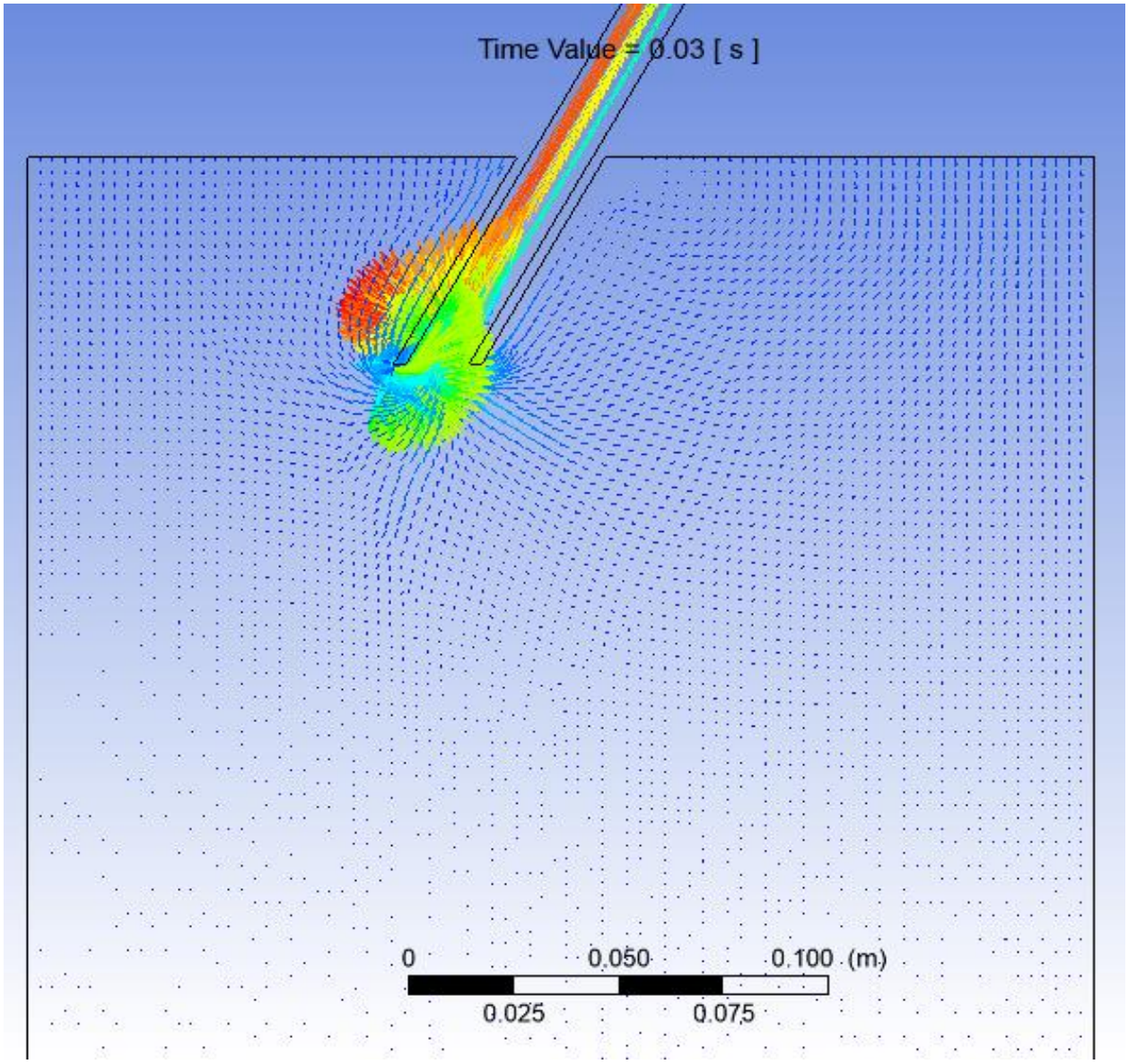


Figure 34: Velocity vector at the 60º inclined siphon obtained from the simulation.

Simulated velocity vector in **Figure 36** and experimental velocity vectors in **Figure 33** show a similar flow pattern, this is attributed to identical siphon angle. However, there is one discrepancy between **Figure 36** and **Figure 33**. **Figure 33** does not show the velocity vectors on the left side of the siphon. According to Hartenberg & O'Hern (2011), this is due to the siphon obstructing the light sheet.

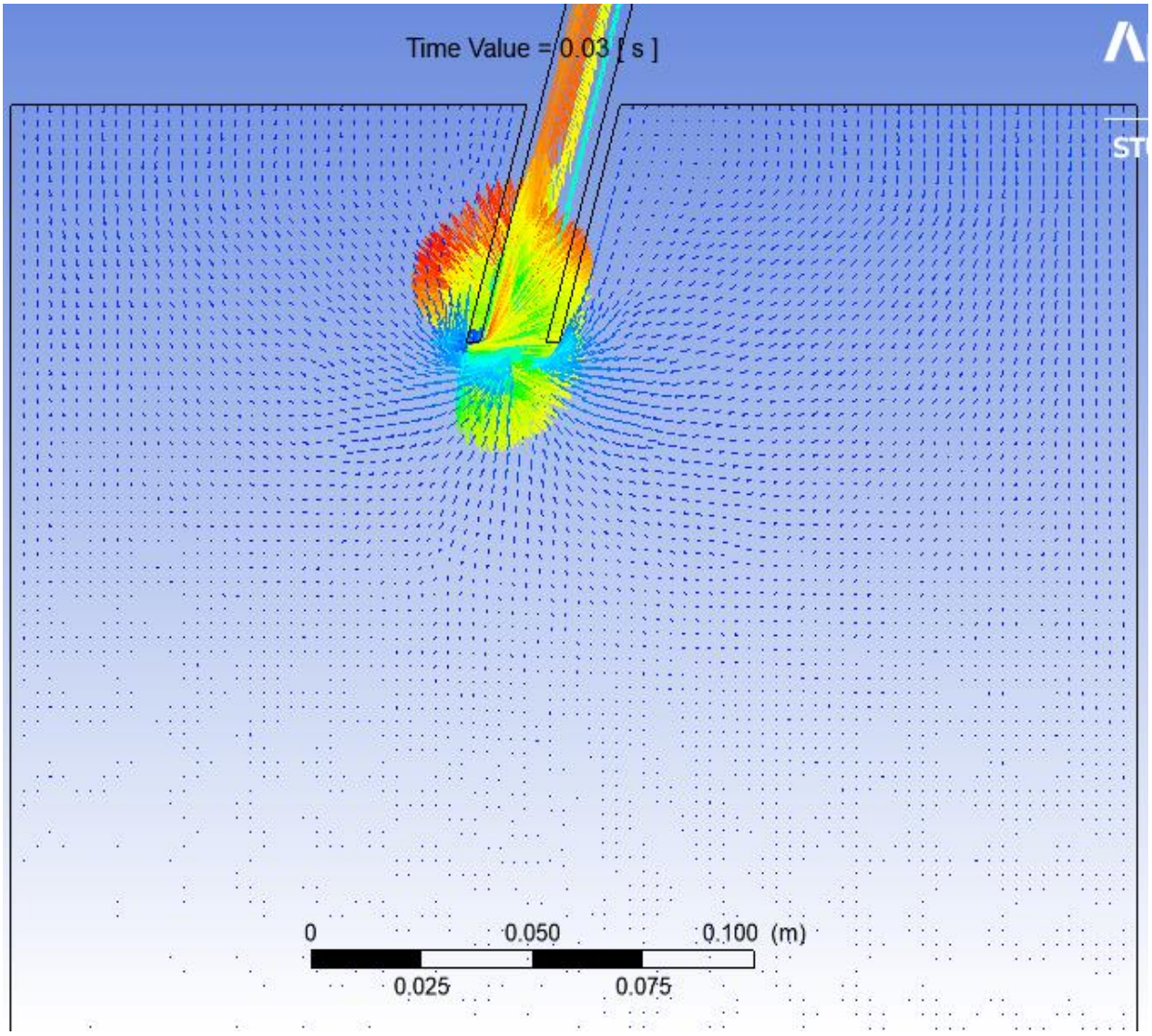


Figure 35: Velocity vector at the 75º inclined siphon obtained from the simulation.

Velocity vector fields on the left-hand side of **Figure 34** appear to be more curved near the inlet compared to **Figures 33**, **35** and **36**. The curved velocity vectors improve with increasing the leaning angle of the siphon. The velocity vectors in **Figures 33**, **34**, **35** and **36** were denser near the siphon inlet showing the region in which inertial forces are responsible for the transition to oil entrainment. To be clearer, beneath the siphon's inlet looks to be the most powerful flow which means as get further away from the siphon's inlet, the magnitude of the vectors decreases and this is shown in **Figures 33**, **34**, **35** and **36**. The length of the line drawn over-represents the magnitude of the vector.

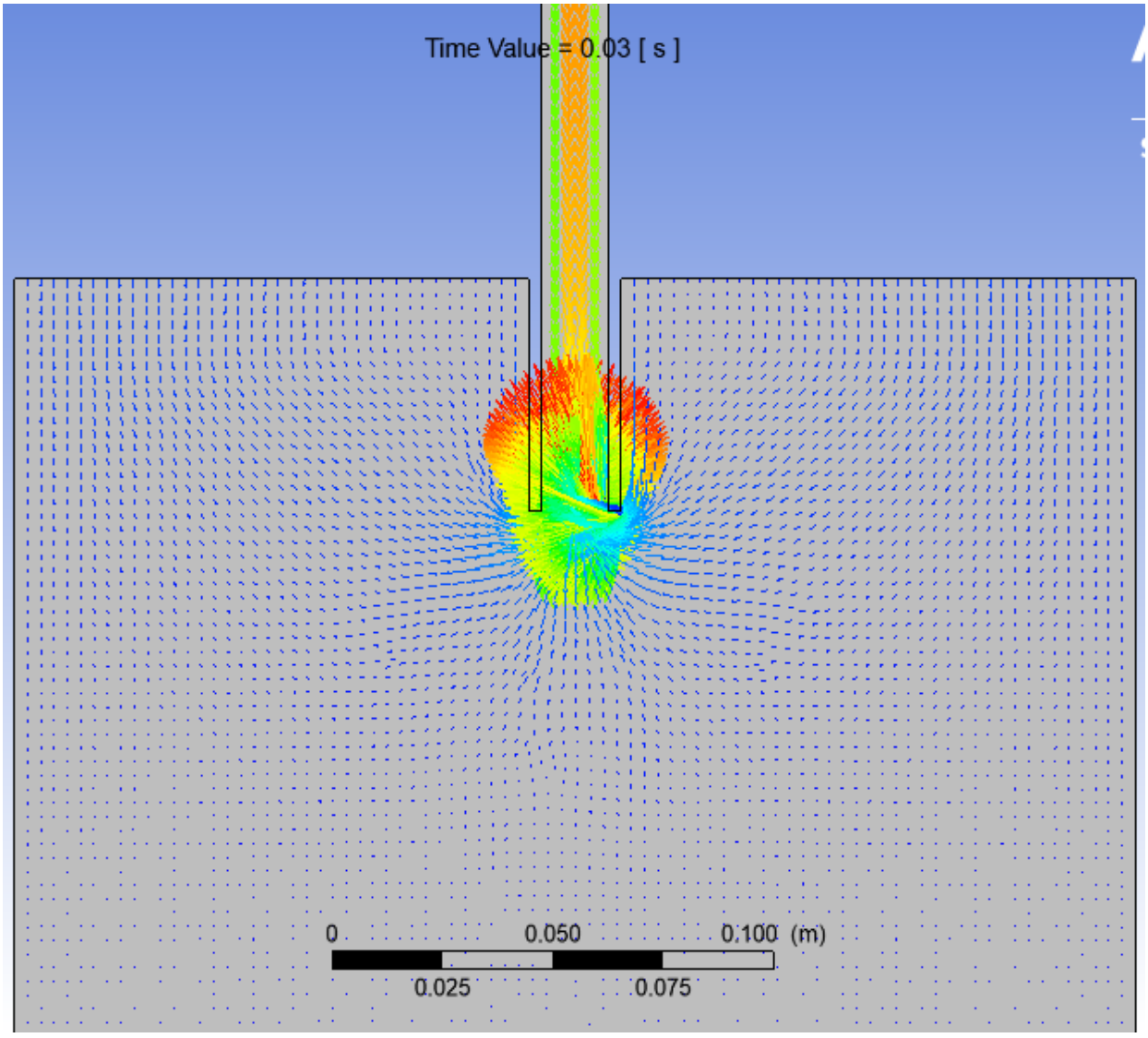


Figure 36: Velocity vector at the 90º siphon obtained from the simulation.

4.3 The effect of Pressure and Velocity

Graphs in **Figures 37**, **38**, **39** and **40** were plotted along lines shown in **APPENDIX A**. To be specific, plots in **Figures 37** and **39** were plotted along horizontal below the inlet as shown in **APPENDIX A**. Plots in **Figures 38** and **40** were plotted along symmetric lines to the siphon as shown in **APPENDIX A**.

Bernoulli's equation describes the relationship between pressure and velocity for any incompressible, non-viscous fluid, stating that increases in fluid speed result in low pressure, which entrains one fluid into another. The relationship between pressure and velocity is inverse. When pressure rises, velocity falls to maintain the algebraic total of potential energy, kinetic

energy, and pressure. Similarly, as velocity rises, the pressure falls to maintain the total potential energy, kinetic energy, and pressure (Darby & Chhabra, 2001; Munson *et al*., 2013).

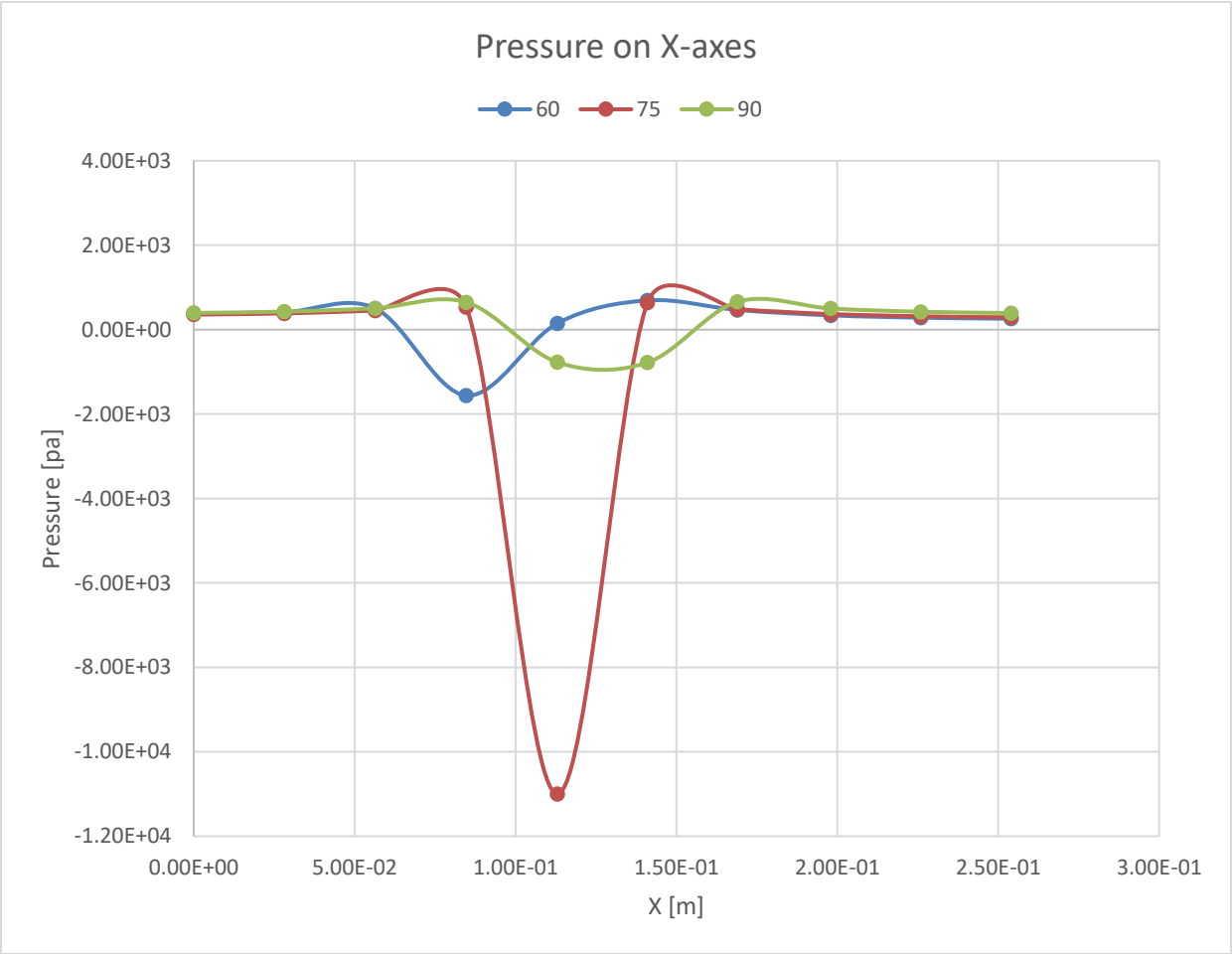


Figure 37: Variation of pressure along a horizontal line below the inlet.

Plots in **Figure 37** were plotted along horizontal below the inlet as shown in **APPENDIX A**. These plots show the pressure decrease as fluid approaches both sides of the siphon's inlet. 60º and 75º plots in **Figure 37** show that pressure on both sides of the siphon is ununiform but 75º is much better than 60º. The 90º shows more uniform pressure as fluid approaches the inlet, meaning fluid enter both sides of the siphon at the same time. The pressure is higher far away from the inlet and decreases as approaches the inlet. 60º and 75º inclined reach the minimum pressure of -1560 Pa and -11000 Pa while 90º reached the minimum pressure of -778 Pa.

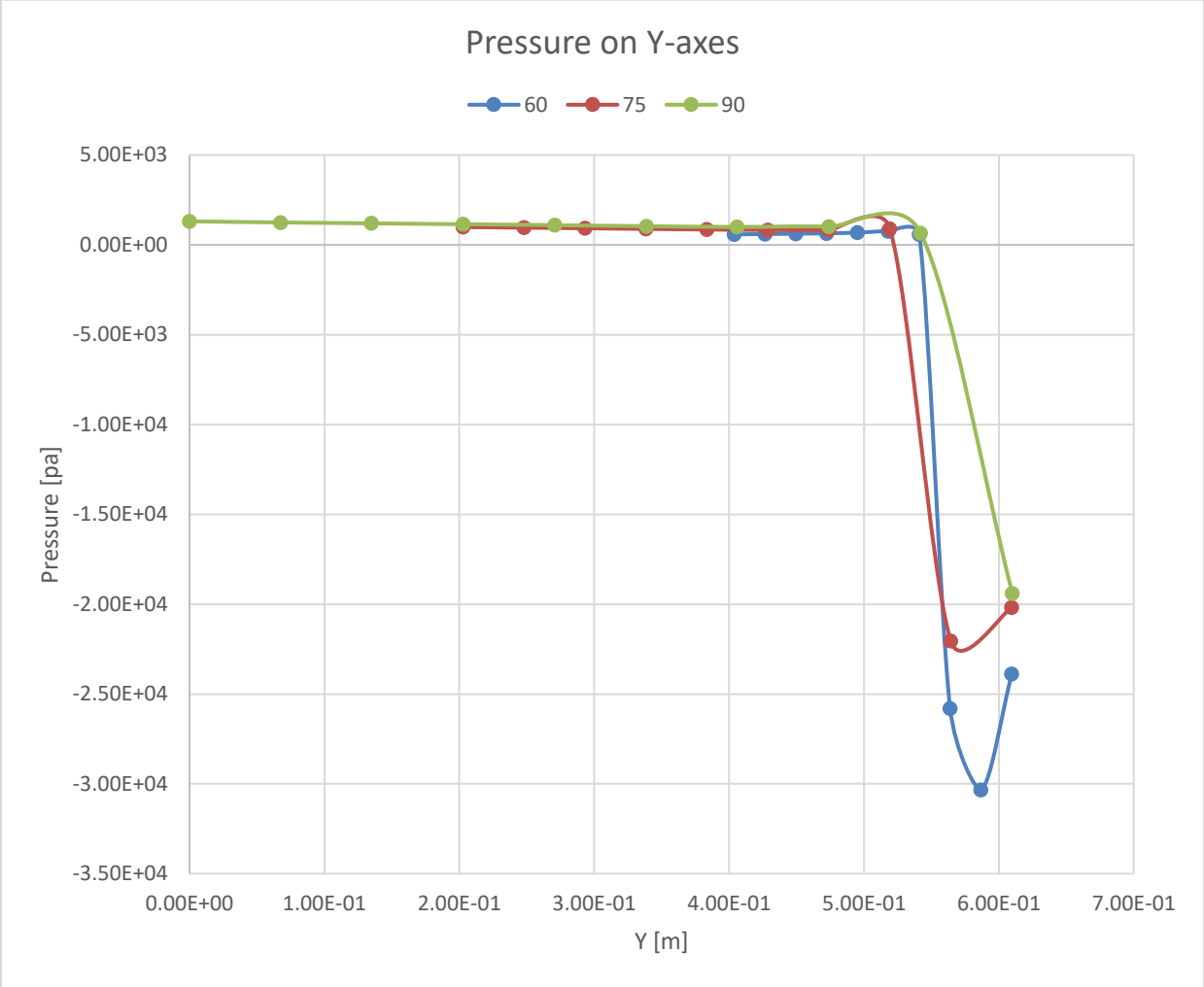


Figure 38: Variation of pressure along the symmetrical line to the siphon.

Plots in **Figure 38** were plotted along symmetric lines to the siphon as shown in **APPENDIX A**. **Figure 38** shows the same trend of high pressure far away from the inlet and decreasing as approaches the inlet. 60^{o} and 75^{o} inclined reach the minimum pressure of -30500 Pa and -22100 Pa respectively, as fluid flow further in the siphon pressure start to pick up, while 90^{o} incline reached the minimum pressure -19400 Pa and did not show any pressure increase at the same height with 60^{o} and 75^{o} incline siphons. This pressure change is solely caused by the fluid's elevation change as it flows uphill. In this investigation, during selective withdrawal, the decrease in pressure due to velocity increases creates a vacuum on the inlet.

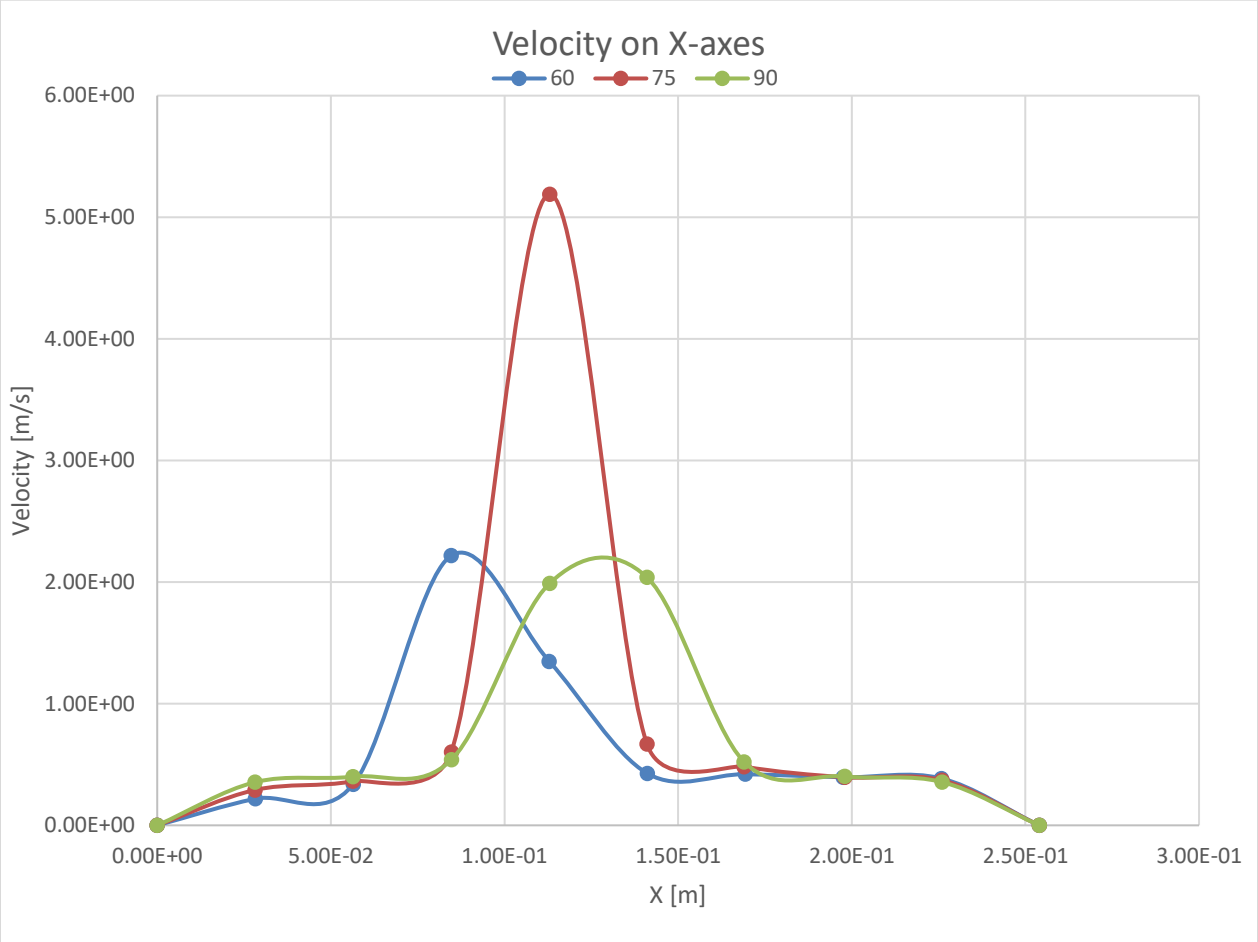


Figure 39: Variation of velocity along a horizontal line below the inlet.

Plots in **Figure 39** were plotted along horizontal below the inlet as shown in **APPENDIX A.** These plots show the velocity increase as fluid approaches both sides of the siphon's inlet. 60º to 75º show that velocities on both sides of the siphon are ununiform but 75º is much better than 60º. 90º shows uniform velocity as fluid approaching the inlet meaning fluid enter both sides of the siphon at the same time. This is the evidence that as the leaning angle increased from 60º to 75º and then 90º, improves uniformity. 75º inclined siphon archived the highest velocity of 5.19 m/s at the inlet followed by 60º inclined with the velocity of 2.22 m/s and lastly the 90º incline with the velocity of 2.04 m/s.

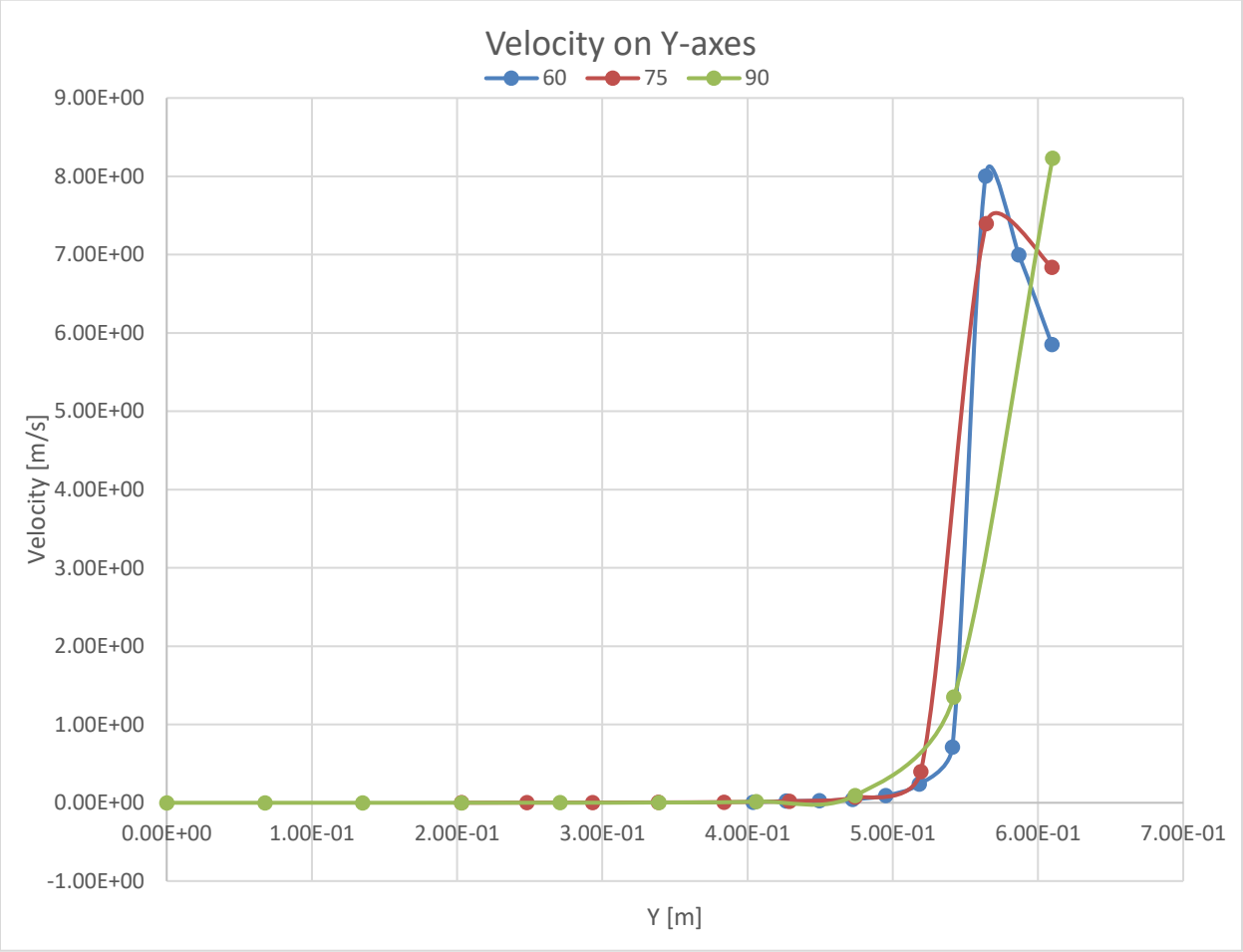


Figure 40: Variation of velocity along the symmetrical line to the siphon.

Plots in **Figure 40** were plotted along symmetric lines to the siphon as shown in **APPENDIX A**. These show the same trend of low velocity far away from the inlet and increasing as approaches the inlet. 60^{o} and 75^{o} inclined reach the maximum velocity 8.00 m/s and 7.39 m/s respectively as fluid flow further in the siphon before dropping, while 90^{o} reached the velocity of 8.23 m/s and did not show any velocity drop at the same height. This velocity change is solely caused by the fluid's elevation change as it flows uphill.

4.4 Calculated Dimensionless Numbers

Dimensionless numbers, in general, refer to physical parameters that have no units of measurement. These numbers are frequently used by process engineers in calculations. Dimensionless numbers remain the same regardless of whether metric or other units are used in the equations as long as consistent units are used (Salih, 2017).

The velocities in **Table 2** were obtained along horizontal lines below the inlet as shown in **Figures 38**, **39** and **40** at **APPENDIX A**. Dimensionless numbers in **Table 2** were calculated at **APPENDIX C.**

Table 2: Dimensionless Numbers

Leaning Angle (^{0})	*Velocity (m/s)*	S_c(cm)	Fr_d	Re_d	We_d
60	2.22	1.10	20	$3.32*10^4$	$1.352*10^3$
75	5.19	1.62	47	$7.77*10^4$	$1.091*10^4$
90	2.04	1.02	19	$3.05*10^4$	$1.059*10^3$

Dimensionless numbers, also known as non-dimensional numbers, are useful in fluid mechanics for determining the flow characteristics of a fluid. If there is any mass in motion, there is always an inertia force. Dividing this inertia force by other forces such as viscous force, gravity force, surface tension, elastic force, or pressure force yields dimensionless numbers. The Reynolds number, Froude number, and Weber number are dimensionless numbers used in the current investigation (Salih,2017).

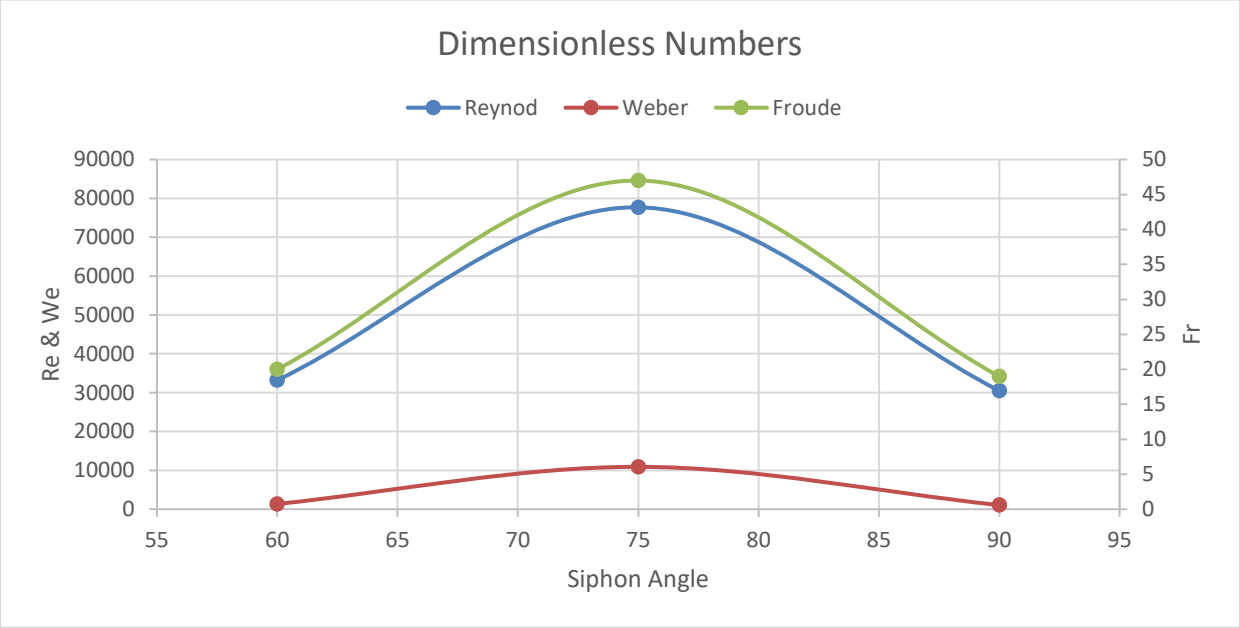


Figure 41: Dimensionless Numbers on the siphon angle

4.4.1 Reynolds Number

Reynolds number is a dimensionless number that gives a measure of the ratio of inertial forces to viscous forces and can be used to determine three classes of flow regime (Emerson, 2015; Salih, 2017). Reynolds number is proportional to inertia forces. A high Reynolds number means strong inertia forces and according to Hartenberg & O'Hern's (2011), these forces are responsible cause for oil entrainment. Reynolds number (diameter based) is shown in **Equation (16)**.

$$Re_d = \frac{\rho_1 v d}{\mu_1} \quad (16)$$

ρ_1 is a density of water, v is a velocity, d is the diameter of the siphon and μ_1 is a viscosity of water (Hartenberg & O'Hern, 2011).

In the experimental investigation, the Reynolds numbers on 1.57cm diameter siphon with a liquid pairing of silicon oil (5 cSt and 918kg/m3) and water ranged from ~1.7×10^4 to ~5.3×10^4. These Reynolds numbers were measured at the inlet of the siphon. Any flow with a Reynolds number greater than 4000 is considered turbulent, so the flows in these simulations were turbulent as shown in **Figure 41**. Because the geometry of 90° more closely resembles the primary orientation outlined in the experimental investigation, the Reynolds number on 90° was within the Reynolds number of the primary orientation.

4.4.2 Froude Number

Froude's number is a dimensionless number expressed as the ratio of the square root of the inertia force to the square root of gravity force (Hartenberg & O'Hern, 2011; Sequeiros, 2012; Salih, 2017). Froude number is proportional to inertia forces. A high Froude number means strong inertia forces. According to Hartenberg & O'Hern's (2011), these forces are responsible cause for oil entrainment. Froude number (diameter based) is shown in **Equation (17)**.

$$Fr_d = \frac{v}{\sqrt{g' d}} \quad (17)$$

$$g' = \frac{g(\rho_1 - \rho_2)}{\rho_1} \quad (18)$$

g' is a reduced gravitational constant, g is a reduced gravitational constant ρ_1 is a density of water, ρ_2 is a density of silicon oil, v is a velocity, d is a diameter of the siphon.

In the experimental investigation, Froude numbers on 1.57cm diameter pipe with a liquid pairing of silicon oil (5 cSt and 918kg/m3) and water ranged from ~9 to ~60. In this simulation, the Froude numbers at 60°, 75°, and 90° as shown in **Figure 41 and Table 2**, were within the range of the experimental investigation. The average critical Froude number was nearly 16 for the primary

withdrawal siphon orientation in the prototype and it is near to 19 of the 90^{o} siphon in the model. This is because the geometry of the model closely resembled the prototype.

4.4.3 Weber Number

Weber number is a dimensionless number expressed as the square root ratio of the inertia force to the force of surface tension. Weber number is proportional to inertia forces (Salih, 2017). High Weber number means strong inertia forces. These forces are responsible cause for oil entrainment. Weber number (diameter based) is shown in **Equation (19)** (Hartenberg & O'Hern, 2011; Salih, 2017).

$$We = \frac{sv^2\rho_1}{\gamma} \quad (19)$$

S is a submergence depth, γ is an interfacial tension.

In the experimental investigation, the Weber numbers on 1.57cm diameter pipe with a liquid pairing of silicon oil (5 cSt and 918kg/m3) and water ranged from ~90 to ~8000. In this simulation, the Weber numbers at 60^{o}, 75^{o}, and 90^{o} as shown in **Figure 41 and Table 2**, were within the range investigated in the experimental analysis.

Critical submergence refers to the vertical distance between the inlet of a siphon and the interface when the interface starts to be drawn into the siphon from the upper layer elevation. When the critical submergence is low, it prevents early entrainment, which means that selective withdrawal is optimal. The critical submergence of 60^{o}, 75^{o} and 90^{o} are 1.10, 1.62 and 1.02 cm respectively. The decrease in pressure brought on by the velocity pulls the interface downward and reduces submergence depth, causing interface to distort.

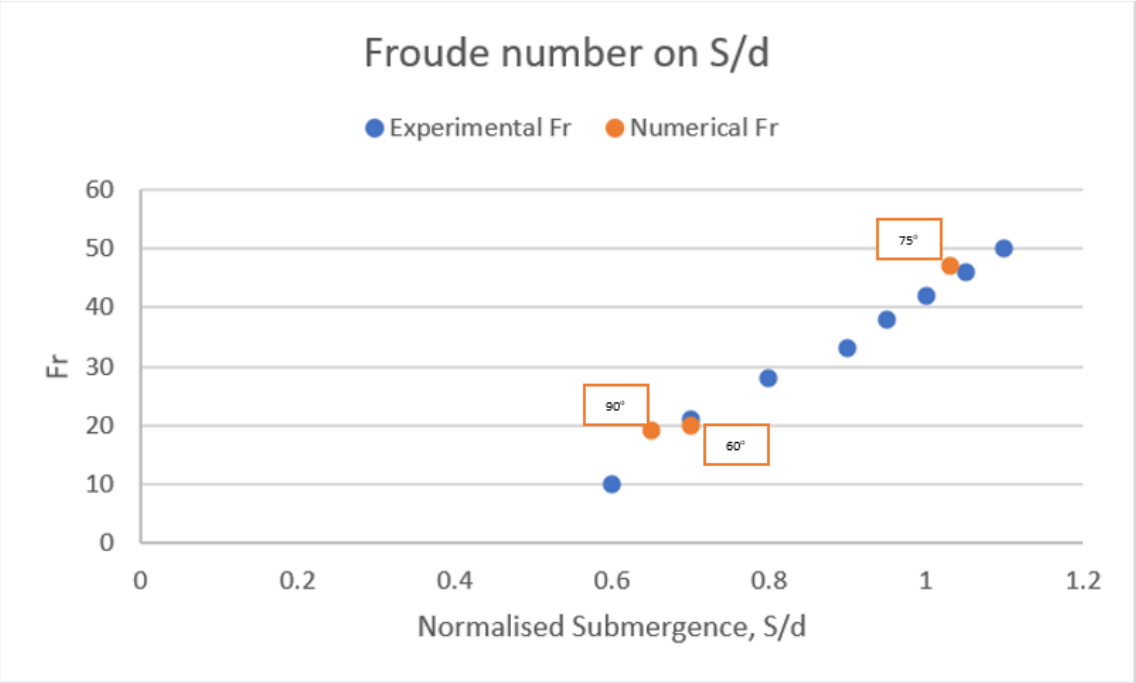


Figure 42: Froude & Weber number as a function of normalised submergence.

The results from the CFD model were validated with the data obtained from Experimental Investigation of Selective Withdrawal and Light Layer Entrainment of Stratified Immiscible Liquids. **Figure 42** illustrates the relationship between Froude number and normalized submergence depth, and compares the experimental values of primary orientation siphon with the simulated values of 60°, 75° and 90° siphon. It is also evident that the Froude number is an important parameter that affects the S_c in the selective withdrawal. Froude number is proportional to inertia forces. A high Froude number means strong inertia forces. As the inlet Froude number increases, critical submergence also increases and eventually entrain oil into the inlet from higher depth. The inertia of oil flow is the reason behind the decrease in S_c with the increase of Froude number, while the buoyancy is likely the primary source of restoring force that prevents the transition to light layer entrainment. As the Froude number increases, the inertia of oil flow also increases and overcomes the buoyance force which initiate the transition of the interface into the inlet of the siphon. The data presented in **Figure 42** shows that the 75° siphon was more prone to oil entrainment at high submergence depth and high Froude number when compared to the 60° and 90° siphons. The results show that the Froude number and submergence depth for the 60° and 90° siphons were almost similar.

CHAPTER 5: CONCLUSION AND RECOMMENDATION

5.1 Conclusion

The main objective of this research project is to investigate numerically the entrainment of crude oil during the selective withdrawal of brine. Silicone oil and water will be used as simulated fluids to represent crude oil and brine respectively.

This paper presents numerical simulations of selective withdrawal to supplement the experimental investigation. The simulations were carried out to investigate what causes the unintended withdrawal of crude oil during the selective withdrawal of brine from the salt cavern. To simulate flow on three inclined siphons, a multiphase 2-dimensional model based on the VOF model was used. Both the experiment and the numerical model revealed that the velocity of the fluid increases with decreasing pressure directly beneath the centerline of the siphon inlet, which reduces the siphon's submergence depth and causes the liquid-liquid interface to deform. There is a direct relationship between the flow rate and velocity of the flow of the liquid. When there is an increase in the flow rate of the flow also the velocity increases and the pressure is inverse to the velocity. As the flow and velocity increase while pressure decreases, the interface drops until the entrainment of oil occurs. 75^{o} inclined siphon was found to have the highest dimensionless numbers (Re_d, Fr_d and We_d) followed by the 60^{o} inclined siphon while 90^{o} siphon was the lowest. The transition from selective withdrawal to light layer entrainment was dependent upon the inclined angle of the siphon. The results showed that, for avoiding oil entrainment, 90^{o} siphon is better followed by 60^{o} inclined siphon, whereas the 75^{o} inclined siphon was the worse. The simulation is in agreement with the experimental analysis investigated by Hartenberg and O'Hern (2011).

5.2 Recommendation

Vibration does occur when fluid flows through pipes. The effect of siphon vibration was overlooked in the current study by simulating with no-slip boundary conditions of a stationary wall. The speed of the fluid on the wall is o m/s in no-slip boundary conditions and nonzero in slip boundary conditions. The effects of slip boundary conditions on the liquid-liquid interface are worth researching. The effect of the second-order element, polygon and tetrahedral elements were overlooked in the current investigation, the use of these elements is worth researching.

APPENDIX A: SYMMETRICAL LINES ALONG THE SIPHON AND HORIZONTAL LINES BELOW THE SIPHON'S INLET.

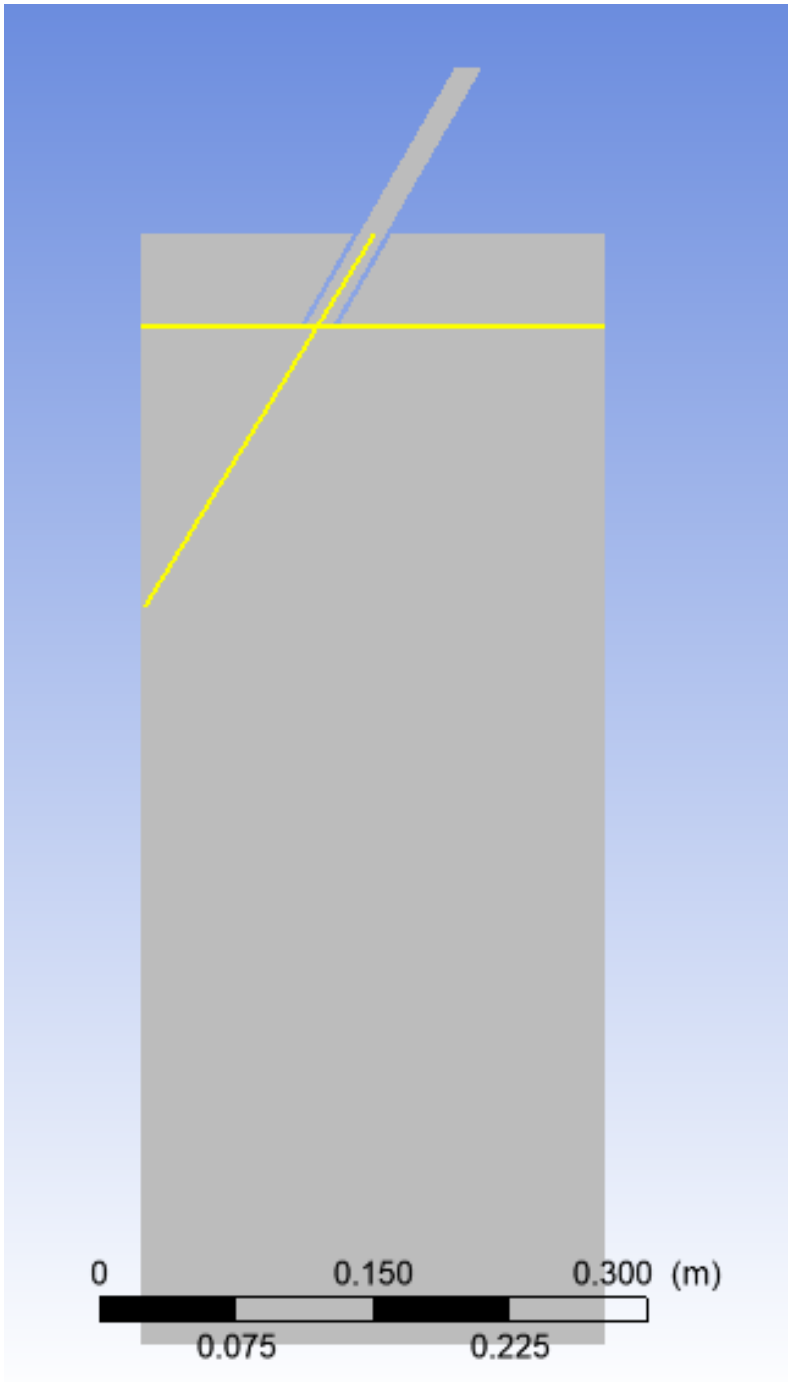


Figure 43: At a 60º inclined siphon, Symmetrical line along the siphon and horizontal line below the inlet.

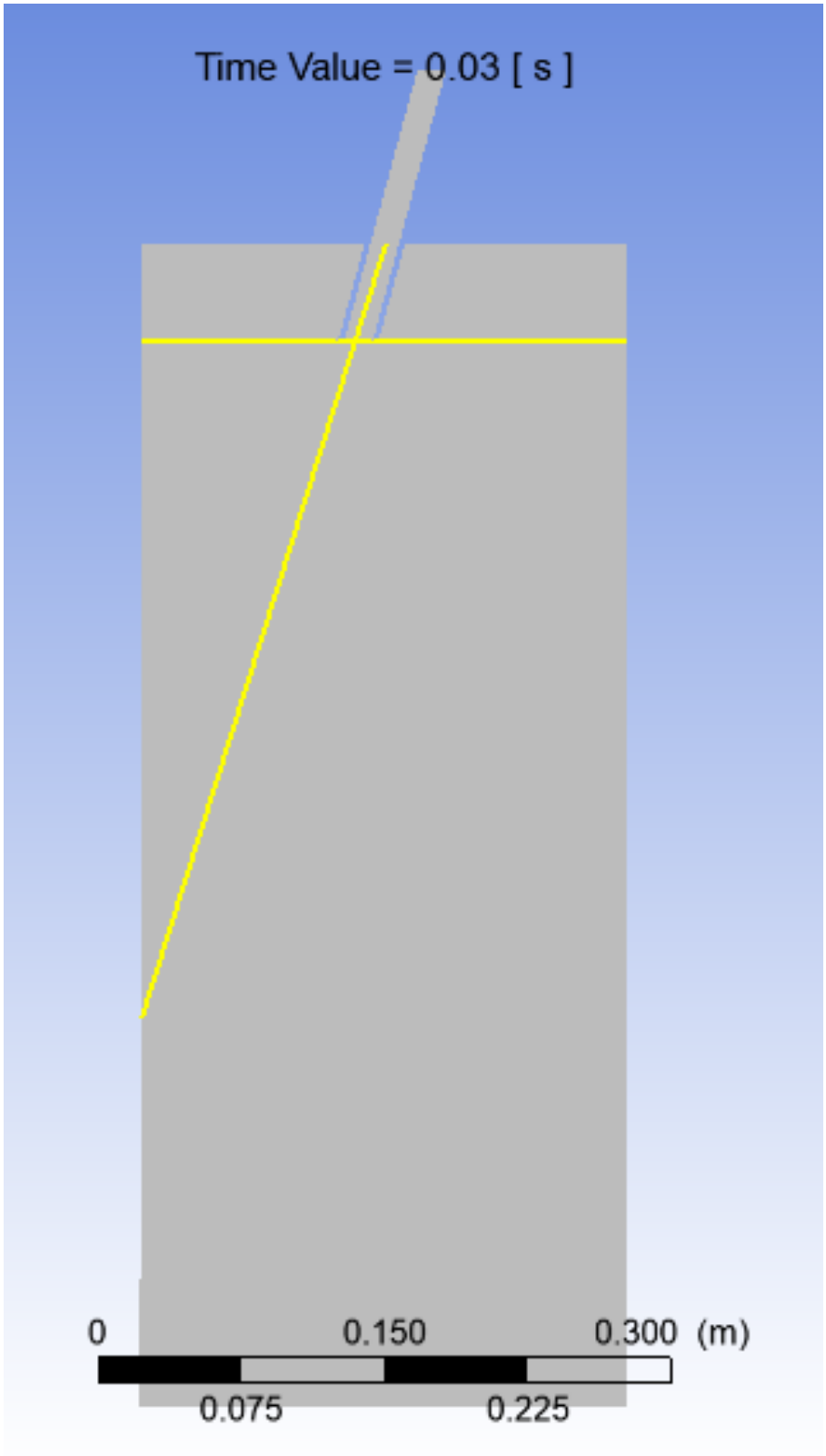


Figure 44: At a 75º inclined siphon, Symmetrical line along the siphon and horizontal line below the inlet.

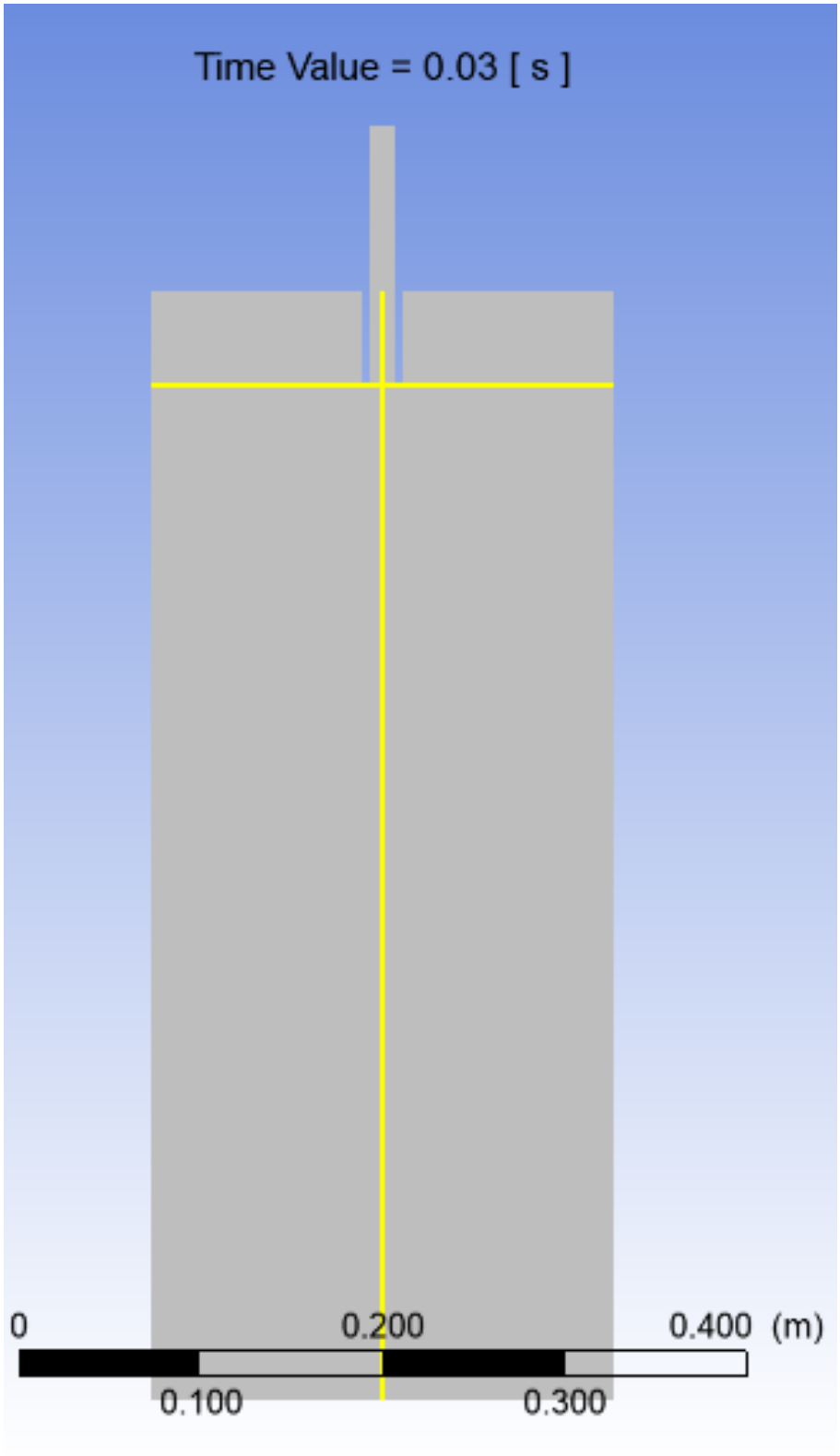


Figure 45: At a 90º inclined siphon, Symmetrical line along the siphon and horizontal line below the inlet.

APPENDIX B: SUMMARY STEPS OF FLOW SOLVER IN FLUENT

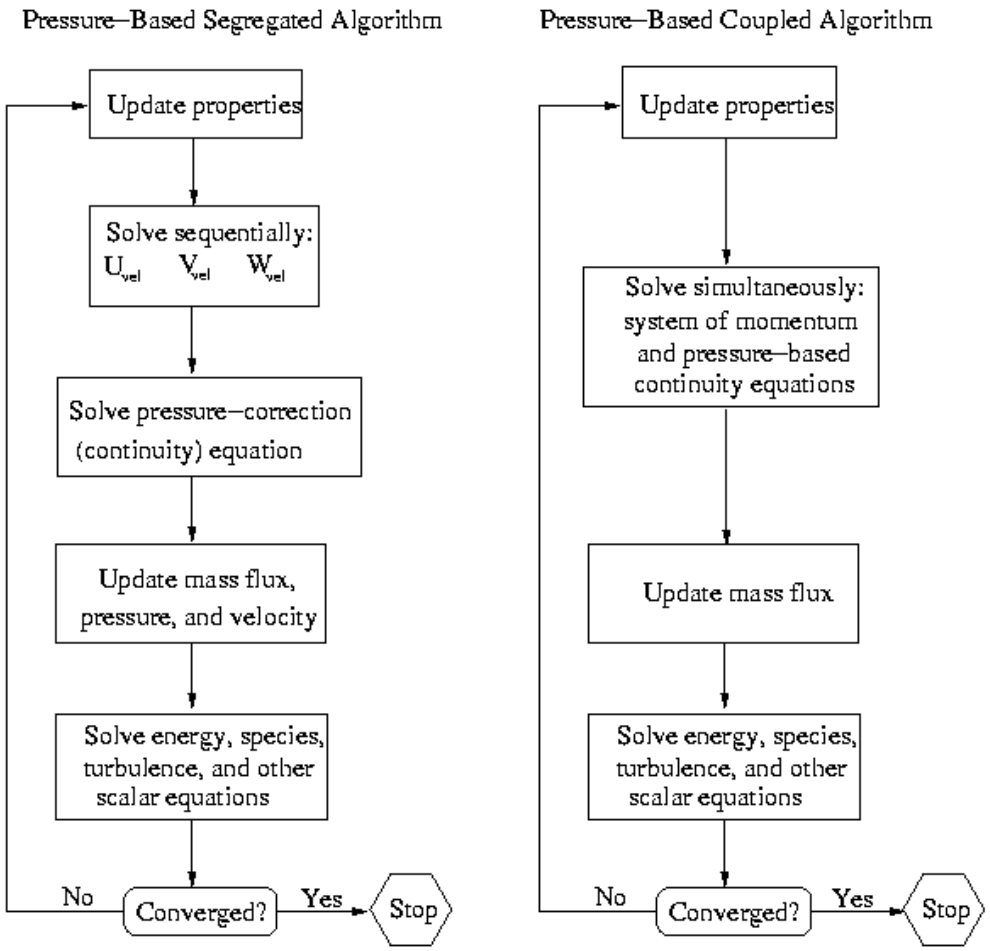


Figure 46: Summary steps of Pressure-Based Solution Methods (Ansys Inc, 2009).

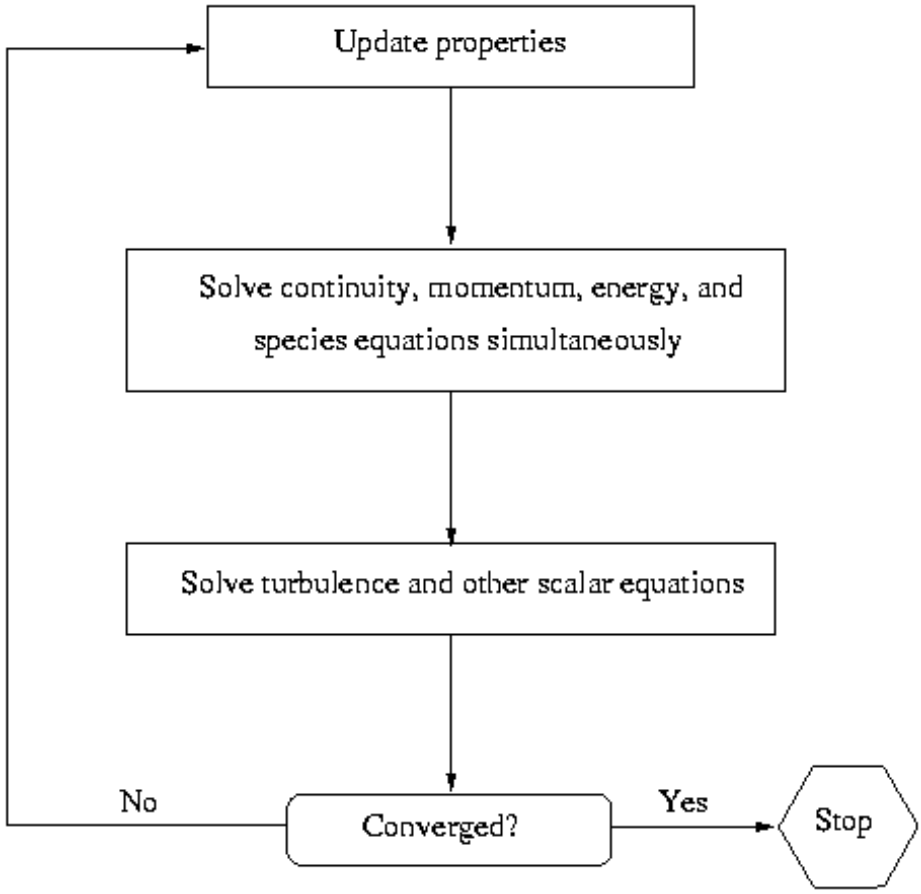


Figure 47: Summary steps of Density-Based Solution Method (Ansys Inc, 2009).

APPENDIX B: CALCULATIONS OF THE DIMENSIONLESS NUMBERS

Table 3: Flow velocity at the siphon's inlet of the simulations

Leaning Angle (^{0})	*Flow Velocity (m/s)*
60	2.22
75	5.19
90	2.04

Table 4: Properties of fluids used in the simulation.

Properties	*Silicon oil*	*water*
Density (kg/m3)	918	998
Viscosity (kg/ms)	0.005	0.001
Gravity (m/s2)	9.81	
Interfacial Tension (N/m)	0.04	

Table 5: Testing tank geometry values.

Geometry	*Values*
Silicon oil (cm)	2.54
Submergence Depth (cm)	2.54
Siphon Diameter (cm)	1.5
Tank Hight (cm)	60.96
Tank width (cm)	25.4

Reynolds Number Calculations

$$Re_d = \frac{\rho_1 v d}{\mu_1} \qquad (16)$$

ρ_1 is a density of water, v is a velocity, d is the diameter of the siphon and μ_1 is a viscosity of water

60º Siphon

$$Re_d = \frac{998 * 2.22 * 0.015}{0.001}$$

$= \underline{3.32*10^4}$

75º Siphon

$$Re_d = \frac{998 * 5.19 * 0.015}{0.001}$$

$= \underline{7.77*10^4}$

90º Siphon

$$Re_d = \frac{998 * 2.04 * 0.015}{0.001}$$

$= \underline{3.05*10^4}$

Froude Number Calculations

$$Fr_d = \frac{v}{\sqrt{g'd}} \quad (17)$$

$$g' = \frac{g(\rho_1 - \rho_2)}{\rho_1} \quad (18)$$

g' is a reduced gravitational constant, g is a reduced gravitational constant ρ_1 is a density of water, ρ_2 is a density of silicon oil, v is a velocity, d is a diameter of the siphon.

$$g' = \frac{9.81(998 - 918)}{998}$$

$= \underline{0.786 \text{ m/s}}$

60º Siphon

$$Fr_d = \frac{2.22}{\sqrt{0.786 * 0.015}}$$

$= \underline{20}$

75º Siphon

$$Fr_d = \frac{5.19}{\sqrt{0.786 * 0.015}}$$

$= \underline{47}$

90º Siphon

$$Fr_d = \frac{2.04}{\sqrt{0.786 * 0.015}}$$

$= \underline{19}$

Weber Number Calculations

$$We = \frac{sv^2\rho_1}{\gamma} \quad (19)$$

S is a submergence depth, γ is an interfacial tension, ρ_1 is a density of water, *v* is a velocity

60º Siphon

$$We = \frac{0.0110 * (2.22)^2 * 998}{0.04}$$

$= \underline{1.352*10^3}$

75º Siphon

$$We = \frac{0.0162 * (5.19)^2 * 998}{0.04}$$

$= \underline{1.0906*10^4}$

90º Siphon

$$We = \frac{0.0102 * (2.04)^2 * 998}{0.04}$$

$= \underline{1.059*10^3}$

REFERENCES

Abdulkadir, M., Hernandez-Perez, V., Lo, S., Lowndes, I. and Azzopardi, B., 2013. Comparison of Experimental and Computational Fluid Dynamics (CFD) Studies of Slug Flow in a Vertical 90° Bend. *The Journal of Computational Multiphase Flows*, 5(4), pp.265-281.

Abdulsalam, J., 2019, *Introduction to Petroleum and Offshore Operations*, CHMT5006A, lecture notes, University of Witwatersrand, delivered March 2019.

Abulnaga, B.E. and Rushdi, K., 2013. Froude numbers and hydraulic jumps of open channel slurry flows. *Transactions of the society for mining, metallurgy, and Exploration*, Vol. 334, pp. 535-543.

Ahmad, Z. and Hashid, M., 2020. Experimental and Numerical Study of Critical submergence for Dual intakes. In: *8th IAHR ISHS 2020*. Santiago, Chile: India Institute of Technology Roorkee, pp.1- 10.

Ajoko, T.J. and Ebughni, N.P., 2015. Multiphase flow simulation of oil and gas in vertical flow using CFXPRE and FLUENT. *International Journal of Scientific & Engineering Research*, 6(9), pp.741 - 749.

Albaali, G. and Farid, M.M., 2006. Fundamentals of Computational Fluid Dynamics. pp. 34 - 44.

Alfonsi, G., 2009. Reynolds-Averaged Navier–Stokes Equations for Turbulence Modeling. *Applied Mechanics Reviews*, 62(4).

Anderson, J.D. and Wendt, J.F., 2009. Governing Equations of Fluid Dynamics. *Springer-Verlag*, pp.15 - 51.

Ansys Inc, 2009. *Overview of Using the Solver: User Guide*. Release 12.0. Canonsburg, PA: Ansys Inc. https://www.afs.enea.it/project/neptunius/docs/fluent/html/ug/node776.htm

Ansys Inc, 2010. *Ansys Meshing: User Guide*. Release 13.0. Canonsburg, PA: Ansys Inc.

Ansys Inc, 2012. *DesignModeler: User Guide*. Release 14.5. Canonsburg, PA: Ansys Inc.

Ansys Inc, 2013. *Ansys Fluent: User Guide*. Release 15.0. Canonsburg, PA: Ansys Inc.

API, 2020. API standard 650. *American Petroleum Institute*, [online] third edition, pp.1–514. Available at: www.api.org.

Arthur, J.D., Alleman, N. & Andersen, K., 2016. A Historical Look at Underground Natural Gas Storage in America, image, AAP/Datapages, Vol. 17, no. 1, pp. 35 – 46.

ASTM Standard D4052, 2011, "Standard Test Method for Density, Relative Density, and API Gravity of Liquids by Digital Density Meter[1]" ASTM International, West Conshohocken, Pennsylvania, 2011, DOI: 10.1520/D4052-11, www.astm.org.

ASTM Standard D445, 2017a, "Standard Test Method for Kinematic Viscosity of Transparent and Opaque Liquid (and Calculation of Dynamic Viscosity" ASTM International, West Conshohocken, Pennsylvania, 2017, DOI: 10.1520/D445-17A, www.astm.org.

Atlas, R.M. (1975). Effects of Temperature and Crude Oil Composition on Petroleum Biodegradation. *Applied Microbiology*, 30(3), pp.396–403. https://doi.org/10.1128/am.30.3.396-403.1975.

Azin, R., Nasiri, A. and Entezari, J., 2008. Underground Gas Storage in a Partially Depleted Gas Reservoir. *Oil & Gas Science and Technology - Revue de l'IFP*, 63(6), pp.691-703.

Baker, R.C. (1990). Fluid flow measurement. *Flow Measurement and Instrumentation*, 1(4), pp.241–243.

Barca, F., Caporossi, T & Rizzo, S 2014, 'Silicone Oil: Different Physical Properties and Clinical Applications', *BioMed Research International*, pp. 1 – 7.

Barker, G.B., 2018. *The Engineer's Guide To Plant Layout And Piping Design For The Oil And Gas Industries*. Gulf Professional Publishing, pp.361 - 380.

Bérest, P. and Brouard, B., 2003. Safety of Salt Caverns Used for Underground Storage Blow Out; Mechanical Instability; Seepage; Cavern Abandonment. *Oil & Gas Science and Technology*, 58(3), pp.361-384.

Bérest, P., Brouard, B. and Durup, J.G., 2001. Tightness Tests in Salt-Cavern Wells. *Oil & Gas Science and Technology*, 56(5), pp.451–469. doi:https://doi.org/10.2516/ogst:2001037.

Berkenbusch, M.K., Cohen, I. and Zhang, W.W., 2008. Liquid interfaces in viscous straining flows: numerical studies of the selective withdrawal transition. *Journal of Fluid Mechanics*, 613, pp.171-203.

Bert, R., Manes, C. and Tiraferri, A. (2022). New Facility for Membrane Fouling Investigations under Customizable Hydrodynamics: Validation and Preliminary Experiments with Pulsating Cross-Flow. *Membranes*, 12(3), p.334.

Blanchette, F. & Zhang, W., 2009. Force Balance at the Transition from Selective Withdrawal to Viscous Entrainment. *Physical Review Letters*, 102(14), pp. 1 – 4.

Bonto, M., Eftekhari, A. and Nick, H., 2019. An overview of the oil-brine interfacial behavior and a new surface complexation model. *Scientific Reports*, 9(1), pp.1 - 16.

Bruno, M. and Dusseault, M., 2003. Geomechanical Analysis of Pressure Limits for Thin Bedded Salt Caverns. In: *Spring 2002 Meeting*. Banff, Alberta: Solution Mining Research Institute, pp.1 - 25.

Bruno, M., Dorfmann, L., Han, G., Lao, K. and Young, J., 2005. 3D Geomechanical Analysis of Multiple Caverns in Bedded Salt. In: *SMRI Fall 2005 Meeting*. Nancy, France: Solution Mining Research Institute, pp.1 - 25.

Çengel, Y.A. and Cimbala, J.M., 2014. *Fluid Mechanics: fundamentals and Applications*. 3rd ed. New York: McGraw-Hil, pp.347 - 419.

Chibwe, D., Akdogan, G., Aldrich, C. and Eric, R., 2011. CFD Modelling of Global Mixing Parameters in a Peirce-Smith Converter with Comparison to Physical Modelling. *Chemical Product and Process Modeling*, 6(1), pp. 1 – 28.

Chorin, A.J., 1968. Numerical solution of the Navier-Stokes equations. *Mathematics of Computation*, 22(104), pp.745-745. (Chorin, 1968).

Cohen, I., 2004. Scaling and transition structure dependence on the fluid viscosity ratio in the selective withdrawal transition. *Physical Review E*, 70(2).

Cohen, I. and Nagel, S., 2002. Scaling at the Selective Withdrawal Transition through a Tube Suspended above the Fluid Surface. *Physical Review Letters*, 88(7).

Comte-Bellot, G., 1976. Hot-Wire Anemometry. *Annual Review of Fluid Mechanics*, 8(1), pp.209-231.

CPA (2019). *Why You Need a Flow Conditioner for Oil and Liquid Hydrocarbon Flows*. [online] Canada Pipeline Accessories. Available at: https://www.flowconditioner.com/why-you-need-a-flow-conditioner-for-liquid-petroleum-and-oil/ [Accessed 11 May 2023].

Crotogino, F.R., 1995. SMRI Reference for External Well Mechanical Integrity Testing/Performance, Data Evaluation and Assessment. Summary of the Final Project Report, SMRI 95-0001.

Darby, R. and Chhabra, R.P., 2001. *Chemical Engineering Fluid Mechanics*. 2nd ed. New York, USA: Marcel Dekker, Inc., pp.149 - 266.

Day, M.A., 1990. The no-slip condition of fluid dynamics. *Erkenntnis*, 33(3), pp.285-296.

Eder A., Durst B., Jordan M. (2001) Laser-Doppler Velocimetry — Principle and Application to Turbulence Measurements. In: Mayinger F., Feldmann O. (eds) Optical Measurements. Heat and Mass Transfer. Springer, Berlin, Heidelberg. https://doi.org/10.1007/978-3-642-56443-7_8

EL-Samanody, M., Ghorab, A. and Noaman, A.S., 2017. design and study of floating roofs for oil storage tanks. *Mechanics and Mechanical Engineering*, 21(1), pp.117 - 136.

Emerson, 2015. *Theory of DP Flow*. Rosemount inc, pp.32 - 51. Available at: < https://pdf4pro.com/amp/view/theory-of-dp-flow-emerson-4ec532.html> [Accessed 25 October 2020].

Engel, R. and Baade, H.-J. (2015). Quantifying impacts on the measurement uncertainty in flow calibration arising from dynamic flow effects. *Flow Measurement and Instrumentation*, 44, pp.51–60.

Farrow, D.E. and Hocking, G.C., 2006. A numerical model for withdrawal from a two-layer fluid. *Journal of Fluid Mechanics*, 549(-1), pp.141 - 157.

Gazem, A., Rabeeh, M.D., Shahbaz, M.D., Laheb, M., Kumar, S. and Kanna, A.R., 2018. Surface and Interfacial Tension For Various Liquids. *International Refereed Journal of Engineering and Science (IRJES)*, 7(1), pp.64 - 66.

Geocaching, 2008. The Salt of the earth, image, viewed 26 June 2020. https://www.geocaching.com/seek/cache_details.aspx?guid=3dd5036e-efc7-4271-8bd1-0216ef07df31

Guerrero, E., Munoz, F. and Ratkovich, N., 2017. Comparison Between Eulerian and VOF Models for Two-Phase Flow Assessment in Vertical Pipes. *CT&F - Ciencia, Tecnología y Futuro*, Vol. 7. Pp. 73 – 84.

Guo, X., Hao, C. & Niu, S., 2020. Analysis of oil import Risk and Strategic Petroleum Reserve: The case of China. *Sustainability*, pp. 1 – 20.

Han, G., Bruno, M., Lao, K., Young, J. and Dorfmann, L., 2007. Gas Storage and Operations in Single-Bedded Salt Caverns: Stability Analyses. *SPE Production & Operations*, 22(03), pp.368-376.

Hartenberg, J.D. and O'Hern, T.J., 2011. Experimental investigation of selective withdrawal and light layer entrainment of stratified immiscible liquids. *International Mechanical Engineering Congress & Exposition*, pp.1 - 9.

Hasan, M.M.A and Hayder, A.A., 2021. Air entrained Vortex Occurrence at Sump for Inclined Multiple Intake Pipes using CFD. *Journal of Engineering Science and Technology*, pp.93 - 104.

Helmenstine, A.M., 2020. *Why Oil And Water Don't Mix*. [image] Available at: <http://thoughtco.com> [Accessed 20 September 2020].

Hendriana, D., 2020. *Oil and Gas Industry*. [online] Center for Computational Fluid Dynamics. Available at: <https://centerforcfd.com/oilgas.htm> [Accessed 21 June 2020].

Hirt, C.W. & Nichols, B.D., 1981. Volume of Fluid (VOF) method for the Dynamics of Free Boundaries. *Journal of Computational Physics*, pp. 201 – 225.

Hjelmeland, O.S. and Larrondo, L.E., (1986). Experimental Investigation of the Effects of Temperature, Pressure, and Crude Oil Composition on Interfacial Properties. *SPE Reservoir Engineering*, 1(04), pp.321–328.

Jafari, A., Hasani, M., Hosseini, M. and Gharibshahi, R., 2019. Application of CFD technique to simulate enhanced oil recovery processes: current status and future opportunities. *Petroleum Science*, 17(2), pp.434-456.

Johansson, K., 2011. *Numerical Simulation Of Fuel Filling With Volume Of Fluid*. Master of Science. Chalmers University of Technology. pp. 1 – 65.

Kabezya, K., Hara, T. and Paton, R., 2019. A review of primary aluminium tapping models, SN Applied Sciences. *Springer International Publishing*, 1(8), pp. 1–9.

Kline, S.J., 1969, Flow Visualization, National Committee for Fluid Mechanics Films, No. 21607, pp. 1 – 5.

Lane, A., 2019. Bereau of water/Geology and Well Technology Unit: Underground Hydrocarbon Storage (UHS), http://www.kdheks.gov/uhs/index.html

Ledzung, 2012. *Petroleum Storage Tanks Basic Training*. Slideshare Business, pp. 1 – 97.

Li, J. and Renardy, Y., 2000. Numerical Study of Flows of Two Immiscible Liquids at Low Reynolds Number. *SIAM Review*, 42(3), pp.417-439.

Louisiana Offshore Oil Port, 2016. *Salt Cavern*. [image] Available at: https://www.loopllc.com [Accessed 20 June 2020].

Lu, J., Zhang, W., Wang, D. and Wang, X., 2018. A New Device used in Selective Withdrawal from Reservoirs and its Effectiveness Verified in Computational Fluid Dynamics. *International Journal of Online Engineering (iJOE)*, 14(03), pp.142 – 151.

Lubin, B.T. and Springer, G.S., 1967. The formation of a dip on the surface of a liquid draining from a tank. *Journal of Fluid Mechanics*, 29(2), pp.385-390.

Majumdar, P., 2011. Computational Fluid Dynamics Analysis of Turbulent Flow. In: I. Minin, ed., *Computational Fluid Dynamics Technologies and Applications*. [online] InTech, pp.255 - 292. Available at: <http://www.intechopen.com/books/computational-fluid-dynamics-technologies-andapplications/computational-fluid-dynamics-analysis-of-turbulent-flow> [Accessed 11 November 2020].

Moghtaderi, B., 2003. Application Of Laser Doppler Velocimetry (ldv) To Study The Structure Of Gravity Currents Under Fire Conditions. *Fire Safety Science*, 7, pp.271-282.

Mohanty, S., Sigl, O., Krenn, F. and Höfer-Öllinger, G., 2013. Underground crude oil storage projects in India / Unterirdische Rohölkavernen in Indien. *Geomechanics and Tunnelling*, 6(5), pp.509-518.

Moreno, C., 2014. Determining Critical Submergence in Tanks by Means of Reynolds & Weber Numbers. *World Journal of Engineering and Technology*, 02(03), pp.222-233.

Munson, B.R., Okiishi, T.H., Huebsch, W.W. and Rothmayer, A.P., 2013. *Fundamentals of Fluid Mechanics*. 7th ed. Hoboken, New Jersey: John Wiley & Sons, Inc., pp.101 - 468.

Muzaferija, S. and Peric, M., 2017. Computation of free-surface flows using interface-tracking and interface-capturing methods. *Fluid Dynamics and Ship Theory Section*, pp.1 - 42.

Naithani, A.k., 2012. Underground rock caverns for strategic crude oil storage in India - Nature of studies, design and construction. *National Institute of Rock Mechanics*, 103(5), pp.490 - 496.

Nanda, A., Rath, R. and Usmani, A., 2015. *Underground Storage Technologies*. New Delhi: Engineers India Ltd, pp.1 - 176.

Oetjen, J., Schüttrumpf, H. and Engel, M., 2020. Experimental models of coarse-clast transport by tsunamis. In: M. Engel, S. May, E. Garrett, J. Pilarczyk and D. Brill, ed., *Geological Records of Tsunamis and Other Extreme Waves*. Elsevier, pp.585 - 615.

Park, E. and Chung, S., 2014. Experience and challenge of underground oil/gas storage caverns in Korea. *Geosystem Engineering*, 17(5), pp.294-302.

Rath, R., Nanda, A., Malkani, S. and Grover, R.K., 2008. underground rock caverns for storage of hydrocarbons. *Civil Engineering & Construction Review*, pp.72 - 74.

Salih, A., 2017. *Dimensionless Numbers*. [online] www.iist.ac.in. Available at: <https://www.iist.ac.in/sites/default/files/people/numbers.html> [Accessed 16 November 2021].

Schneider, G. and Donadei, S., 2016. Compressed Air Energy Storage in Underground Formations. In: T.M. Letcher, ed., *Storing Energy*. Durban, South Africa: Elsevier, pp.113 - 133.

Sequeiros, O.E., 2012. Estimating turbidity current conditions from channel morphology: A Froude number approach. *Journal of Geophysical Research: Oceans*, 117(C4), pp.1 - 15.

Serway, R.A., 1996. Physics for Scientists and Engineers – Bernoulli's principles. *Saunders College Publishing*, Vol. 1, pp 422 – 434.

Shaheed, R., Mohammadian, A. and Kheirkhah Gildeh, H., 2018. A comparison of standard k–ε and realizable k–ε turbulence models in curved and confluent channels. *Environmental Fluid Mechanics*, 19(2), pp.543-568.

Shammaa, Y. and Zhu, D., 2010. Experimental Study on Selective Withdrawal in a Two-Layer Reservoir Using a Temperature-Control Curtain. *Journal of Hydraulic Engineering*, 136(4), pp.234-246.

Shi, X., Liu, W., Chen, J., Yang, C., Li, Y., Ma, H., Peng, H., Wang, T. & Ma, X., 2017. Geological Feasibility of Underground Oil Storage in Jintan Salt Mine of China. *Advances in Materials Science and Engineering*, pp.1 – 11.

Shirayama, S. and Kuwahara, K., 1990. Flow Visualization in Computational Fluid dynamics, *International Journal of High Performance Computing Applications*, pp. 1 – 16.

Shivam, 2020. *Pipe Flow Simulation in Solidworks*. [image] Available at: <https://skill-lync.com/projects/pipe-flow-simulation-in-solidworks-7> [Accessed 26 October 2020].

Sigl, O., Mohanty, S.K., Krenn, F., Höfer-Öllinger, C.G., Rao, B.E., Babu, V.S., Kudtarkar, D.M., Nizalapur, M. and Padiyar, P.S., 2014. Underground crude oil Strategic storage projects in India. In: *Tunnels for a better life*. Foz do Iguacu: World Tunnel Congress, pp.1 - 9.

Sophocleous, M., 2010. Understanding and explaining surface tension and capillarity: an introduction to fundamental physics for water professionals. *Hydrogeology Journal*, 18(4), pp.811-821.

Strauch, B., Zimmer, M. and Tjallingii, R., 2019. Lab scale salt caverns – first results on construction and investigation techniques. *Advances in Geosciences*, 49, pp.149-154.

Tang, H. and Wrobel, L.C., 2005. Modelling the interfacial flow of two immiscible liquids in mixing processes. *International Journal of Engineering Science*, 43(15-16), pp.1234-1256.

Tatar, A., Halali, M.A. and Mohammad, A.H., 2016. On the Estimation of the Density of Brine with an Extensive Range of Different Salts Compositions and Concentrations. *Journal of Thermodynamics & Catalysis*, 7(2), pp.1 - 10.

Urone, P., Hinrichs, R., Dirks, K. and Sharma, M., 2012. *College Physics*. Houston, Texas: OpenStax College, pp.399 - 429.

Vanysek, P. & Ramirez, L.B., 2008. Interface Between Two Immiscible Liquid Electrolytes: A Review. *J.Chil.Chem* Sec, 53, No 2, pp. 1455 – 1463.

Versteeg, H.K. & Malalasekera, W., 2007, *An Introduction to Computational Fluid Dynamics: THE FINITE VOLUME METHOD*, Second edition, Pearson Education Limited, England.

Wah-Yen, T., Asako, Y., Sidik, N.A.C. and Rui-Zher, G., 2017. Governing Equations in Computational Fluid Dynamics: Derivations and A Recent Review. *Progress in Energy and Environment*, 1, pp.1 - 19.

Wami, E.N., Onunwor, W.M., Chisa, O.S. and Etim, J.D., 2017. Design of a Floating Roof Crude Oil Storage Tank of 100,000 BPD Capacity and Prototype Fabrication. *Journal of Scientific and Engineering Research*, 4(8), pp.318 - 329.

Wang, P. and Anderko, A., 2013. Modeling Interfacial Tension in Liquid–Liquid Systems Containing Electrolytes. *Industrial & Engineering Chemistry Research*, 52(20), pp.6822-6840.

Westerwee, J., 1997. Fundamentals of digital particle image velocimetry. *Measurement Science Technology*, 8, pp. 1379 – 1392.

Yasin, G., Bhanger, M.I., Ansari, T.M., Naqvi, S.M.S.R, Ashraf, M., Ahmad, K. and Talpur, F.N., 2013. Quality and chemistry of crude oils. *Journal of Petroleum Technology and Alternative Fuels*, 4(3), pp.53 - 63.

Zhang, Y., Shi, X., Ma, H., Yang, C., Ye, L., Han, Y. & Zhang, N., 2018. Research on the limit operating pressure of a bedded salt gas storage: A case study. *American Mechanics Association*, pp. 1 – 12.

Zhou, D. & Feng, J., 2010a. Selective withdrawal of polymer solutions: Computations. *Journal of Non-Newtonian Fluid Mechanics*, 165(15-16), pp.839-851.

Zhou, D. & Feng, J., 2010b. Selective withdrawal of polymer solutions: Experiments. *Journal of Non-Newtonian Fluid Mechanics*, 165(15-16), pp.829-838.